A Study of Anode Functional Layer for Protonic Solid Oxide Electrolysis Cells

プロトン固体酸化物電解セルに対するアノード機能層の研究

Chunmei Tang

Graduate School of Chemical Sciences and Engineering

Hokkaido University

September 2022

Table of Contents

Chapter 1 General introduction

1.1 Energy and environmental crisis

Since industrial revolution, the exponential growth in consumption of limited fossil fuels not only leads to a serious energy crisis, but also causes many adverse environmental impacts, i.e., global warming, due to the emission of greenhouse gases, such as carbon dioxide (CO_2), methane (CH_4), nitrogen oxides (NO_x), perfluorocarbons (CF_6, C_2F_6), hydrofluorocarbons (CHF_3, CF_3CH_2F, CH_3CHF_2), and sulfur hexafluoride (SF_6).[1,2] CO_2 is the primary constitution of greenhouse gases, the emission rate accounting 78% and 76% of the entire in 2010 and 2014, respectively, based on the report of Intergovernmental Panel on Climate Change (IPCC).[3] The global CO_2 emission by burning fossil fuels in energy sector is 34.81 billion t in 2020.[4] Paris Agreement (PA) that is legally binding international treaty on climate change was adopted in 2015 by 196 international parties, the goal of which is to limit global warming to well below 2, preferably to 1.5 °C, compared to pre-industrial levels. To achieve this goal, all countries nowadays aim to reach the zero emission of greenhouse gases, that is carbon neutrality by 2050.[5–7]

The development of renewable energy sources, such as wind, solar radiation, biomass and geothermal,[8–10] together with CO_2 recycling techniques,[11,12] is a key issue to achieve both the decrease of CO_2 emissions and the satisfaction of future energy demands. Some of these natural energies are not suitable for the power supply core in large electricity grid because of the intermittent nature and site dependency. Hence, to utilize widely the natural energy sources involves the great demand on the grid-scale electricity storage.[13] Secondary ion batteries are well established technology and must be suited for the hourly or daily energy storage. However, they cannot store the electricity in longer periods than a few days because of the natural discharge, which leads to a demand for the monthly or seasonally storage technology. The conversion of renewable energy to hydrogen fuels offers a promising long-term storage way because hydrogen is easily converted to liquid compounds by physical and chemical sorption

process and thus, easily stored in existing stock infrastructure for long periods without environmental impact.[14] Moreover, hydrogen fuels are regarded as the alternative to fossil fuels because the gravimetric energy density (143 kJ kg^{-1}) is much higher than other chemical-based fuels and energy carriers,[15,16] and exhausts only H_2O through combustion. Hence hydrogen has a potential to realize complete energy cycles based on natural energy without carbon emission, as illustrated in Figure 1-1.

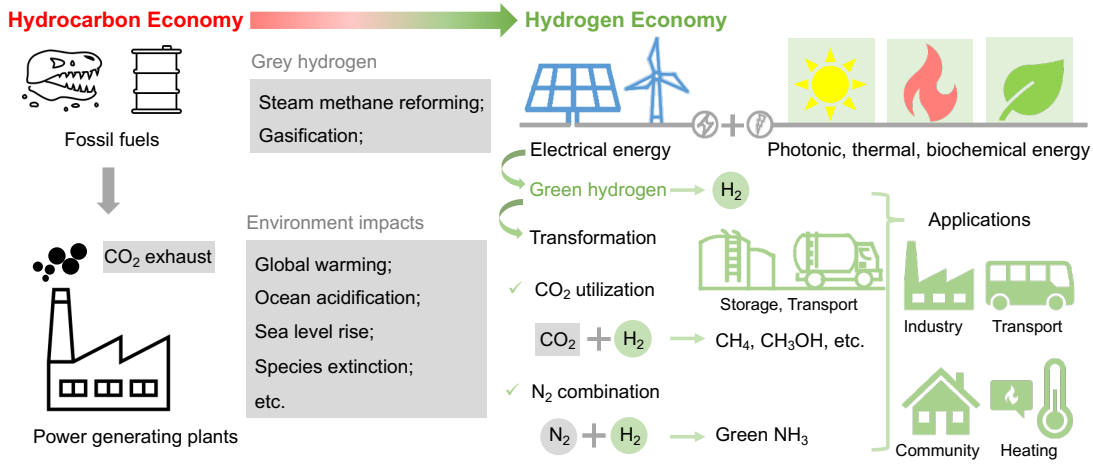

Figure 1-1 Illustration of hydrocarbon economy and green hydrogen economy in synthesis, transformation, and application.

Recently, many governments have announced a series of science and technology strategies to aim the energy-efficient hydrogen production, storage, and utilization technologies.[17–20] The major challenges in the utilization of hydrogen gas as a fuel are to develop cost-effective and energetically rational method to produce the hydrogen gas because it is rare in nature. Therefore, development races towards efficient hydrogen production technologies have been heated up over the world.[21–24]

1.2 Technologies for hydrogen production

Table 1-1 Summary of methods to obtain hydrogen. (Adapted from Ref. 24,25)

Technology	Feedstock	Efficiency	Maturity
Steam reforming	Hydrocarbons	70-85%	Commercial
Partial oxidation	Hydrocarbons	60-75%	Commercial
Autothermal reforming	Hydrocarbons	60-75%	Near term
Plasma reforming	Hydrocarbons	9-85%	Long term
Aqueous phase reforming	Carbohydrates	35-55%	Mid term
Ammonia reforming	Ammonia	-	Near term
Biomass gasification	Biomass	35-50%	Commercial
Photolysis	Water	0.5%	Long term
Dark fermentation	Biomass	60-80%	Long term
Photo fermentation	Biomass	0.1%	Long term
Microbial electrolysis cell	Biomass	78%	Long term
Alkaline electrolyzer	Water	59-70%	Commercial
Proton exchange membrane electrolyzer	Water	65-82%	Commercial
Solid oxide electrolysis cell	Water	up to 90%	Mid term
Thermochemical water splitting	Water	-	Long term
Photoelectrochemical waster splitting	Water	12.4%	Long term

Hydrogen gas can be produced from different resources by catalytic and electrochemical processes as displayed in Table 1-1. The current industry produces hydrogen by means of steam methane reforming (SMR), in which, the endothermic reaction between methane and steam (Equation 1-1) takes place at high temperature (700–1000 °C) and high pressure (14–20 atm) in the first half reactors, and subsequently water gas shift (WGS) reaction (Equation 1-2) progresses at about 360 °C in the second half reactors.[26] Hydrogen prepared by these processes is called “grey hydrogen” since its production involves huge CO_2 esmisson.

$$CH_4 + H_2O \leftrightarrow CO + 3H_2 \ (\Delta H^{\circ}_{298\,K} = +206\ \text{kJ mol}^{-1}) \quad (1\text{-}1)$$

$$H_2O + CO \leftrightarrow CO_2 + H_2 \ (\Delta H^{\circ}_{298\,K} = -41\ \text{kJ mol}^{-1}) \quad (1\text{-}2)$$

Instead of such “gray” hydrogen process, water electrolysis by using renewable energy can produce hydrogen gas without CO_2 emission and thus is an alternative solution for storing energy and establishing sustainable hydrogen economy. Hydrogen thus

prepared is called “green” hydrogen.

Several types of H_2O electrolysis processes, such as alkaline water electrolysis (AWE), anion exchange membrane water electrolysis (AEMWE), proton exchange membrane water electrolysis (PEMECs), and solid oxide steam electrolysis cells (SOECs) have been developed based on different materials and systems, as summarized in Table 1-2.[27] AWE is operated at 20–80 °C where cathode and anode are put in a liquid alkaline electrolyte solution (20–30% KOH or NaOH) with separated by a diaphragm (usually asbestos) to prevent mixing of O_2 and H_2 gases, as depicted in the schematic image in Table 1-2. Ni based metal electrodes are usually used as electrodes in AWE due to its favorable activity and stability.[28,29] AWE is a mature technology, having advantages: saving amounts of non-noble metal catalysts, long-term stability, and relative low cost. It, however, also involves some drawbacks, such as large electrode overpotential due to the less activity of catalysts at low operation temperature, crossover of gases, limited current density (200–400 mA cm^{-2}), and so on.[22,29]

The alkaline polymer electrolyte membranes, which are formed by the solid polymer backbone with cationic functional groups, are applied in anion exchange membranes water electrolysis (AEMWE).[30,31] The major shortcoming of AEMWE is the relatively low thermal stability structure of cationic functionality of polymer at high pH condition. Moreover, state-of-the-art AEMWE uses amounts of noble metal electrocatalysts (Pt, Ru, Ir etc.) in both cathode and anode, and it is crucial issue to develop alternative catalysts without sacrificing the electrochemical performance. Ni-Mo or Ni-Fe alloys have been identified as potential candidate of transition metal catalysts.[32]

The cation exchange membranes water electrolysis (PEMWE) has established itself in the marketplace at a particular application sector because of the outstanding advantages, including the compact design, fast response, high output pressure and efficiency. PEMWE can be generally operative at a current density of 2 A cm^{-2} at 50–80 °C with a bias approximately 2.1 V.[30] The high performance of PEMWE largely relies on high activity of platinum group metals (PGM) catalysts (like Pt, Ir and Ru) for both oxygen evolution reaction (OER) and hydrogen evolution reaction (HER). Therefore, the resource scarcity of PGM limits the applications of PEMWE.

Solid oxide electrolysis cell (SOECs) and protonic solid oxide electrolysis cells (P-SOECs) are based on oxygen-ion and proton conducting oxide electrolyte, respectively, both of which conduct steam electrolysis at elevated temperatures. Recently, they have drawn considerable attention due to thermodynamical advantages. The reaction of H_2O electrolysis is given by Equation (1-3).

$$H_2O + \text{electric energy } (\Delta G) + \text{heat } (Q) \longrightarrow H_2 + \frac{1}{2}O_2 \tag{1-3}$$

Figure 1-2 shows the thermodynamics of water and steam electrolysis at atmospheric pressure, in which, the total energy (standard enthalpy, $\Delta H = \Delta G + T\Delta S$) for H_2O splitting requires a fraction of electrical energy (Gibbs free energy, ΔG) and heat energy ($Q = T\Delta S$).[33–35] Standard thermodynamic parameters, ΔH and ΔS are functions of temperature, as given by Equation (1-4) and (1-5).

$$\Delta H = \Delta H^{\circ}_{298.15} + \int_{298.15}^{T} \Delta C_p \, dT \tag{1-4}$$

$$\Delta S = \Delta S^{\circ}_{298.15} + \int_{298.15}^{T} \frac{\Delta C_p}{T} \, dT \tag{1-5}$$

Here, ΔC_p is constant-pressure molar heat capacity. Total energy, i.e., ΔH for steam electrolysis is smaller than that for water electrolysis because of the gain by vaporization heat, as shown by the jump point in Figure 1-2 at approximately 100 °C. This thermodynamic feature assesses the steam electrolysis as energy-rational way to produce the green hydrogen because the steam electrolysis can conduct water-splitting with smaller electrical energy than water electrolysis, as calculated by ΔH, if the exhaust heat is available for water vaporization. The details are described below.

The water or steam electrolysis can be progressive when the applied bias is higher than the reversible voltage (E_{rev}) which is determined by the Nernst equation, as given by Equation (1-6).

$$E_{rev} = \frac{1}{nF}\Delta G + \frac{RT}{nF}\ln\frac{p_{H_2}p_{O_2}^{1/2}}{p_{H_2O}} \tag{1-6}$$

In SOECs and P-SOECs, the pressure is usually fixed at 1 atm, thereby, the E_{rev} is calculated by Equation (1-7), leading to E_{rev} equaling 1.23 V at standard conditions

(25 °C and 1 atm) for H_2O splitting (Figure 1-3). The thermodynamic data used in this thesis, are referred to Ref.36.

$$E_{rev} = \frac{\Delta G}{nF} = \frac{237.16\times1000}{2\times96485} \approx 1.23 \text{ (V)} \quad (1\text{-}7)$$

Here, n is the number of electrons and F is Faradaic constant (= 96485 C mol^{-1}). The total energy needed for H_2O electrolysis is used to determine thermal neutral voltage (also denoted as enthalpy voltage (E_{the})), which is defined as the minimum thermodynamic voltage for steam or water electrolysis and can be calculated by Equation (1-8) at 25 °C.

$$E_{the} = \frac{\Delta H}{nF} = \frac{285.83\times1000}{2\times96485} \approx 1.48 \text{ (V)} \quad (1\text{-}8)$$

Near the operation temperature of SOECs and P-SOECs, for example, at 700 °C, E_{the} is approximately 1.28 V, which is smaller than that of water electrolysis at 25 °C by 0.2 V. Therefore, the performance of SOECs and P-SOECs is usually evaluated with a bias at around 1.30 V near E_{the}.

Unlike water electrolysis, both SOECs and P-SOECs normally keep high electrolysis performance with transition metal oxide base electrodes (Figure 1-3) because the electrode reactions are significantly activated at elevated temperatures.[37] Moreover, both devices can be applied to the CO_2-H_2O co-electrolysis, which is a promising method to direct conversion of CO_2 to CO, CH_4 and other utility chemicals with resources of renewable energy.

Table 1-2 Comparison of the typical characteristic of water-splitting technologies.

Cells	Water electrolysis			Steam electrolysis	
	AWE	AEMWE	PEMWE	P-SOECs	SOECs
Operation principles	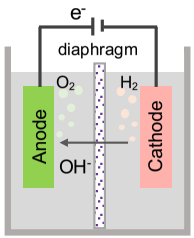	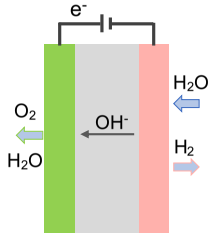	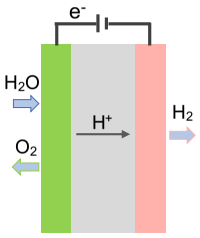	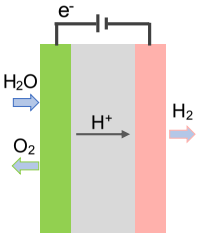	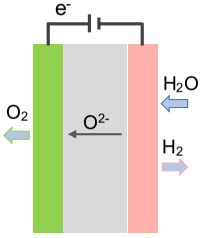
Charge carrier	OH^-		H^+		O^{2-}
Temperature	20-80 °C	20-200 °C		500-700 °C	750-900 °C
Electrolyte	liquid (~20% KOH)	solid (polymeric)	solid (polymeric)	solid (ceramic)	solid (ceramic)
Anode reaction (OER)	$2OH^- \rightarrow H_2O+\frac{1}{2}O_2+2e^-$		$H_2O \rightarrow 2H^+ + \frac{1}{2}O_2+2e^-$		$O^{2-} \rightarrow \frac{1}{2}O_2+2e^-$
Anodes	Ni, Co, Fe(oxides) perovskites	Ni-based	IrO_2, RuO_2; TiO_2, ITO, TiC	$Ba(Zr,Ce,M)O_{3-\delta}$ (M = Y, Yb, etc.)	YSZ, GDC, SDC
Cathode reaction (HER)	$2H_2O+2e^- \rightarrow 2OH^- + H_2$		$2H^+ + 2e^- \rightarrow H_2$		$H_2O+2e^- \rightarrow H_2+O^{2-}$
Cathodes	Ni alloys	Ni, Ni-Fe, $NiFe_2O_4$	Pt/C, MoS_2	Ni-cermet	Ni-YSZ
Efficiency	59-70%		65-82%	up to 100%	
Applicability	commercial	laboratory scale	near-term commercialization	laboratory scale	demonstration
Advantages	low capital cost; relatively stable; mature technology	combination of alkaline and H^+-PEM electrolysis	compact design; fast response/start-up; high-purity H_2	enhanced kinetics; thermodynamics; high efficiency	
Drawbacks	limited current density; corrosive electrolyte; low dynamics	low OH^- conductivity in polymeric membranes	high cost of polymeric membranes, noble metals	unstable electrodes (cracking)	
Challenge	improve durability/reliability; oxygen evolution	improve electrolyte	reduce noble-metal utilization	microstructure changes in electrodes: delamination, blocking of TPB*, passivation	

* gas-anode-electrolyte triple phase boundary

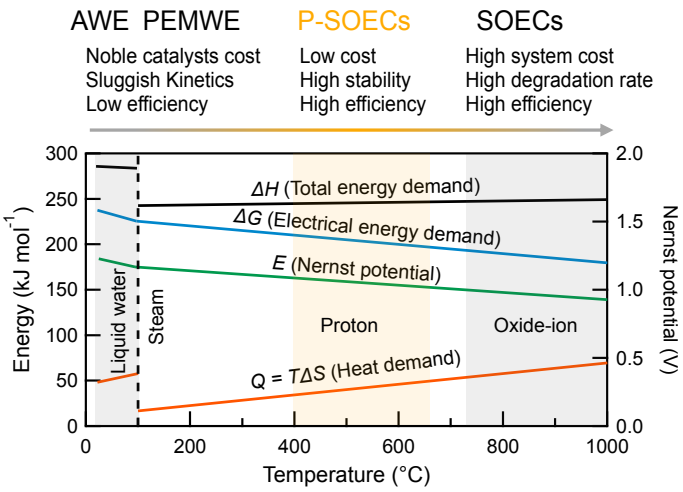

Figure 1-2 Energy demand of total (ΔH), thermal (Q) and electrical (ΔG) for ideal water or steam electrolysis process as a function of temperature.

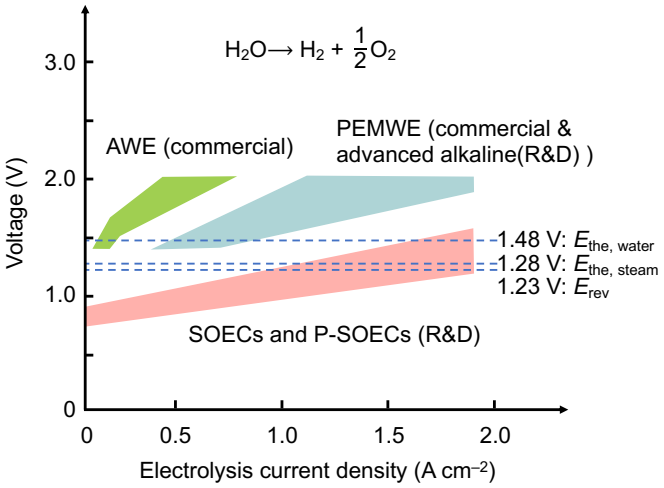

Figure 1-3 Typical performance ranges for competing electrolysis technologies for H_2O splitting (R&D: research and development).[37]

1.3 Solid oxide electrolysis cells

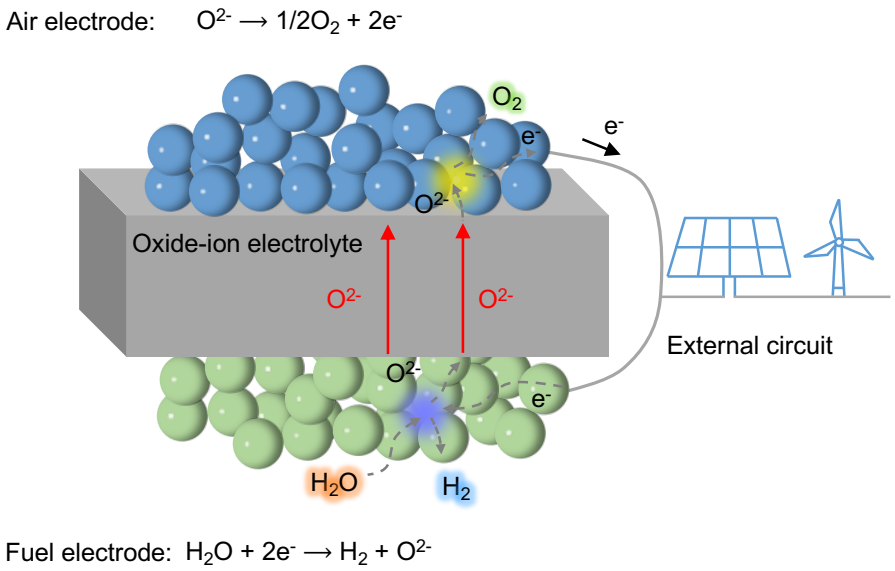

Figure 1-4 Schematic illustration of the operation mechanism in SOECs.

SOECs depicted in Figure 1-4 are electrochemical devices consisting of three main components: two porous electrodes and a dense ceramic electrolyte film with oxide-ion conductivity. The typical electrolytes are yttrium-doped ZrO_2 (YSZ) and samarium-doped ceria (SDC). Because of the large activation energy associated with oxide-ion conduction of SOECs, high operating temperatures (700–1000 °C) are required to reach sufficient ionic conductivity. Here, some of the electrolysis performance in SOECs is summarized in Table 1-3, which shows the outstanding current density is ~2 A cm^{-2} at 750 °C. The high operating temperature is an important feature of SOECs but causes serious problems regarding to material degradation and limited long-term stability; for example, delamination of anode caused by coarsening of porous Ni-YSZ cermet, intermixing of cathode and electrolyte materials due to the high oxygen chemical potential gradient, and so on.[38–40] Therefore, it is strongly motivated to decrease operating temperature of SOECs below 600 °C. In addition, steam gases including impurities such as CO_2, O_2 etc are fed to the fuel electrode side in SOECs, as shown in Figure 1-4, and thus, purification process is needed to obtain pure and dry hydrogen after electrolysis.

Table 1-3 Current density of SOECs at 1.3 V.

Configuration of SOECs: Air electrode/electrolyte/fuel electrode	Measurement condition		Current density ($A\ cm^{-2}$)	Ref.
	Temperature (°C)	Humidity (%)		
SSC-SDC/GDC (barrier layer)/YSZ/Ni-YSZ	750	50	3.13	41
SSC-SDC/GDC (barrier layer)/YSZ/Ni-YSZ	800	50	4.08	41
LSM/YSZ/Ni-YSZ	800	50	~0.80	42
LSCF-GDC/YSZ/Ni-YSZ	850	50	~0.74	43
LSCF-GDC/GDC (barrier layer)/YSZ/Ni-YSZ	800	50	0.85	44
LSCF-GDC/GDC (barrier layer)/YSZ/Ni-YSZ	750	50	0.90	45
LSCF-GDC-SSC/GDC (barrier layer)/YSZ/Ni-YSZ	750	50	1.80	45
YSZ-SSC/YSZ/Ni-YSZ	750	50	0.71	46
BSCF-SDC/YSZ/ Ni-YSZ	850	80	~0.40	47
NN/YSZ/Ni-GDC	750	47	0.40	48
LSCN/10Sc1CeSZ/Ni-YSZ	850	31	0.87	49
LSCF-GDC/GDC (barrier layer)/YSZ/Ni-YSZ	750	75	0.58	50
LSM-YSZ/YSZ/Ni-YSZ	895	70	0.68	51
LSCF/YSZ/Ni-YSZ	750	50	1.72	52
LSCF/LSGM/Ni-LSGM	650	50	~2.00	53
LSCF2882/GDC (barrier layer)/YSZ/Ni-YSZ	700	50	0.82	54
STFC/YSZ/Ni-YSZ	700	50	1.48	55
PrO_x-GDC/GDC/YSZ/Ni-YSZ	700	50	2.9	56

Abbreviations: $Sm_{0.5}Sr_{0.5}CoO_{3-\delta}$ (SSC); $Ce_{0.8}Sm_{0.2}O_{2-\delta}$ (SDC); (La, Sr)$MnO_{3-\delta}$ (LSM); $La_{0.6}Sr_{0.4}Co_{0.2}Fe_{0.8}O_{3-\delta}$ (LSCF); $Ce_{0.9}Gd_{0.1}O_{2-\delta}$ (GDC); $Ba_{0.5}Sr_{0.5}Co_{0.8}Fe_{0.2}O_{3-\delta}$ (BSCF); $Nd_2NiO_{4+\delta}$ (NN); $La_{1.7}Sr_{0.3}Co_{0.5}Ni_{0.5}O_{4+\delta}$ (LSCN); 10% Sc_2O_3 and 1%CeO_2 doped ZrO_2 (10Sc1CeSZ); $(La_{0.9}Sr_{0.1})_{0.98}Ga_{0.8}Mg_{0.2}O_{3-\delta}$ (LSGM); $La_{0.2}Sr_{0.8}Co_{0.8}Fe_{0.2}O_{3-\delta}$ (LSCF2882); $SrTi_{0.3}Fe_{0.63}Co_{0.07}O_{3-\delta}$ (STFC);

1.4 Protonic solid oxide electrolysis cells

Protonic solid oxide electrolysis cells (P-SOECs) based on proton-conducting electrolytes are promising alternative to the conventional oxide-ion conducting SOECs. Proton-conducting oxides, typically, $Ba(Zr,Ce)O_{3-\delta}$, has a lower mobility activation energy (0.4–0.6 eV) compared to oxide-ion conducting electrolyte (YSZ, ~0.8 eV),[57] thereby resulting in higher conductivity (> 10^{-3} S cm $^{-1}$) at 500 °C.[58,59] Therefore, P-SOECs can be operative at lower temperatures than SOECs. In addition, the steam is fed in air electrode (anode) of P-SOECs as shown in Figure 1-6, thus, P-SOECs enable the production of pure and dry hydrogen at fuel electrode (cathode). Moreover, the P-SOECs avoid the issue of Ni oxidation/coarsening in SOECs. Therefore, P-SOECs are potential devices for hydrogen production at intermediate temperatures (400–700 °C), which are expected to have high current, efficiency, and long-term durability.

1.4.1 Proton-conducting oxides

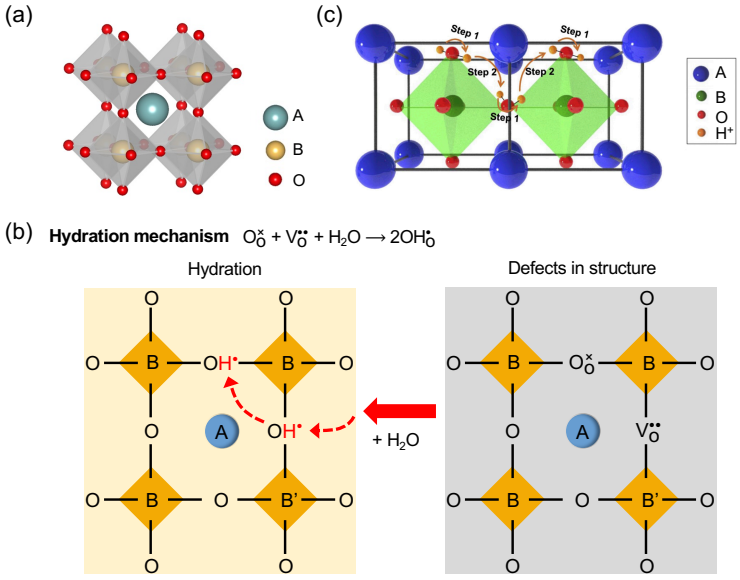

Figure 1-5 (a) Crystal structure of ABO_3 perovskite. (b) Hydration mechanism. (c) Schematic illustration of the proton rotation and hopping for Grotthuss mechanism.

Proton-conducting oxides have been actively investigated for decades, since Forrat et al. first reported the phenomenon of proton conduction in $LaAlO_3$ ceramic.[60] The

studies in the past few decades clarify that the proton-conducting oxides are fundamentally 'hydrated' oxides and can be categorized to three structure types: perovskite (ABO_3), fluorite (AO_2) and pyrochlore ($A_2B_2O_7$). The most ubiquitous and attracted proton-conducting oxides are $BaCeO_3$ and $BaZrO_3$ base perovskites, which exhibit higher hydration capability and proton conductivity than other groups. The ideal ABO_3 perovskite shows a cubic (space group, $Pm\bar{3}m$) structure, in which, the A-site and B-site cations are in twelve-fold coordination and six-fold coordination with oxygen, respectively, as shown in Figure 1-5a. Unfortunately, $BaCeO_3$ and $BaZrO_3$ base oxides can't satisfy all the requirements of P-SOECs. $BaCeO_3$ base electrolytes have high proton conductivity, while are unstable in steam electrolysis conditions since decomposing to $Ba(OH)_2$ and CeO_2 in relatively high water pressure at temperatures below 800 °C.[61] $BaZrO_3$-based electrolytes show excellent thermodynamic stability under high humidity but exhibit larger grain boundary resistances because the ceramics have coarse granular morphology due to poor sinterability.[62] By combining the advantages of both oxides, the electrolyte materials fall into the solid solution $Ba(Zr,Ce,M)O_{3-\delta}$ (M = Y, Yb, etc.). M is the trivalent rare earth ions as the B-site acceptor dopant. Yttrium (Y) was found to fit seamlessly into the host lattice without large crystal distortion.[63–65] Ytterbium (Yb) was identified to further improve the chemical stability of $Ba(Zr,Ce,M)O_{3-\delta}$ and to be beneficial for the migration of oxygen vacancies.[65,66]

In perovskites, mobile proton defects ($OH_O^{\bullet}$) are incorporated by thermodynamic hydration via the association of oxygen vacancies ($V_O^{\bullet\bullet}$) and water vapor, and thus the oxygen vacancies are occupied by hydroxide ions, as shown in Figure 1-5b. This process is called hydration reaction expressed as Equation (1-9).

$$O_O^{\times} + V_O^{\bullet\bullet} + H_2O \longrightarrow 2OH_O^{\bullet} \qquad (1\text{-}9)$$

Hereafter, the defect thermodynamic reactions are represented by Kröger–Vink notation. In Equation (1-9), $O_O^{\times}$ is the lattice oxygen. Grotthuss-type mechanism is most widely accepted for the proton transfer process in oxide crystals, as shown in Figure 1-5c.[67,68] H_2O is chemisorbed on the oxygen vacancy on the ceramic surfaces and one proton coordinates to the neighbor lattice oxygen atom with forming a weak

O-H bond. Then, the proton rotates and hops from one oxide ion to the nearest neighbor ones, in which one O-H bond is broken while simultaneously another O-H bond is formed with the neighboring oxide ion.[69]

1.4.2 Cell structure and operation mechanism

P-SOECs were first reported by Iwahara et al. in 1981, in which the electrolysis of steam was performed using $SrCe_{1-x}Sc_xO_{3-\delta}$ (x = 0.05 and 0.1) bulk electrolyte with a thickness of about 0.5 mm and Pt electrodes. They demonstrated the current efficiencies for hydrogen evolution were in the range of 50–95% and the reasons for current loss may be ascribed to the conduction due to electron holes in electrolytes.[70] After the numerical studies for fabrication of protonic ceramics,[71–74] He et al. had successfully fabricated the lab-scale electrolysis cells with electrolyte thin film of about 20 μm thickness by a dry-pressing method.[75] The current thin film P-SOECs typically comprise of the porous cermet cathode support, dense and thin electrolyte film (10–30 μm) and porous nanoparticles layer of anode, as shown in Figure 1-6.

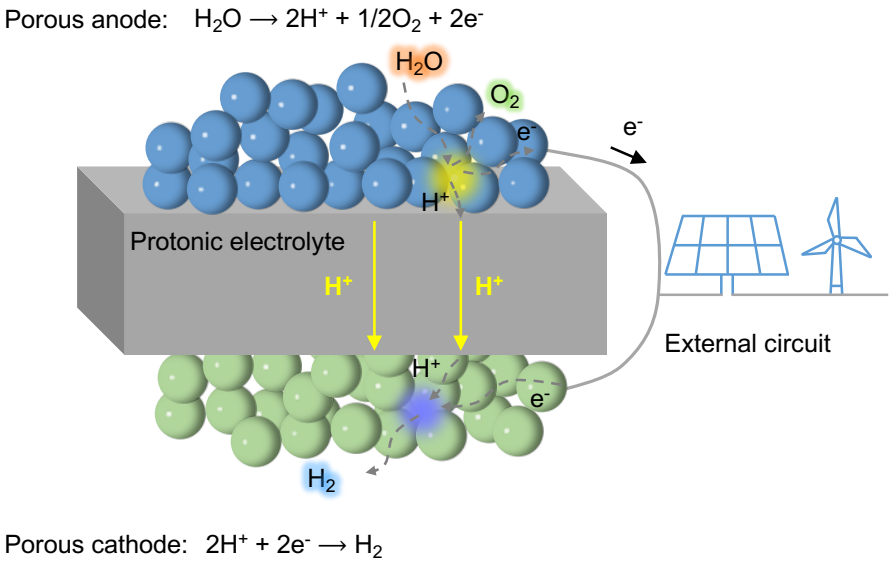

Figure 1-6 Schematic illustration of the operation mechanism in P-SOECs.

The anode reactions including the oxygen evolution reaction (OER) of P-SOECs are mainly progressive at the sites near the gas-anode-electrolyte triple-phase boundary

(TPB), in which the OER is caused by coupled with interfacial diffusion of protons and oxygen species. At the cathode side, hydrogen evolution reaction (HER) takes place via coupling of protons and electrons at metal-electrolyte-gas TPB. These electrochemical reactions are promoted by applying a bias between two electrodes, as depicted in Figure 1-6.

1.4.3 Performance of current proton solid oxide electrolysis cells

As mentioned before, the first report from Iwahara et al.[70] demonstrated steam electrolysis was conducted with a Faradaic efficiency of 50–90% in the current range of 0.1–0.8 A cm^{-2} at 900 °C by using the cells of $SrCe_{1-x}Sc_xO_{3-\delta}$ bulk electrolyte. Nevertheless, P-SOECs received relatively little attention owing to the poor sinterability and complexity in stoichiometry of proton conducting ceramics until 2000's. In 2007–2009, Babilo et al. and Yamazaki et al. pioneered the ZnO sintering aid that can dramatically lower the sintering temperatures,[76,77] which stimulates numerous researches of P-SOECs. In 2010, P-SOECs based on $Sm_{0.5}Sr_{0.5}CoO_{3-\delta}$–$BaZr_{0.3}Ce_{0.5}Y_{0.2}O_{3-\delta}$ (SSC-BZCY352) composite anode and BZCY352 thin electrolyte achieved electrolysis current of 0.19 A cm^{-2} at 1.3 V and 600 °C with 50%H_2O-Air and pure H_2 as reacting gases.[75] In more recent year (2019), Duan et al. reported a champion data of P-SOECs based on with $BaZr_{0.1}Ce_{0.7}Y_{0.1}Yb_{0.1}O_{3-\delta}$ (BZCYYb1711) thin film electrolyte and $BaCo_{0.4}Fe_{0.4}Zr_{0.1}Y_{0.1}O_{3-\delta}$ (BCFZY) anode, which demonstrated electrolysis at thermal neutral voltage (1.3 V) with remarkably high Faradaic efficiency of 90–98% and electrochemical current (1.00 A cm^{-2}) at 600 °C.[78] In the same year, Choi and co-workers reported excellent performance of the cells applied by proton-conducting $PrBa_{0.5}Sr_{0.5}Co_{2-x}Fe_xO_{5+\delta}$ (PBSCF) anode on thermodynamically stable $BaZr_{0.4}Ce_{0.4}Y_{0.1}Yb_{0.1}O_{3-\delta}$ (BZCYYb4411) electrolyte. Finally, P-SOECs yielded a current of 1.42 A cm^{-2} but a relatively low Faradaic efficiency near 46% at 1.3 V and 600 °C.[79] In 2022, Bian et al. founded that a simple acid treatment can effectively rejuvenate the high-temperature annealed electrolyte surface, resulting in reactive bonding between anode and electrolyte and achieving a current approximately 1.86 A cm^{-2} at 1.3 V and 600 °C.[80] All mentioned performance

here is summarized in Table 1-4. In conclusion, those excellent performance indicates that P-SOECs are promising technology for hydrogen production at intermediate temperatures.

Table 1-4 Current density of P-SOECs at 1.3V and 600 °C.

Configuration of electrolysis cell: Anode/electrolyte (thickness)/cathode	Inlet gas composition		*I* ($A\ cm^{-2}$)	Ref.
	Anode	Cathode		
SSC-BZCY352/BZCY352 (20 μm)/Ni-BZCY352	Air (50% H_2O)	100% H_2	~0.19	75
LSC-BZCYbCo/BZCYbCo (45 μm)/Ni-BZCYbCo	Air (30% H_2O)	10% H_2/He	0.03	81
LSCF-BZY82/BZY91 (15 μm)/Ni-BZY82	Air (3% H_2O)	4% H_2/Ar	0.05	82
LSCF/BZCYYb4411 (15 μm)/Ni-BZCYYb4411	Air (3% H_2O)	97% H_2 (3% H_2O)	0.70	79
LSM/BZCYYb4411 (15 μm)/Ni-BZCYYb4411	Air (3% H_2O)	97% H_2 (3% H_2O)	0.65	79
LSCF/BZCY442 (24 μm)/Ni-BZCY442	Air (3% H_2O)	97% H_2 (3% H_2O)	0.50	83
LNO-BZCDy/ BZCDy (30 μm)/Ni-BZCDy	Air (90% H_2O)	97% H_2 (3% H_2O)	0.16	84
BSCF-BZCY262/BZCY262 (10-15μm)/Ni-BZCY262	Air (2.76% H_2O)	50% H_2 (2.76% H_2O)	1.05	85
PNO/LCO|BZCYYb1711 (bilayer 20 μm)/Ni-BZCYYb1711	Air (60% H_2O)	100% H_2	0.33	86
SFM-BZY82/BZY82 (16 μm)/Ni-BZY82	Air (3% H_2O)	10% H_2/N_2	0.21	87
SFM-BZY82/BZY82 (18 μm)/Ni-BZCY172	Air (3% H_2O)	20% H_2/N_2	0.38	88
SEFC-BZCY532/BZCY532 (15 μm)/Ni-BZCY532	Air (10% H_2O)	97% H_2 (3% H_2O)	0.42	89
SLF/BZCY352 (20 μm)/Ni-BZCY352	Air (20% H_2O)	97% H_2 (3% H_2O)	0.46	90
LSN/BZCY172 (15 μm)/Ni-BZCY172	Air (20% H_2O)	97% H_2 (3% H_2O)	0.42	91
LSN/BZCYYbCu (13 μm)/Ni-BZCYYbCu	Air (20% H_2O)	97% H_2 (3% H_2O)	0.59	92
LSN-BZCYYbCu/BZCYYbCu (13 μm)/Ni-BZCYYbCu	Air (20% H_2O)	97% H_2 (3% H_2O)	1.03	93
PNO-BZCY262/ BZCY262 (20 μm)/ Ni-BZCY262	Air (40% H_2O)	100% H_2	0.60	94
BGLC-BZCY721/BZCY721 (~20 μm)/Ni-BZCY721	5%O_2/Ar (50% H_2O)	10% H_2/Ar	0.11	95
NBSCF-BZCYYb1711/BZCYYb1711 (20 μm)/Ni-BZCYYb1711	Air (10% H_2O)	97% H_2 (3% H_2O)	0.75	96
PBSCF/BZCYYb (20 μm)/Ni-BZCYYb	O_2 (3% H_2O)	100% H_2	0.55	97
PBSCF/BZCYYb4411 (15 μm)/Ni-BZCYYb4411	Air (3% H_2O)	97% H_2 (3% H_2O)	1.42	79
PBSCF/BZCYYb4411 (15 μm)/Ni-BZCYYb4411	Air (3% H_2O)	5% H_2/Ar	1.31	79
PBSCF(3D)/BZCYYb (20 μm)/Ni-BZCYYb	O_2 (12% H_2O)	5% H_2/Ar	0.85	98

PBSCF/BHCYYb3511 (10 μm)/Ni-BHCYYb3511	Air (3% H_2O)	97% H_2 (3% H_2O)	1.45	99
BCFZY/BZCYYb1711 (12 μm)/Ni-BZCYYb1711	Air (10% H_2O)	100%Ar	1.00	78
BCFZY-BZCY361/BZCYSm (25 μm)/Ni-BZCYSm	Air (12% H_2O)	97% H_2 (3% H_2O)	0.37	100
PBCC95/BZCYYb4411 (20 μm)/Ni-BZCYYb4411	O_2 (20% H_2O)	97% H_2 (3% H_2O)	0.72	101
LSCN8210/BZCY442 (24 μm)/Ni-BZCY442	Air (3% H_2O)	97% H_2 (3% H_2O)	0.87	83
LSCN8273/BZCY442 (24 μm)/Ni-BZCY442	Air (3% H_2O)	97% H_2 (3% H_2O)	1.09	83
PNC/BZCYYb4411 (15 μm)/Ni-BZCYYb4411	Air (10% H_2O)	10% H_2/Ar	0.85	102
PNC(3D)/BZCYYb4411 (15 μm)/Ni-BZCYYb4411	Air (10% H_2O)	10% H_2/Ar	1.18	102
PBCC-BCO/BZCYYb1711 (10 μm)/Ni-BZCYYb1711	Air (3% H_2O)	97% H_2 (3% H_2O)	1.51	103
YEBCG/BZCYYb1711 (13.6 μm)/Ni-BZCYYb1711	Air (20% H_2O)	10% H_2/N_2	~1.18	104
SCFN/BZCYYb1711 (26 μm)/Ni-BZCYYb1711	Air (3% H_2O)	100% H_2	0.36	105
PLNCu-BZCY172/BZCY172 (15μm)/ Ni-BZCY	Air (3% H_2O)	97% H_2 (3% H_2O)	0.76	106
PNC/(acid treated)BZCYYb1711 (22 μm)/Ni-BZCYYb1711	O_2 (30% H_2O)	100% H_2	~1.86	80

Abbreviations of anode: $Sm_{0.5}Sr_{0.5}CoO_{3-\delta}$ (SSC); $(LaSr)CoO_{3-\delta}$ (LSC); $La_{0.6}Sr_{0.4}Co_{0.2}Fe_{0.8}O_{3-\delta}$ (LSCF); $La_{0.8}Sr_{0.2}MnO_{3-\delta}$ (LSM); $La_2NiO_{4+\delta}$ (LNO); $Ba_{0.5}Sr_{0.5}Co_{0.8}Fe_{0.2}O_{3-\delta}$ (BSCF); $Pr_2NiO_{4+\delta}$ (PNO); $La_2NiO_{4+\delta}$ (LNO); $Sr_2Fe_{1.5}Mo_{0.5}O_{6-\delta}$ (SFM); $SrEu_2Fe_{1.8}Co_{0.2}O_{7-\delta}$ (SEFC); $Sr_{2.8}La_{0.2}Fe_2O_{7-\delta}$ (SLF); $La_{1.2}Sr_{0.8}NiO_4$ (LSN); $Ba_{1-x}Gd_{0.8}La_{0.2+x}Co_2O_{6-\delta}$ (BGLC); $NdBa_{0.5}Sr_{0.5}Co_{1.5}Fe_{0.5}O_{5+\delta}$ (NBSCF); $PrBa_{0.5}Sr_{0.5}Co_{2-x}Fe_xO_{5+\delta}$ (PBSCF); $BaCo_{0.4}Fe_{0.4}Zr_{0.1}Y_{0.1}O_{3-\delta}$ (BCFZY); $(PrBa_{0.8}Ca_{0.2})_{0.95}Co_2O_{6-\delta}$ (PBCC95); $La_{0.8}Sr_{0.2}CoO_{3-\delta}$ (LSCN8210); $La_{0.8}Sr_{0.2}Co_{0.7}Ni_{0.3}O_{3-\delta}$ (LSCN8273); $La_{0.5}Sr_{0.5}CoO_{3-\delta}$ (LSC55); $PrNi_{0.5}Co_{0.5}O_{3-\delta}$ (PNC); $PrBa_{0.8}Ca_{0.2}Co_2O_{5+\delta}$-$BaCoO_{3-\delta}$ (PBCC-BCO); $Y_{0.8}Er_{0.2}BaCo_{3.2}Ga_{0.8}O_{7+\delta}$ (YEBCG); $Sr_{0.9}Ce_{0.1}Fe_{0.8}Ni_{0.2}O_{3-\delta}$(SCFN); $(Pr_{0.9}La_{0.1})_2(Ni_{0.8}Cu_{0.2})O_{4+\delta}$ (PLNCu);

Abbreviations of electrolyte and cathode: $BaZr_{0.3}Ce_{0.5}Y_{0.2}O_{3-\delta}$ (BZCY352); $BaZr_{0.40}Ce_{0.48}Yb_{0.1}Co_{0.02}O_{3-\delta}$ (BZCYbCo); $BaZr_{0.8}Y_{0.2}O_{3-\delta}$ (BZY82); $BaZr_{0.9}Y_{0.1}O_{3-\delta}$ (BZY91); $BaZr_{0.4}Ce_{0.4}Y_{0.1}Yb_{0.1}O_{3-\delta}$ (BZCYYb4411); $BaZr_{0.4}Ce_{0.4}Y_{0.2}O_{3-\delta}$ (BZCY442); $BaZr_{0.3}Ce_{0.5}Dy_{0.2}O_{3-\delta}$ (BZCDy); $BaZr_{0.2}Ce_{0.6}Y_{0.2}O_{3-\delta}$ (BZCY262); $BaZr_{0.1}Ce_{0.7}Y_{0.1}Yb_{0.1}O_{3-\delta}$ (BZCYYb1711); $BaZr_{0.1}Ce_{0.7}Y_{0.2}O_{3-\delta}$ (BZCY172); $BaZr_{0.5}Ce_{0.3}Y_{0.2}O_{3-\delta}$ (BZCY532); $BaZr_{0.3}Ce_{0.5}Y_{0.2}O_{3-\delta}$ (BZCY352); $BaZr_{0.1}Ce_{0.68}Y_{0.1}Yb_{0.1}Cu_{0.02}O_{3-\delta}$ (BZCYYbCu); $BaZr_{0.7}Ce_{0.2}Y_{0.1}O_{3-\delta}$ (BZCY721); $BaZr_{0.1}Ce_{0.7}Y_{0.2-x}Yb_xO_{3-\delta}$ (BZCYYb); $BaHf_{0.3}Ce_{0.5}Y_{0.1}Yb_{0.1}O_{3-\delta}$ (BHCYYb3511); $BaZr_{0.3}Ce_{0.6}Y_{0.1}O_{3-\delta}$ (BZCY361); $BaZr_{0.1}Ce_{0.7}Y_{0.1}Sm_{0.1}O_{3-\delta}$ (BZCYSm); $BaZr_{0.4}Ce_{0.4}Y_{0.2}O_{3-\delta}$ (BZCY442); $BaZr_{0.6}Ce_{0.2}Y_{0.1}Yb_{0.1}O_{3-\delta}$ (BZCYYb6211); $BaZr_{0.2}Ce_{0.5}Y_{0.1}Yb_{0.1}Gd_{0.1}O_{3-\delta}$ (BZCYYbGd).

1.5 Issues of protonic solid oxide electrolysis cells

1.5.1 Resistance of anode reaction

Most of current densities in P-SOEC are below 1.00 A cm^{-2} at 600 °C under 1.3 V as listed in Table 1-4, although several groups have developed P-SOECs with very high electrolysis current. One of the reasons for inferior performance is the large anode reaction resistance. The anode reaction resistance regarding to OER is sluggish and thus involves relatively large overpotential in comparison to the cathode ones regarding to HER, which prompts the development of highly active and highly water-tolerant anode materials for P-SOECs. In the early stage, P-SOECs are employed with the O^{2-}/e^{-} double conductors for the anode, which are widely used in the cathode of solid oxide fuel cells (SOFCs). For instance, $Sm_{0.5}Sr_{0.5}CoO_{3-\delta}$ (SSC) was applied on $BaZr_{0.4}Ce_{0.4}Y_{0.2}O_{3-\delta}$ (BZCY442) dense electrolyte. The cell yielded a current of 0.02 A cm^{-2} at 600 °C under 1.5 V, with a larger polarization resistance of 17.90 Ω cm^2 at 600 °C under open circuit voltage (OCV) as summarized in Table 1-5. Finally, the cell achieved Faradaic efficiency approximately 75% at 600 °C.[107]

The conventional O^{2-}/e^{-} conductors as mentioned above adopt to ABO_3 type perovskite phase. Recently, many other types of oxides were also investigated as anode in P-SOECs. The redox stable perovskite $Sr_2Fe_{1.5}Mo_{0.5}O_{6-\delta}$ (SFM) was demonstrated and the corresponding P-SOECs with BZY82 electrolyte showed promising cell performance, 0.21 A cm^{-2} at 600 °C under 1.30 V with anode resistance of 0.65 Ω cm^2. The cell also achieved a Faradaic efficiency of 63.6%.[87] Their current density increases to 0.38 A cm^{-2} by mixing SFM with $BaZr_{0.8}Y_{0.2}O_{3-\delta}$ (BZCY82).[88] After this, the Ruddlesden-Popper type $SrEu_2Fe_{1.8}Co_{0.2}O_{7-\delta}$ (SEFC) and $Sr_{2.8}La_{0.2}Fe_2O_{7-\delta}$ (SLF) were also proposed as novel anode to optimize the catalytic ability for steam electrolysis.[89,90] Yang et al. reported Cobalt-free Ruddlesden-Popper type $La_{1.2}Sr_{0.8}NiO_4$ can remain stable structure over 100 h in humidified air (20 vol% H_2O) at 800 °C, in which the current density reached to 0.42 A cm^{-2} at 1.30 V and polarization resistance equaled 1.47 Ω cm^2 under OCV condition.[91] Those efforts boosted up the electrochemical

performance of P-SOEC to achieve 0.50 A cm^{-2} near 1.3 V bias at 600 °C.

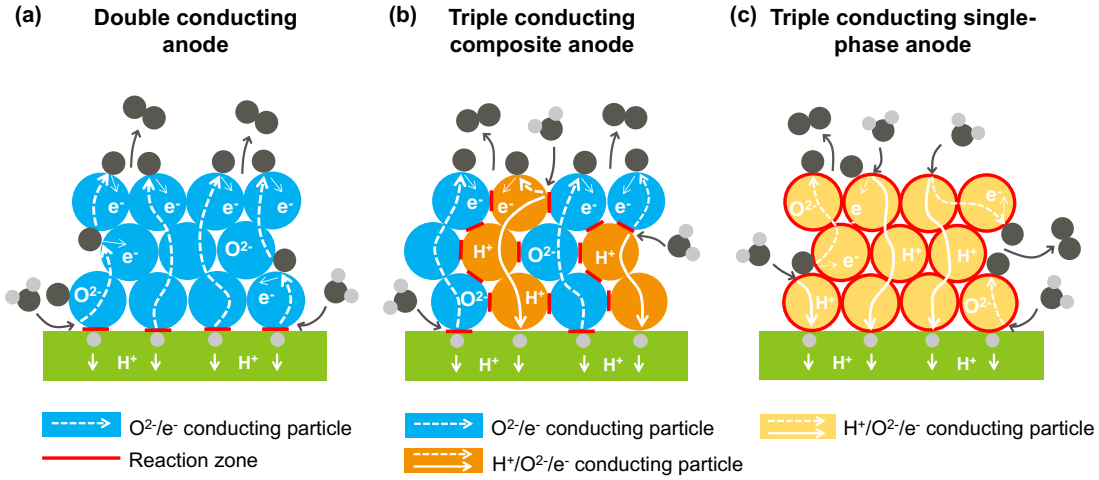

Figure 1-7 The scheme of effective reaction areas for P-SOECs with (a) mixed O^{2-}/e^- double conducting anode, (b) triple conducting composite anode, and (c) triple conducting single-phase anode.

The pure O^{2-}/e^- double conducting anode limits the effective reaction areas into the gas-electrode-electrolyte triple phase boundary (TPB) as shown in Figure 1-7a. Therefore, the anode materials of P-SOECs are favored to possess proton conductivity, together with good catalytic activity and desirable electrical conductivity, to extend the reaction zones into the anode surfaces. For this, to design the composite of double O^{2-}/e^- conductors with proton conducting electrolyte is a simple way to extend the effective reaction area, as shown in Figure 1-7b. He et al. employed SSC-$BaZr_{0.3}Ce_{0.5}Y_{0.2}O_{3-\delta}$ (BZCY352) composite to the air electrode and achieved a current 0.19 A cm^{-2} at 1.32 V with a polarization resistance of 2.41 Ω cm^2 at 600 °C.[75] And the electrochemical performance was characterized with various reacting atmospheres, which shows an increased tendency with the enhancement of steam partial pressure. Bi et al. fabricated the cells with a porous $La_{0.6}Sr_{0.4}Co_{0.2}Fe_{0.8}O_{3-\delta}$ (LSCF6428)-$BaZr_{0.8}Y_{0.2}O_{3-\delta}$ (BZY82) composite air electrode on the $BaZr_{0.9}Y_{0.1}O_{3-\delta}$ (BZY91) electrolyte, which exhibited a current of 0.05 A cm^{-2} at 600 °C under 1.32 V.[82] The performance of P-SOECs is rather low, implying that the composite air electrode would not increase sufficiently the reaction areas.

In more recent year, $H^+/O^{2-}/e^-$ triple conductors have been extensively examined for the anode in P-SOECs, as inspired by the results that triple conductors could spatially expand reaction zone of the cathode on protonic solid oxide fuel cells (P-SOFCs) from TPB to the whole cathode particles, as shown in Figure 1-7c. The application of triple conducting anode in P-SOECs significantly increased the electrolysis currents, which is close to 1 A cm^{-2} at 600 °C near 1.3 V bias and decreases the polarization resistance. In 2018, Kim et al. employed triple conducting $NdBa_{0.5}Sr_{0.5}Co_{1.5}Fe_{0.5}O_{5+\delta}$ (NBSCF) layered perovskite to the anode of P-SOECs with addition of BZCYYb1711, which yielded high current density of 0.75 A cm^{-2} at 1.3 V and very low polarization resistance of about 0.16 Ω cm^2 under OCV at 600 °C.[96] Choi et al. reported a triple conducting material, $PrBa_{0.5}Sr_{0.5}Co_{2-x}Fe_xO_{5+\delta}$ (PBSCF), which was successfully applied as cathode in P-SOFCs with a peak power density (PPD) near 2.2 W cm^{-2} at 600 °C.[108] Wu et al. examined PBSCF anodes on BZCYYb1711 based P-SOECs and achieved the electrolysis current of 0.55 A cm^{-2} at 1.3 V at 600 °C, with a polarization resistance of 0.30 Ω cm under OCV at 600 °C.[97] In 2019, Choi et al. reported that P-SOECs comprising $BaZr_{0.4}Ce_{0.4}Y_{0.1}Yb_{0.1}O_{3-\delta}$ (BZCYYb4411) electrolyte with high proton conductivity and chemically stability and PBSCF air electrode exhibited current density of 1.42 and 1.31 A cm^{-2} at 1.3 V at 600 °C by supplying the cathode gases of humidified H_2 and 5%-H_2/Ar, respectively. And the corresponding polarization resistance is 0.34 Ω cm^2 in the case of 5%-H_2/Ar at 600 °C under OCV.[79] In 2020, Murphy et al. demonstrated a remarkable current density of 1.45 A cm^{-2} at 1.3 V at 600 °C, by employing PBSCF air electrode to the cells with a new proton conductor of $BaHf_xCe_{0.8-x}Y_{0.1}Yb_{0.1}O_{3-\delta}$ (BHCYYb). The identical cell showed similar performance for CO_2-H_2O co-electrolysis conducting with feed of humidified 16%-CO_2/H_2 on the fuel side and excellent stability throughout a 700-h operation.[99] These works unambiguously validate the usefulness of triple conducting PBSCF for P-SOEC anodes. Meanwhile, the durability of PBSCF under high water partial pressure is still unclear because the steam concentration in the above reports is relatively low, ranging from 3 to 12%. Other triple conductors, such as $BaCo_{0.4}Fe_{0.4}Zr_{0.1}Y_{0.2}O_{3-\delta}$ (BCFZY),[78] $(PrBa_{0.8}Ca_{0.2})_{0.95}Co_2O_{6-\delta}$ (PBCC95),[101] $La_{0.8}Sr_{0.2}Co_{1-x}Ni_xO_{3-\delta}$ (LSCN),[83] and $PrNi_{0.5}Co_{0.5}O_{3-\delta}$ (PNC)[80,102,109]

were also reported to present low polarization resistances and superior electrochemical performance of P-SOECs.

Table 1-5 Polarization resistance of P-SOECs at 600 °C and open circuit voltage (OCV).

Configuration of electrolysis cell: Anode/electrolyte (thickness)/cathode	Polarization resistance (Ω cm^2)	Ref.
SSC/BZCY442 (1.5 mm)/Pt	17.90	107
BMO-ATO/BZCY442 (1.5 mm)/Pt	17.50	110
SSC-BZCY352/BZCY352 (20 μm)/Ni-BZCY352	2.41	75
SFM-BZY82/BZY82 (16 μm)/Ni-BZY82	0.65	87
SFM-BZY82/BZY82 (18 μm)/Ni-BZY82	2.81	88
SFM-BZY82/BZY82 (18 μm)/Ni-BZCY172	2.48	88
SEFC-BZCY532/BZCY532 (15 μm)/Ni-BZCY532	0.89	89
SLF/BZCY352 (20 μm)/Ni-BZCY352	2.22	90
LSN/BZCY172 (15 μm)/Ni-BZCY172	1.47	91
PSN/BZCY172 (15 μm)/Ni-BZCY172	2.17	91
NBSCF-BZCYYb1711/BZCYYb1711 (20 μm)/Ni-BZCYYb1711	0.16	96
PBSCF/BZCYYb4411 (15 μm)/Ni-BZCYYb4411	0.34	79
LSCF-BCO/BZCYYb1711 (10 μm)/Ni-BZCYYb1711	0.13	111
PBSCF/BZCYYb (20 μm)/Ni-BZCYYb	0.30	97
BGLC/BZCY721 (~20 μm)/Ni-BZCY721	4.00	95
BGLC-BZCY721/BZCY721 (~20 μm)/Ni-BZCY721	0.80	95
PBCC-BCO/BZCYYb1711 (10 μm)/Ni-BZCYYb1711	0.16	103
LSN-BZCYYbCu/BZCYYbCu (13 μm)/Ni-BZCYYbCu	0.36	93
PNO/LCO|BZCYYb1711 (bilayer 20 μm)/Ni-BZCYYb1711	1.10	86
PNO-BZCY262/ BZCY262 (20 μm)/ Ni-BZCY262	0.40	94
YEBCG/BZCYYb1711 (13.6 μm)/Ni-BZCYYb1711	0.27	104
PLNCu-BZCY172/BZCY172 (15μm)/ Ni-BZCY172	1.04	106
PNC/(acid treated)BZCYYb1711 (22 μm)/Ni-BZCYYb1711	0.08	80

Abbreviations of anode: $Sm_{0.5}Sr_{0.5}CoO_{3-\delta}$ (SSC); $Ba_3(MnO_4)_2$ (BMO); $Sb_{0.05}Sn_{0.95}O_{2-\delta}$ (ATO); $Sr_2Fe_{1.5}Mo_{0.5}O_{6-\delta}$ (SFM); $SrEu_2Fe_{1.8}Co_{0.2}O_{7-\delta}$ (SEFC); $Sr_{2.8}La_{0.2}Fe_2O_{7-\delta}$ (SLF); $La_{1.2}Sr_{0.8}NiO_4$ (LSN); $Pr_{1.2}Sr_{0.8}NiO_4$ (PSN); $NdBa_{0.5}Sr_{0.5}Co_{1.5}Fe_{0.5}O_{5+\delta}$ (NBSCF); $PrBa_{0.5}Sr_{0.5}Co_{2-x}Fe_xO_{5+\delta}$ (PBSCF); $La_{0.6}Sr_{0.4}Co_{0.2}Fe_{0.8}O_{3-\delta}$-$BaCoO_{3-\delta}$ (PBCC-BCO); $Ba_{1-x}Gd_{0.8}La_{0.2+x}Co_2O_{6-\delta}$ (BGLC); $PrBa_{0.8}Ca_{0.2}Co_2O_{5+\delta}$-$BaCoO_{3-\delta}$ (PBCC-BCO); $Pr_2NiO_{4+\delta}$ (PNO); $Y_{0.8}Er_{0.2}BaCo_{3.2}Ga_{0.8}O_{7+\delta}$ (YEBCG); $(Pr_{0.9}La_{0.1})_2(Ni_{0.8}Cu_{0.2})O_{4+\delta}$ (PLNCu).

Abbreviations of electrolyte and cathode: $BaZr_{0.4}Ce_{0.4}Y_{0.2}O_{3-\delta}$ (BZCY442); $BaZr_{0.3}Ce_{0.5}Y_{0.2}O_{3-\delta}$ (BZCY352); $BaZr_{0.8}Y_{0.2}O_{3-\delta}$ (BZY82); $BaZr_{0.1}Ce_{0.7}Y_{0.2}O_{3-\delta}$ (BZCY172); $BaZr_{0.5}Ce_{0.3}Y_{0.2}O_{3-\delta}$ (BZCY532); $BaZr_{0.1}Ce_{0.7}Y_{0.1}Yb_{0.1}O_{3-\delta}$ (BZCYYb1711); $BaZr_{0.4}Ce_{0.4}Y_{0.1}Yb_{0.1}O_{3-\delta}$ (BZCYYb4411); $BaZr_{0.1}Ce_{0.7}Y_{0.2-x}Yb_xO_{3-\delta}$ (BZCYYb); $BaZr_{0.7}Ce_{0.2}Y_{0.1}O_{3-\delta}$ (BZCY721); $BaZr_{0.1}Ce_{0.68}Y_{0.1}Yb_{0.1}Cu_{0.02}O_{3-\delta}$ (BZCYYbCu); $La_2Ce_2O_7$ (LCO); $BaZr_{0.2}Ce_{0.6}Y_{0.2}O_{3-\delta}$ (BZCY262).

1.5.2 Stability of electrolyte

The electrolyte material for P-SOEC is required to be thermodynamically stable in both reducing (cathode) and high-humidified, oxidizing atmosphere (anode). The most widely used electrolyte materials for P-SOECs are $Ba(Zr,Ce,M)O_{3-\delta}$ solid solutions because highly-conducting $BaCeO_{3-\delta}$ is rather unstable in humidified atmospheres but poorly-conducting $BaZrO_{3-\delta}$ is highly tolerant to H_2O.[112] The steam tolerance in $Ba(Zr,Ce,M)O_{3-\delta}$ electrolyte is increased with the Zr contents of B-Site cations. Zhong et al. evaluated the thermo-chemical stability by changing the ratio of Ce to Zr in $BaZr_{0.9-x}Ce_xY_{0.1}O_{2.95}$, in which the sintered pellets were first treated in boiling water and then heated in CO_2 atmosphere at 900 °C for 2 h. Only the phase with $x \leq 0.5$ remain unchanged through the durability tests.[113] Fabbri et al. also conducted the similar durability tests for $BaZr_{0.8-x}Ce_xY_{0.2}O_{3-\delta}$, demonstrating the excellent CO_2 and H_2O tolerance for phase with $x \leq 0.3$.[114] Many works have reported that $BaZr_{0.1}Ce_{0.7}Y_{0.1}Yb_{0.1}O_{3-\delta}$ (BZCYYb1711) based cells are decomposed by running with concentrated H_2O and CO_2 at 500-900 °C for 100 h.[62,115–117] These findings strongly suggest that the Zr content in $BaZr_{1-x-y}Ce_xM_yO_{3-\delta}$ should be higher than 0.5 for P-SOECs used in high H_2O partial pressure (p_{H2O}) conditions.

It is obviously important to enhance steam electrolysis performance of P-SOECs with high Zr content $BaZr_{1-x-y}Ce_xM_yO_{3-\delta}$ electrolyte. Zr-rich side $BaZr_{1-x-y}Ce_xM_yO_{3-\delta}$ causes large ohmic resistances in P-SOECs, because such electrolyte involves large grain boundary resistances due to the high refractory nature of $BaZrO_3$, as mentioned before. Therefore, it is great challenge to fabricate highly efficient P-SOECs with relatively high Zr content (≥ 0.5) electrolytes. The cells with $BaZr_{0.9}Y_{0.1}O_{3-\delta}$ (BZY91),[82] $BaZr_{0.8}Y_{0.2}O_{3-\delta}$ (BZY82),[87] $BaZr_{0.7}Ce_{0.2}Y_{0.1}O_{3-\delta}$ (BZCY721)[95] were investigated, while their electrolysis currents were limited to 0.05, 0.21, and 0.11 A cm^{-2} at 600 °C under 1.3V, respectively. Hence the studies on Zr-rich side electrolysis cells are rather few.

1.5.3 Current leakage and Faradaic efficiency

In $Ba(Zr,Ce,M)O_{3-\delta}$ electrolyte, the proton defects ($OH_O^{\bullet}$) are formed by the incorporation of water vapor with association of oxygen vacancies ($V_O^{\bullet\bullet}$) via thermodynamic hydration by Equation (1-10):

$$O_O^{\times} + V_O^{\bullet\bullet} + H_2O \longrightarrow 2OH_O^{\bullet} \tag{1-10}$$

Here, $O_O^{\times}$ is the lattice oxygen. The equilibrium constant of hydration reaction and the concentration of proton can be expressed by Equation (1-11) and (1-12), respectively.

$$K_{hydration} = \frac{[OH_O^{\bullet}]^2}{[O_O^{\times}][V_O^{\bullet\bullet}]p_{H_2O}} \tag{1-11}$$

$$[OH_O^{\bullet}] = K_{hydration}^{1/2}[O_O^{\times}]^{1/2}[V_O^{\bullet\bullet}]^{1/2}p_{H_2O}^{1/2} \tag{1-12}$$

The anode side is exposed to oxidizing atmosphere, and, therefore, the association between oxygen vacancies and oxygen gas is equilibrated by Equation (1-13) at the same time.

$$V_O^{\bullet\bullet} + \frac{1}{2}O_2 \longrightarrow O_O^{\times} + 2h^{\bullet} \tag{1-13}$$

Here, $h^{\bullet}$ is electron hole. The oxidation reaction equilibrium constant and the concentration of hole can be expressed as Equation (1-14) and (1-15), respectively.

$$K_{oxidation} = \frac{[h^{\bullet}]^2[O_O^{\times}]}{[V_O^{\bullet\bullet}]p_{O_2}^{1/2}} \tag{1-14}$$

$$[h^{\bullet}] = K_{oxidation}^{1/2}[O_O^{\times}]^{-1/2}[V_O^{\bullet\bullet}]^{1/2}p_{O_2}^{1/4} \tag{1-15}$$

In fact, the $Ba(Zr,Ce,M)O_{3-\delta}$ electrolytes have mixed protonic, oxide ionic and electronic triple conductivity, and thus, the migration of $h^{\bullet}$ carries from the anode side to the cathode side causes serious electron leakage, resulting in a decrease in Faradaic efficiency (Figure 1-8). Combining Equation (1-12) and (1-15), the hole concentration can be descripted as a function of steam and oxygen partial pressures (p_{H2O} and p_{O2}, respectively), as shown in Equation (1-16).

$$[h^{\bullet}] = K_{hydration}^{-1/2} K_{oxidation}^{1/2} [OH_O^{\bullet}][O_O^{\times}]^{-1} p_{H_2O}^{-1/2} p_{O_2}^{1/4} \quad (1\text{-}16)$$

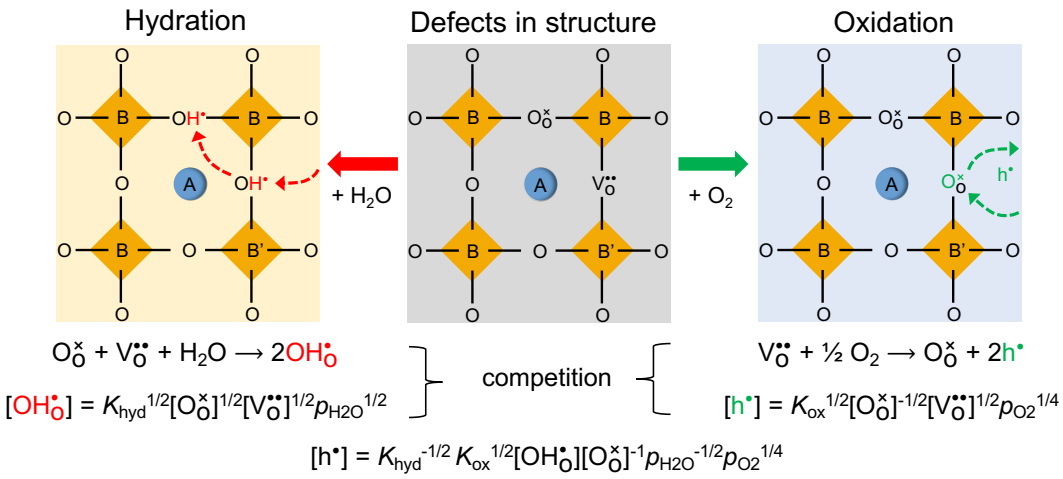

Figure 1-8 Schematic illustration of competition between hydration and oxidation reactions.

The proton concentration exhibits positive and negative correlation with p_{H2O} and p_{O2}, respectively, which means the gas composition of anode has a direct influence on the Faradaic efficiency. Juaristi et al. reported the effect of temperature, p_{O2} and p_{H2O} on the electrical transport numbers of $BaZr_{0.7}Ce_{0.2}Y_{0.1}O_{3-\delta}$ (BZCY721) dense ceramic electrolyte, revealing that the protonic transport number (t_H) is about 0.95 at $p_{O2} = 10^{-5}$ atm while it decreases to 0.63 at $p_{O2} = 0.2$ atm at 600 °C in wet condition ($p_{H2O} = 0.022$ atm) due to the increment of the electronic transport number (t_h). On the other hand, t_H becomes larger with p_{H2O},[118] which agrees with Equation (1-12). The measurement conditions are very important to achieve high Faradaic efficiency, and the lower p_{O2} and higher p_{H2O} must be favorable to increase the efficiency. Some P-SOECs already obtained very high current density over 600 °C. However, oxidation reaction is dominant to hydration reaction in such high temperature region because the enthalpy of oxidation (–135 kJ mol^{-1} for BZY82) is more negative than that of hydration (–93.3 kJ mol^{-1} for BZY82).[119] Therefore, hydrogen production by P-SOECs should be conducted at temperatures below 600 °C in order to gain high Faradaic efficiency.

Many investigations have demonstrated the electronic conductivity is closely related

to the composition of electrolyte materials.[78,120–123] Zhu et al. calculated the Faradaic efficiency of $BaZr_{0.8}Y_{0.2}O_{3-\delta}$ (BZY82) and $BaZr_{0.1}Ce_{0.7}Y_{0.1}Yb_{0.1}O_{3-\delta}$ (BZCYYb1711) based P-SOEC by considering the fluxes of three charge carries inside electrolyte under electrolysis conditions in terms of a Nernst-Planck model, which forecasts BZCYYb1711 based cell has a much higher protonic transfer number than BZY82 based cell, thereby the former exhibiting higher Faradaic efficiency than latter.[121,122] In more recent year, this calculation results were verified by Duan et al. with electrolysis tests of BZCYYb1711 and BZY82 cells.[78] Hence it is a great challenge to explore the new way to reduce the hole leakage of P-SOECs based one Zr-rich side electrolyte materials.

Equation (1-16) can be converted to Equation (1-17) by using the electrochemical potential of the anode reaction represented by Equation (1-18).

$$[\mathrm{h}^{\bullet}] = K_{\mathrm{hydration}}^{-1/2} K_{\mathrm{oxidation}}^{1/2} \exp\left(\frac{F(E - E_{\mathrm{an}})}{RT}\right) \tag{1-17}$$

$$E = E_{\mathrm{an}} + \frac{RT}{2F} \ln \frac{p_{\mathrm{O_2}}^{1/2} [\mathrm{H^+}]^2}{p_{\mathrm{H_2O}}} \tag{1-18}$$

Here E_{an} is potential at anode/electrolyte interface and is proportional to the anode reaction resistances. This strongly suggests that hole leakage can be minimized if the anode reaction resistance is sufficiently lowered with a use of highly active anode materials.

Table 1-6 Faradaic efficiency of P-SOECs in recent years.

Electrolyte	Anode		Temperature (°C)	Faradaic efficiency (%)	Ref
	Material	Gas (Air)			
BZCYZn	LSM-BZCYZn-Co_3O_4	10% H_2O	800	43	124
BZCYZn	LSM-BZCYZn-Fe_2O_3	5% H_2O	800	55	125
BZCYZn	LSCF-BZCYZn	3% H_2O	800	38	126
BZCYZn	BSCF-BZCYZn	3% H_2O	800	44	
BZCYZn	LSMSc	5% H_2O	700	72	127
BZCY721	BGLC	50% H_2O	600	53	95
BZCY721	BGLC-BZCY721	50% H_2O	600	88	
BZY82	SFM-BZY82	3% H_2O	600	64	87
BZY82	SFM-BZY82	3% H_2O	550	54	88
BZY82	SFM-BZY82	3% H_2O	550	44	88
BZCY532	SEFC-BZCY532	10% H_2O	700	20	89
BZCY352	SLF	20% H_2O	700	25	90
BZCYYb4411	PNC	15% H_2O	550	83	102
			500	86	
BZCYYb4411	PBSCF	3% H_2O	600	46	79
			550	58	
			500	71	
BZCYYb1711	BCFZY	20% H_2O	600	~97	78
		10% H_2O	550	~90	
BZCYYb1711	PBCC-BCO	30% H_2O	600	82	103
		3% H_2O	500	80	
		20% H_2O		89	
		30% H_2O		94	

Abbreviations of electrolyte: $BaZr_{0.3}Ce_{0.5}Y_{0.16}Zn_{0.04}O_{3-\delta}$ (BZCYZn); $BaZr_{0.7}Ce_{0.2}Y_{0.1}O_{3-\delta}$ (BZCY721); $BaZr_{0.8}Y_{0.2}O_{3-\delta}$ (BZY82); $BaZr_{0.5}Ce_{0.3}Y_{0.2}O_{3-\delta}$ (BZCY532); $BaZr_{0.3}Ce_{0.5}Y_{0.2}O_{3-\delta}$ (BZCY352); $BaZr_{0.4}Ce_{0.4}Y_{0.1}Yb_{0.1}O_{3-\delta}$ (BZCYYb4411); $BaZr_{0.1}Ce_{0.7}Y_{0.1}Yb_{0.1}O_{3-\delta}$ (BZCYYb1711).

Abbreviations of anode: $La_{0.8}Sr_{0.2}MnO_{3-\delta}$ (LSM); $La_{0.6}Sr_{0.4}Co_{0.2}Fe_{0.8}O_{3-\delta}$ (LSCF); $Ba_{0.5}Sr_{0.5}Co_{0.8}Fe_{0.2}O_{3-\delta}$ (BSCF); $La_{0.8}Sr_{0.2}Mn_{0.95}Sc_{0.05}O_{3-\delta}$ (LSMSc); $Ba_{1-x}Gd_{0.8}La_{0.2+x}Co_2O_{6-\delta}$ (BGLC); $Sr_2Fe_{1.5}Mo_{0.5}O_{6-\delta}$ (SFM); $SrEu_2Fe_{1.8}Co_{0.2}O_{7-\delta}$ (SEFC); $Sr_{2.8}La_{0.2}Fe_2O_{7-\delta}$ (SLF); $PrNi_{0.5}Co_{0.5}O_{3-\delta}$ (PNC); $PrBa_{0.5}Sr_{0.5}Co_{2-x}Fe_xO_{5+\delta}$ (PBSCF); $BaCo_{0.4}Fe_{0.4}Zr_{0.1}Y_{0.1}O_{3-\delta}$ (BCFZY); $PrBa_{0.8}Ca_{0.2}Co_2O_{5+\delta}$-$BaCoO_{3-\delta}$ (PBCC-BCO).

1.5.4 Importance of anode/electrolyte interface

The microstructures near the interface between the anode and electrolyte have not been significantly studied, although the interfacial contact is crucial for the proton transfer from anode to electrolyte and/or to elongate the reaction zones near TPB. The fabrication of P-SOECs usually includes two steps; the first step is the preparation of half-cell comprising electrolyte thin films supported on porous cermet cathode by sintering the green body at high temperature (≥ 1400 °C). In the second step, anode ink is screen-printed on the $Ba(Zr,Ce,M)O_{3-\delta}$ electrolyte and calcined at moderate temperature below 1000 °C to improve the adhesion between anode and electrolyte. It is easily presumed that interdiffusion occurs between anode/electrolyte by the calcination at the 2nd step and the interfacial layers thus formed must be crucial to the activity of TPB reaction sites and/or interfacial proton transfers. Therefore, it is strongly motivated to design the microstructure at anode/electrolyte interfaces for enhancing the performance of P-SOECs.

Recently, Bian et al. focused on the true contact of anode/electrolyte interface and proposed an acid treatment to rejuvenate the high-temperature annealed $BaZr_{0.1}Ce_{0.7}Y_{0.1}Yb_{0.1}O_{3-\delta}$ (BZCYYb1711) electrolyte surface before bonding anode.[80] They demonstrated such treatment could fully recover the theoretical bulk proton conductivity in electrochemical cells and significantly increased the cell currents from 0.70 A cm^{-2} to 1.86 A cm^{-2} at 600 °C under 1.30 V with decreasing the anode resistance from 0.17 to 0.08 Ω cm^2 at 600 °C and OCV, respectively. The ohmic resistance also decreased from 0.20 to 0.09 Ω cm^2 by such treatment. The authors mentioned that some new phase was formed at anode/electrolyte interface during 2nd step calcination of the etched cells and this interfacial layer encouraged the strong adhesion between electrolyte and anode.[80] These results provide an important insight that the interfacial new phase formed between anode and electrolyte makes an important role to elongate the proton-accessible, electrochemical area at the anode sides. Combined these results and Equation (1-17), it is plausible that such interfacial modification may lower the hole leakage by decreasing the anode potential E_{an}.

Matsuzaki et al. proved that current leakage of BZY82 electrolyte became 200 times smaller when $La_{28-x}W_{4+x}O_{54+\delta}$ (LWO) film was introduced between electrolyte and anode by means of numerical simulations. Unfortunately, the area specific resistance (ASR) of electrolyte was largely increased owing to the lack of proton conductivity of LWO. However, these results strongly suggest hole blocking layer of optimal oxide films provide another possible approach to mitigate the current leakage and achieve high Faradic efficiency.[128] In conclusion, the modification of anode/electrolyte interface is efficient way to improve simultaneously the anode reaction resistance and Faradaic efficiency and thus the overall performance of P-SOECs. Hence it is strongly motivated us to design the interface layer between electrolyte and anode, i.e., forming anode functional interlayer (AFL) on $Ba(Zr,Ce,M)O_{3-\delta}$ based P-SOECs.

As mentioned in Figure 1-8, the low Faradaic efficiency in P-SOECs is due to the drift/diffusion of $h^{\bullet}$ defects from anode to cathode side, which is greatly influenced by p_{O2} and p_{H2O} at anode/electrolyte interface as shown in Equation (1-16). According to this, the modification of the anode/electrolyte interface using AFL could lower the hole leakage by another mechanism. For instance, in the case of cell without modification, Figure 1-9a represents schematically the oxygen and water chemical potential terms, i.e., $\ln p_{O2}$ and $\ln p_{H2}$, respectively across electrolyte. p_{O2} and p_{H2O} are oxygen and water partial pressures in the anode gases, respectively. After incorporating dense AFL, the drop of $\ln p_{O2}$ and $\ln p_{H2}$ in AFL must be different from that in electrolyte, thus it's highly possible to achieve high $p_{O_2}^{int}$ and low $p_{H_2O}^{int}$ at electrolyte surfaces as shown in Figure 1-9b, which is favourable to depress $h^{\bullet}$ formation and increase the Faradaic efficiency.

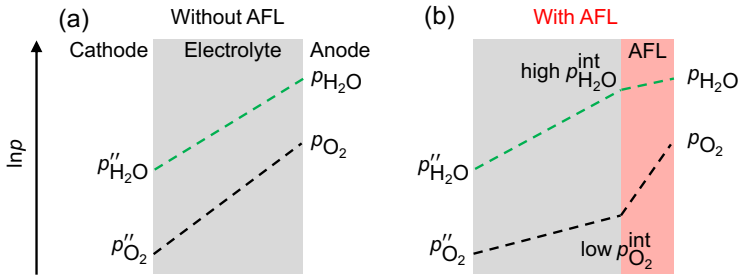

Figure 1-9 Oxygen and water chemical potentials across electrolyte.

1.6 Motivation and objective of this thesis

It is a great challenge to improve the current outputs and durability of P-SOECs based on the $Ba(Zr,Ce,M)O_{3-\delta}$ electrolytes. As listed in Table 1-4, only few groups reported current densities of P-SOECs exceeding 1 A cm^{-2} at 600 °C under thermal neutral potential (near 1.30 V),[79,80,103] which is falling behind that (~2 A cm^{-2} at 750 °C) of SOECs summarized in Table 1-3. One of the reasons for low currents is the large anode reaction resistance because of the carrier mismatch between anode and electrolyte by using conventional O^{2-}/e^{-} double conductors as anode, which limits effective reaction area, that is, the gas-anode-electrolyte triple-phase boundary (TPB).

The further challenge in P-SOECs is to decrease the hole leakage in $Ba(Zr,Ce,M)O_{3-\delta}$ electrolytes. There are many reports on the steam electrolysis currents for P-SOECs (Table 1-4), whereas there exist only a few reports on the conversion efficiency from current to hydrogen production (usually, Faradaic efficiency), as shown in Table 1-6. The highest efficiency (~97% with applied current of 1.00 A cm^{-2} at 600 °C) was achieved in Ce-rich side $BaZr_{0.1}Ce_{0.7}Y_{0.1}Yb_{0.1}O_{3-\delta}$ (BZCYYb1711) electrolyte cells.[78] On the other hand, the efficiency is limited in below 60% for the cells comprising thermodynamically-stable, Zr-rich side $Ba(Zr,Ce,M)O_{3-\delta}$ electrolytes; $BaZr_{0.5}Ce_{0.3}Y_{0.2}O_{3-\delta}$ (BZCY532) base cells exhibit only 20% efficiency with a current of 0.30 A cm^{-2} at 700 °C and 46% of $BaZr_{0.4}Ce_{0.4}Y_{0.1}Yb_{0.1}O_{3-\delta}$ (BZCYYb4411) base cells with current of 1.40 A cm^{-2} at 600 °C.[79,89] These deteriorated efficiencies are attributed to the relatively low $K_{hydration}/K_{oxidation}$ ration in Equation (1-16). The enthalpy of hydration reaction (Equation (1-10)) for BZY91 is about –80.00 kJ mol^{-1} which is more positive than that of BCY91 (–138.00 kJ mol^{-1}), and thus $K_{hydration}$ of BZY91 is smaller than that of BCY91. At the same time, the enthalpy of oxidation reaction (Equation (1-13)) for BZY91 (–38.08 kJ mol^{-1}) is more negative than BCY91 (9.8 kJ mol^{-1}), and thus $K_{oxidation}$ of the former is larger than that of the latter.[129,130] Combined these with Equation (1-16) clearly indicate that Zr-rich $BaZr_{1-x-y}Ce_xM_yO_{3-\delta}$ may cause more serious current leakage than Ce-rich one in P-SOECs. Nevertheless, $BaZr_{1-x-y}Ce_xM_yO_{3-\delta}$ can avoid the decomposition to $Ba(OH)_2$ or $BaCO_3$ only when $1-x-y >$

0.5,[113,114] and thus such composition is desirable for a practical electrolyte for P-SOECs. Hence, in the studies of P-SOECs, the other critical issue is to increase electrolysis current of Zr-rich electrolyte-based cells together with high Faradaic efficiency.

As mentioned in 1.5.4, modification of anode and electrolyte interface by functional oxide thin films, i.e., anode functional layer (AFL) may enable the simultaneous optimization of anode reaction resistance and Faradaic efficiency of P-SOECs. Such improvement of resistance may be attributed to the elongate reaction zones near TPB, thus promoting the anode reaction and proton transfer from anode to electrolyte. Therefore, AFL has possibility to decrease overpotential and achieve a lower hole concentration ($[h^{\bullet}]$). In addition, if the AFL can modify the p_{O2} and p_{H2O} at anode/electrolyte interface as illustrated in Figure 1-9, AFL can prevent hole injection to electrolyte and thus $[h^{\bullet}]$ will be further decreased, thus achieving higher Faradaic efficiency. The main objective of this thesis is to explore novel AFL for P-SOECs with high Zr-content electrolyte to aim the development of the device with excellent performance and long-term durability. In this thesis, various thin films with different structures and transport properties were employed as AFL at the anode/electrolyte interface for P-SOECs with $BaZr_{0.6}Ce_{0.2}Y_{0.1}Yb_{0.1}O_{3-\delta}$ (BZCYYb6211) electrolyte, and its effects on Faradaic efficiency and anode reaction resistance were evaluated. The functionality of AFL was verified by means of electrochemical analysis, and finally, the P-SOECs with very high Faraday efficiency and current density were demonstrated. Thus, this thesis gives a general guidance of design principles of AFL for highly efficient P-SOECs operating at relatively low temperatures.

1.7 Contents of this thesis

This thesis consists of 6 chapters as follows.

Chapter 1 introduces the backgrounds, unique advantages, and recent developments of protonic solid oxide electrolysis cells (P-SOECs) operating at intermediate temperatures and summarizes the challenges blocking the improvement of electrochemical performance in P-SOECs. The motivations and objectives were also described.

Chapter 2 gives the general experiments about material synthesis, AFL deposition techniques and characterization methods.

Chapter 3 demonstrated that the electrolysis performance of the cell with a high Zr content electrolyte $BaZr_{0.6}Ce_{0.2}Y_{0.1}Yb_{0.1}O_{3-\delta}$ (BZCYYb6211) could be drastically improved by a use of $La_{0.5}Sr_{0.5}CoO_{3-\delta}$ (LSC) thin film (~90 nm) as an anode functional layer (AFL). Electrochemical measurements proved that LSC AFL significantly reduced the barrier height for electrochemical proton incorporation reaction at gas-electrolyte-electrode triple phase boundary. Hence both ohmic and polarization resistances of the BZCYYb6211 cell decreased from 0.52 and 0.98 Ω cm^2 to 0.26 and 0.57 Ω cm^2, respectively, with the LSC AFL at 600 °C, and thus achieved a high electrolysis current 1.22 A cm^{-2} at 1.3 V, which was equivalent to that of the cell with a state-of-the-art electrolyte BZCYYb1711 (1.13 A cm^{-2}). BZCYYb6211 with LSC AFL showed good durability at 500 °C under high steam condition with an applied current of 1 A cm^{-2} over for 100 hours, and Faradaic efficiency about 70% was achieved.

In chapter 4, a series of double- or triple-conducting oxides $LaSrCoO_{4+\delta}$ (LSC4) $La_{0.5}Sr_{0.5}CoO_{3-\delta}$ (LSC), $LaNiO_{3-\delta}$ (LNO) or $Ba_{0.95}La_{0.05}Fe_{0.8}Zn_{0.2}O_{3-\delta}$ (BLFZ), $BaCo_{0.4}Fe_{0.4}Zr_{0.1}Y_{0.1}O_{3-\delta}$ (BCFZY), $BaPr_{0.8}Y_{0.2}O_{3-\delta}$ (BPY), $PrBa_{0.5}Sr_{0.5}Co_{1.5}Fe_{0.5}O_{3-\delta}$ (PBSCF) were applied as AFLs (~100–140 nm) between the $La_{0.6}Sr_{0.4}Co_{0.2}Fe_{0.8}O_{3-\delta}$ (LSCF) anode and BZCYYb6211 electrolyte in P-SOECs. The steam electrolysis performance and efficiency of P-SOECs could be drastically improved by the use of $H^+/O^{2-}/e^-$ triple conducting BLFZ thin film as AFL. The electrochemical analysis clarified that BLFZ AFL could significantly promote interfacial proton transfer at

anode-electrolyte interfaces, resulting in low interfacial resistivity, and provide the proton-accessible reaction zones extended overall the surfaces of AFL. These features enable promoting the anodic reaction without long range surface diffusion of oxygen species from gas-anode-electrolyte triple phase boundary (TPB) to LSCF anode surfaces. The BLFZ cell offered an electrolysis current of 0.57 A cm^{-2} at 1.3 V at 600 °C, which was higher than reported cells with LSCF as anode. And interestingly, the Faradaic efficiency increased from 46% for a cell without the BLFZ AFL to 75% for BLFZ cell at 500 °C. These results proved that BLFZ could depress the hole in electrolyte because the water partial pressure retained to relatively high in comparison to oxygen partial pressure at AFL/electrolyte interface due to the excellent proton conductivity.

In chapter 5, the thickness of BLFZ AFL was optimized for the cells with $H^+/O^{2-}/e^-$ triple conducting PBSCF anode, indicating a favorable thickness is in the range of 90-170 nm. The P-SOEC with 150 nm BLFZ AFL gained highest electrolysis current at 1.3 V bias equaling to 0.83 A cm^{-2} at 600 °C. The cell exhibited very high Faradaic efficiency of 71% in 0.74 A cm^{-2} and 82% in 0.22 A cm^{-2} at 600 and 500 °C, which was the highest values of the P-SOECs with high Zr-content electrolyte (BZCYYb6211). Moreover, the polarization resistance of the corresponding cells was lower than that of reported cells yielding similar electrolysis current, indicating the anode reaction kinetics were greatly boosted by the synergy of BLFZ AFL and PBSCF anode. Nevertheless, the cells using BLFZ anodes exhibited inferior performance, demonstrating the AFL make a different role from that of anode in the anode reaction. These results revealed that AFL could be a strong and effective tool to design P-SOECs with excellent performance for green hydrogen production.

Chapter 6 gives the overall summary and conclusion of this thesis.

1.8 References

1. IPCC (2007) Climate Change 2007: The Physical Science Basis. Eds. S. Solomon, et al.; Cambridge University Press, Cambridge, United Kingdom and New York, NY, USA.
2. Center for Sustainable Systems, University of Michigan. 2021. "Greenhouse Gases Factsheet." Pub. No. CSS05-21.
3. IPCC (2014) Climate Change 2014: Mitigation of Climate Change. O. Edenhofer, et al. Cambridge University Press, Cambridge, United Kingdom and New York, NY, USA.
4. H. Ritchie, M. Roser and P. Rosado. *Our world in data*, 2020.
5. P Agreement. Paris agreement. Report of the conference of the parties to the united nations framework convention on climate change (21st session, 2015: Paris), vol. 4, Retrived December (2015, December) 2017.
6. M. Salvia, D. Reckien, F. Pietrapertosa, *et al.*, *Renew. Sustain. Energy Rev.*, 2021, **135**. 110253.
7. X. Zhao, X. Ma, B. Chen, Y. Shang and M. Song, *Resour. Conserv. Recycl.*, 2022, **176**. 105959.
8. I. Dincer. *Renew. Sustain. Energy Rev.*, 2000, **4**, 157–175.
9. R. Gross, M. Leach and A. Bauen, *Environ. Int.*, 2003, **29**, 105–122.
10. E. T. Sayed, T. Wilberforce, K. Elsaid, M. K. H. Rabaia, M. A. Abdelkareem, K. J. Chae and A. G. Olabi, *Sci. Total Environ.*, 2021, **766**, 144505.
11. R. G. Grim, Z. Huang, M. T. Guarnieri, J. R. Ferrell, L. Tao and J. A. Schaidle, *Energy Environ. Sci.*, 2020, **13**, 472–494.
12. Y. Zheng, J. Wang, B. Yu, W. Zhang, J. Chen, J. Qiao and J. Zhang, *Chem. Soc. Rev.*, 2017, **46**, 1427–1463.
13. G. Notton, M.-L. Nivet, C. Voyant, C. Paoli, C. Darras, F. Motte and A. Fouilloy, *Renew. Sustain. Energy Rev.*, 2018, **87**, 96–105.
14. K. Møller, D. Sheppard, D. Ravnsbæk, C. Buckley, E. Akiba, H.-W. Li and T. Jensen, *Energies*, 2017, **10**, 1645.
15. I. K. Kapdan and F. Kargi, *Enzyme Microb. Technol.*, 2006, **38**, 569-582.
16. W. Liu, Y. Cui, X. Du, Z. Zhang, Z. Chao and Y. Deng, *Energy Environ. Sci.*, 2016, **9**, 467-472.
17. Patel, S. Countries Roll Out Green Hydrogen Strategies, Electrolyzer Targets. Power: News & Technology for the Global Energy Industry, 1 February 2021.
18. E. Bianco and H. Blanco, IRENA (2020), Green Hydrogen: A guide to policy making. International Renewable Energy Agency, Abu Dhabi.
19. U. Albrecht, U. Bünger, J. Michalski, T. Raksha, R. Wurster, and J. Zerhusen, International Hydrogen Strategies—A study commissioned by and in cooperation

with the World Energy Council Germany, 2020.
20. T. Capurso, M. Stefanizzi, M. Torresi and S. M. Camporeale, *Energy Convers. Manage.*, 2022, **251**, 114898.
21. F. Dawood, M. Anda and G. M. Shafiullah, *Int. J. Hydrogen Energy*, 2020, **45**, 3847–3869.
22. J. Chi and H. Yu, *Chin. J. Catal.*, 2018, **39**, 390–394.
23. S. Y. Tee, K. Y. Win, W. S. Teo, L. D. Koh, S. Liu, C. P. Teng and M. Y. Han, *Adv. Sci.*, 2017, **4**, 1600337.
24. M. David, C. Ocampo-Martínez and R. Sánchez-Peña, *J. Energy Storage*, 2019, **23**, 392–403.
25. J. D. Holladay, J. Hu, D. L. King and Y. Wang, *Catal. Today*, 2009, **139**, 244–260.
26. H. Zhang, Z. Sun and Y. H. Hu, *Renew. Sustain. Energy Rev.*, 2021, **149**, 111330.
27. F. M. Sapountzi, J. M. Gracia, C. J. Weststrate, H. O. A. Fredriksson and J. W. Niemantsverdriet, *Pro. Energy Combust. Sci.*, 2017, **58**, 1–35.
28. M.B.I. Janjua and R.L. Leroy, *Int. J. Hydrogen Energy*, 1985, **10**, 11–19.
29. K. Zeng and D. Zhang, *Pro. Energy Combust. Sci.*, 2010, **36**, 307–326.
30. H. A. Miller, K. Bouzek, J. Hnat, S. Loos, C. I. Bernäcker, T. Weißgärber, L. Röntzsch and J. Meier-Haack, *Sustainable Energy Fuels*, 2020, **4**, 2114–2133.
31. J. R. Varcoe, P. Atanassov, D. R. Dekel, A. M. Herring, M. A. Hickner, P. A. Kohl, A. R. Kucernak, W. E. Mustain, K. Nijmeijer, K. Scott, T. Xu and L. Zhuang, *Energy Environ. Sci.*, 2014, **7**, 3135–3191.
32. L. Xiao, S. Zhang, J. Pan, C. Yang, M. He, L. Zhuang and J. Lu, *Energy Environ. Sci.*, 2012, **5**, 7869–7871.
33. S. D. Ebbesen, S. H. Jensen, A. Hauch and M. B. Mogensen, *Chem. Rev.*, 2014, **114**, 10697–10734.
34. L. Mingyi, Y. Bo, X. Jingming and C. Jing, *J. Power Sources*, 2008, **177**, 493–499.
35. A. Buttler and H. Spliethoff, *Renew. Sustain. Energy Rev.*, 2018, **82**, 2440–2454.
36. National Institute of Standards and Technology (NIST) Chemistry WebBook, Standard Reference Database Number 69 (https://doi.org/10.18434/T4D303).
37. A. Hauch, R. Kungas, P. Blennow, A. B. Hansen, J. B. Hansen, B. V. Mathiesen and M. B. Mogensen, *Science*, 2020, **370**, eaba6118.
38. D. Simwonis, F. Tietz and D. Stover, *Solid State Ionics*, 2000, **132**, 241–251.
39. J.-H. LEE, H. MOON, H.-W. LEE, J. KIM, J.-D. KIM and K.-H. YOON, *Solid State Ionics*, **148**, 15–26.
40. Q. Zhang, Q.-Y. Liu, B.-K. Park, S. Barnett and P. Voorhees, *Acta Mater.*, 2021, **213**,116928.
41. H. Shimada, T. Yamaguchi, H. Kishimoto, H. Sumi, Y. Yamaguchi, K. Nomura and Y. Fujishiro, *Nat. Commun.*, 2019, **10**, 5432.

42. A. Brisse, J. Schefold and M. Zahid, *Int. J. Hydrogen Energy*, 2008, **33**, 5375–5382.
43. J. Laurencin, M. Hubert, D. F. Sanchez, S. Pylypko, M. Morales, A. Morata, B. Morel, D. Montinaro, F. Lefebvre-Joud and E. Siebert, *Electrochim. Acta*, 2017, **241**, 459–476.
44. M. J. López-Robledo, M. A. Laguna-Bercero, A. Larrea and V. M. Orera, *J. Power Sources*, 2018, **378**, 184–189.
45. S.-i. Lee, J. Kim, J.-W. Son, J.-H. Lee, B.-K. Kim, H.-J. Je, H.-W. Lee, H. Song and K. J. Yoon, *J. Power Sources*, 2014, **250**, 15–20.
46. Y. Zhang, M. Han and Z. Sun, *Int. J. Hydrogen Energy*, 2020, **45**, 5554–5564.
47. W. Zhang, B. Yu and J. Xu, *Int. J. Hydrogen Energy*, 2012, **37**, 837–842.
48. F. Chauveau, J. Mougin, J. M. Bassat, F. Mauvy and J. C. Grenier, *J. Power Sources*, 2010, **195**, 744–749.
49. M. A. Laguna-Bercero, N. Kinadjan, R. Sayers, H. El Shinawi, C. Greaves and S. J. Skinner, *Fuel Cells*, 2011, **11**, 102–107.
50. D. Dong, X. Shao, X. Hu, K. Chen, K. Xie, L. Yu, Z. Ye, P. Yang, G. Parkinson and C.-Z. Li, *Int. J. Hydrogen Energy*, 2016, **41**, 19829–19835.
51. M. A. Laguna-Bercero, R. Campana, A. Larrea, J. A. Kilner and V. M. Orera, *J. Power Sources*, 2011, **196**, 8942–8947.
52. N. Ai, S. He, N. Li, Q. Zhang, W. D. A. Rickard, K. Chen, T. Zhang and S. P. Jiang, *J. Power Sources*, 2018, **384**, 125–135.
53. S. H. Jensen, C. Graves, M. Mogensen, C. Wendel, R. Braun, G. Hughes, Z. Gao and S. A. Barnett, *Energy Environ. Sci.*, 2015, **8**, 2471–2479.
54. D. Kim, J. W. Park, M. S. Chae, I. Jeong, J. H. Park, K. J. Kim, J. J. Lee, C. Jung, C.-W. Lee, S.-T. Hong and K. T. Lee, *J. Mater. Chem. A*, 2021, **9**, 5507–5521.
55. S.-L. Zhang, H. Wang, M. Y. Lu, A.-P. Zhang, L. V. Mogni, Q. Liu, C.-X. Li, C.-J. Li and S. A. Barnett, *Energy Environ. Sci.*, 2018, **11**, 1870–1879.
56. B.-K. Park, R. Scipioni, Q. Zhang, D. Cox, P. W. Voorhees and S. A. Barnett, *J. Mater. Chem. A*, 2020, **8**, 11687–11694.
57. K. D. Kreuer, *Annu. Rev. Mater. Res.*, 2003, **33**, 333–359.
58. C. Zuo, S. Zha, M. Liu, M. Hatano and M. Uchiyama, *Adv. Mater.*, 2006, **18**, 3318–3320.
59. L. Yang, S. Wang, K. Blinn, M. Liu, Z. Liu, Z. Cheng and M. Liu, *Science*, 2009, **326**, 126–129.
60. F. Forrat, G. Dauge, P. Trevoux, G. Danner and M. Christen, *Acad. Sci.Paris*, 1964, **259**, 2813–2816.
61. C. W. Tanner and A. V. Virkar, *J. Electrochem. Soc.*, 1996, **143**, 1386–1389.
62. L. Lei, J. Zhang, Z. Yuan, J. Liu, M. Ni and F. Chen, *Adv. Funct. Materials*, 2019, **29**, 1903805.

63. H. Iwahara, T. Yajima and H. Ushida, *Solid State Ionics*, 1994, **70-71**, 267–271.
64. K. D. Kreuer, S. Adams, W. Münch, A. Fuchs, U. Klock and J. Maier, *Solid State Ionics*, 2001, **145**, 295–306.
65. C. Duan, J. Huang, N. Sullivan and R. O'Hayre, *Appl. Phys. Rev.*, 2020, **7**, 011314.
66. K. Yang, J. X. Wang, Y. J. Xue, M. S. Wang, C. R. He, Q. Wang, H. Miao and W. G. Wang, *Ceram. Int.*, 2014, **40**, 15073–15081.
67. J. Kim, S. Sengodan, S. Kim, O. Kwon, Y. Bu and G. Kim, *Renew. Sustain. Energy Rev.*, 2019, **109**, 606–618.
68. G. Geneste, *Solid State Ionics*, 2018, **323**, 172–202.
69. J. Jing, J. Pang, L. Chen, H. Zhang, Z. Lei and Z. Yang, *Chem. Eng. J.*, 2022, **429**, 132314.
70. H. Iwahara, T. Esaka, H. Uchida and N. Maeda, *Solid State Ionics*, 1981, **3-4**, 359–363.
71. F. J. A. Loureiro, N. Nasani, G. S. Reddy, N. R. Munirathnam and D. P. Fagg, *J. Power Sources*, 2019, **438**, 226991.
72. P. Babilo and S. M. Haile, *J. Am. Ceram. Soc.*, 2005, **88**, 2362–2368.
73. J. Tong, D. Clark, M. Hoban and R. O'Hayre, *Solid State Ionics*, 2010, **181**, 496–503.
74. S. Le, J. Zhang, X. Zhu, J. Zhai and K. Sun, *J. Power Sources*, 2013, **232**, 219–223.
75. F. He, D. Song, R. Peng, G. Meng and S. Yang, *J. Power Sources*, 2010, **195**, 3359–3364.
76. P. Babilo, T. Uda and S. M. Haile, *J. Mater. Res.*, 2011, **22**, 1322–1330.
77. Y. Yamazaki, R. Hernandez-Sanchez and S. M. Haile, *Chem. Mater.*, 2009, **21**, 2755–2762.
78. C. Duan, R. Kee, H. Zhu, N. Sullivan, L. Zhu, L. Bian, D. Jennings and R. O'Hayre, *Nat. Energy*, 2019, **4**, 230–240.
79. S. Choi, T. C. Davenport and S. M. Haile, *Energy Environ. Sci.*, 2019, **12**, 206–215.
80. W. Bian, W. Wu, B. Wang, W. Tang, M. Zhou, C. Jin, H. Ding, W. Fan, Y. Dong, J. Li and D. Ding, *Nature*, 2022, **604**, 479–485.
81. M. A. Azimova and S. McIntosh, *Solid State Ionics*, 2011, **203**, 57–61.
82. L. Bi, S. P. Shafi and E. Traversa, *J. Mater. Chem. A*, 2015, **3**, 5815–5819.
83. N. Wang, H. Toriumi, Y. Sato, C. Tang, T. Nakamura, K. Amezawa, S. Kitano, H. Habazaki, Y. Aoki, *ACS Appl. Energy Mater.* 2021, **4**, 554–563.
84. J. Lyagaeva, N. Danilov, G. Vdovin, J. Bu, D. Medvedev, A. Demin and P. Tsiakaras, *J. Mate. Chem. A*, 2016, **4**, 15390–15399.
85. Y. Yoo and N. Lim, *J. Power Sources*, 2013, **229**, 48–57.
86. W. Li, B. Guan, L. Ma, H. Tian and X. Liu, *ACS Appl. Mater. Interfaces*, 2019,

11, 18323–18330.

87. L. Lei, Z. Tao, X. Wang, J. P. Lemmon and F. Chen, *J. Mater. Chem. A*, 2017, **5**, 22945–22951.
88. L. Lei, J. Zhang, R. Guan, J. Liu, F. Chen and Z. Tao, *Energy Conver. Manag.*, 2020, **218**, 113044.
89. D. Huan, N. Shi, L. Zhang, W. Tan, Y. Xie, W. Wang, C. Xia, R. Peng and Y. Lu, *ACS Appl. Mater. Interfaces*, 2018, **10**, 1761–1770.
90. D. Huan, W. Wang, Y. Xie, N. Shi, Y. Wan, C. Xia, R. Peng and Y. Lu, *J. Mater. Chem. A*, 2018, **6**, 18508–18517.
91. S. Yang, Y. Wen, J. Zhang, Y. Lu, X. Ye and Z. Wen, *Electrochim. Acta*, 2018, **267**, 269–277.
92. S. Yang, S. Zhang, C. Sun, X. Ye and Z. Wen, *ACS Appl. Mater. Interfaces*, 2018, **10**, 42387–42396.
93. C. Sun, S. Yang, Y. Lu, J. Wen, X. Ye and Z. Wen, *J. Power Sources*, 2020, **449**, 227498.
94. W. Li, B. Guan, L. Ma, S. Hu, N. Zhang and X. Liu, *J. Mater. Chem. A*, 2018, **6**, 18057–18066.
95. E. Vøllestad, R. Strandbakke, M. Tarach, D. Catalan Martinez, M. L. Fontaine, D. Beeaff, D. R. Clark, J. M. Serra and T. Norby, *Nat. Mater.*, 2019, **18**, 752–759.
96. J. Kim, A. Jun, O. Gwon, S. Yoo, M. Liu, J. Shin, T. H. Lim and G. Kim, *Nano Energy*, 2018, **44**, 121–126.
97. W. Wu, D. Ding and T. He, *ECS Trans.*, 2017, **80**, 167–173.
98. W. Wu, H. Ding, Y. Zhang, Y. Ding, P. Katiyar, P. K. Majumdar, T. He and D. Ding, *Adv. Sci.*, 2018, **5**, 1800360.
99. R. Murphy, Y. Zhou, L. Zhang, L. Soule, W. Zhang, Y. Chen and M. Liu, *Adv. Funct. Mater.*, 2020, **30**, 2002265.
100. Y. Meng, J. Gao, H. Huang, M. Zou, J. Duffy, J. Tong and K. S. Brinkman, *J. Power Sources*, 2019, **439**, 227093.
101. W. Tang, H. Ding, W. Bian, W. Wu, W. Li, X. Liu, J. Y. Gomez, C. Y. Regalado Vera, M. Zhou and D. Ding, *J. Mater. Chem. A*, 2020, **8**, 14600–14608.
102. H. Ding, W. Wu, C. Jiang, Y. Ding, W. Bian, B. Hu, P. Singh, C. J. Orme, L. Wang, Y. Zhang and D. Ding, *Nat. Commun.*, 2020, **11**, 1907.
103. Y. Zhou, E. Liu, Y. Chen, Y. Liu, L. Zhang, W. Zhang, Z. Luo, N. Kane, B. Zhao, L. Soule, Y. Niu, Y. Ding, H. Ding, D. Ding, M. Liu, *ACS Energy Lett.*, 2021, **6**, 1511–1520.
104. J.-S. Shin, H. Park, K. Park, M. Saqib, M. Jo, J. H. Kim, H.-T. Lim, M. Kim, J. Kim and J.-Y. Park, *J. Mater. Chem. A*, 2021, **9**, 607–621.
105. Y. Song, J. Liu, Y. Wang, D. Guan, A. Seong, M. Liang, M. J. Robson, X. Xiong, Z. Zhang, G. Kim, Z. Shao and F. Ciucci, *Adv. Energy Mater.*, 2021, **11**, 2101899.

106. W. Wang, Y. Li, Y. Liu, Y. Tian, B. Ma, J. Li, J. Pu and B. Chi, *ACS Sustainable Chem. Eng.*, 2021, **9**, 10913–10919.
107. T. Kobayashi, K. Kuroda, S. Jeong, H. Kwon, C. Zhu, H. Habazaki and Y. Aoki, *J. Electrochem. Soc.*, 2018, **165**, F342–F349.
108. S. Choi, S. Yoo, J. Kim, S. Park, A. Jun, S. Sengodan, J. Kim, J. Shin, H. Y. Jeong, Y. Choi, G. Kim and M. Liu, *Sci. Rep.*, 2013, **3**, 1–6.
109. S. Rajendran, N. K. Thangavel, H. Ding, Y. Ding, D. Ding and L. M. Reddy Arava, *ACS Appl. Mater. Interfaces*, 2020, **12**, 38275–38284.
110. H. Toriumi, T. Kobayashi, S. Hinokuma, T. Ina, T. Nakamura, K. Amezawa, C. Zhu, H. Habazaki and Y. Aoki, *Inorg. Chem. Front.*, 2019, **6**, 1587–1597.
111. Y. Zhou, W. Zhang, N. Kane, Z. Luo, K. Pei, K. Sasaki, Y. Choi, Y. Chen, D. Ding and M. Liu, *Adv. Funct. Mater.*, 2021, **31**, 2105386.
112. K. H. Ryu and S. M. Haile, *Solid State Ionics*, 1999, **125**, 355–367.
113. Z. Zhong, *Solid State Ionics*, 2007, **178**, 213–220.
114. E. Fabbri, A. Depifanio, E. Dibartolomeo, S. Licoccia and E. Traversa, *Solid State Ionics*, 2008, **179**, 558–564.
115. C. Duan, J. Tong, M. Shang, S. Nikodemski, M. Sanders, S. Ricote, A. Almansoori, R. O'Hayre, Science 2015, 349, 1321–1326.
116. S. Fang, K. S. Brinkman and F. Chen, *J. Membr. Sci.*, 2014, **467**, 85–92.
117. B. Hua, N. Yan, M. Li, Y. F. Sun, Y. Q. Zhang, J. Li, T. Etsell, P. Sarkar and J. L. Luo, *Adv Mater*, 2016, **28**, 8922-8926.
118. G. Heras-Juaristi, D. Pérez-Coll and G. C. Mather, *J. Power Sources*, 2017, **364**, 52–60.
119. E. Vøllestad, H. Zhu and R. J. Kee, *J. Electrochem. Soc.*, 2013, **161**, F114.
120. J. Lagaeva, D. Medvedev, A. Demin and P. Tsiakaras, *J. Power Sources*, 2015, **278**, 436–444.
121. H. Zhu, S. Ricote, C. Duan, R. P. O'Hayre, D. S. Tsvetkov and R. J. Kee, *J. Electrochem. Soc.*, 2018, **165**, F581–F588.
122. H. Zhu, S. Ricote, C. Duan, R. P. O'Hayre and R. J. Kee, *Journal of The Electrochemical Society*, 2018, **165**, F845–F853.
123. D. Han, X. Liu, T. S. Bjørheim and T. Uda, *Adv. Energy Mater.*, 2021, **11**, 2003149.
124. S. Li, R. Yan, G. Wu, K. Xie and J. Cheng, *Int. J. Hydrogen Energy*, 2013, **38**, 14943–14951.
125. H. Li, X. Chen, S. Chen, Y. Wu and K. Xie, *Int. J. Hydrogen Energy*, 2015, **40**, 7920–7931.
126. S. Li, K. Xie, *J. Electrochem. Soc.*, **2013**, 160, F224–F233.
127. L. Gan, L. Ye, M. Liu, S. Tao and K. Xie, *RSC Adv.*, 2016, **6**, 641–647.
128. Y. Matsuzaki, Y. Tachikawa, Y. Baba, K. Sato, G. Kojo, H. Matsuo, J. Otomo, H. Matsumoto, S. Taniguchi and K. Sasaki, *J. Electrochem. Soc.*, 2020, **167**,084515.

129. H. Zhu and R. J. Kee, *Int. J. Hydrogen Energy*, 2016, **41**, 2931–2943.
130. D. K. Lim, H. N. Im, S. J. Song and H. I. Yoo, *Sci. Rep.*, 2017, **7**, 1–9.

Chapter 2 General experiment

2.1 Synthesis of materials for anode and functional layer

The anode powders $La_{0.8}Sr_{0.2}Co_{0.7}Ni_{0.3}O_{3-\delta}$ (LSCN) $PrBa_{0.5}Sr_{0.5}Co_{1.5}Fe_{0.5}O_{3-\delta}$ (PBSCF) $Ba_{0.95}La_{0.05}Fe_{0.8}Zn_{0.2}O_{3-\delta}$ (BLFZ) and most of materials BLFZ, PBSCF, $LaSrCoO_{4+\delta}$ (LSC4), $La_{0.5}Sr_{0.5}CoO_{3-\delta}$ (LSC), $BaCo_{0.4}Fe_{0.4}Zr_{0.1}Y_{0.1}O_{3-\delta}$ (BCFZY), $BaPr_{0.8}Y_{0.2}O_{3-\delta}$ (BPY) for pulsed laser deposition (PLD) targets in this thesis were synthesized by a citrate precursor route as shown in Figure 2-1. The precursor solution of the material (M) was prepared by dissolving the required stoichiometric amounts of nitrates in Milli-Q H_2O with citric acid (CA, $C_6H_8O_7 \cdot H_2O$) as a chelate agent in a mole ratio of M:CA = 1:2. The gelatinous product was obtained by heating and stirring to evaporate H_2O and promote polymerization, in which the temperature of solution was keep at 50–60 °C. The gel was calcined at 500 °C for 1 h. Finally, the ground precursor powder was calcined at a higher temperature, usually 900–1100 °C, to obtain single-phase powders. Particular, in the case of $LaNiO_{3-\delta}$ (LNO), ethylene glycol (MEG, $C_2H_6O_2$) was also added as solvent together with H_2O. The molar ratio of M:CA:MEG was maintained at 1:1.5:3 and the final sintered temperature was 750 °C.[1] And the LNO target was sintered at 850 °C. BPY powders were prepared by ball-milling $BaCO_3$, Pr_6O_{11}, Y_2O_3 for 2 h in 2-propanol and then calcined at 1200 °C for 8 h, the PLD target was sintered at 1500 °C for 12 h.

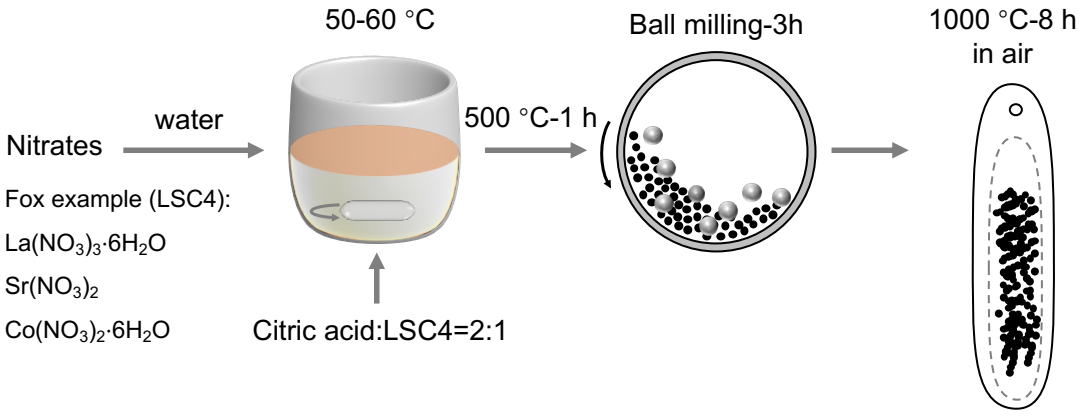

Figure 2-1 Flow chart of the citrate acid method to prepare powders for anode and PLD targets.

2.2 Fabrication of protonic solid oxide electrolysis cells

Before the fabrication of half-cells, $BaZr_xCe_{0.8-x}Y_{0.1}Yb_{0.1}O_{3-\delta}$ electrolyte powders were prepared with stoichiometric quantities of raw materials ($BaCO_3$, ZrO_2, CeO_2, Y_2O_3 and Yb_2O_3) by ball-milling and calcined at 1300 °C for 10 h in air. And then, the cathode-supported protonic solid oxide electrolysis cells were fabricated as shown in Figure 2-2. The porous cathode was prepared by ball-milling NiO, electrolyte powders and starch in ethanol or 2-propanol. After drying, the mixture powders were uniaxially pressed and subsequently isostatically pressed to obtain the pellets. The electrolyte layer was spin-coated on both surfaces of the cathode pellet with a slurry, which was prepared by dispersing electrolyte powders with 1 wt.% NiO into a solution containing dispersant and binder. After sintering in air atmosphere, the back side of formed ceramic pellets was polished with SiC paper to get half-cells. Finally, anode was screen printed on electrolyte or anode functional layer for electrochemical analysis.

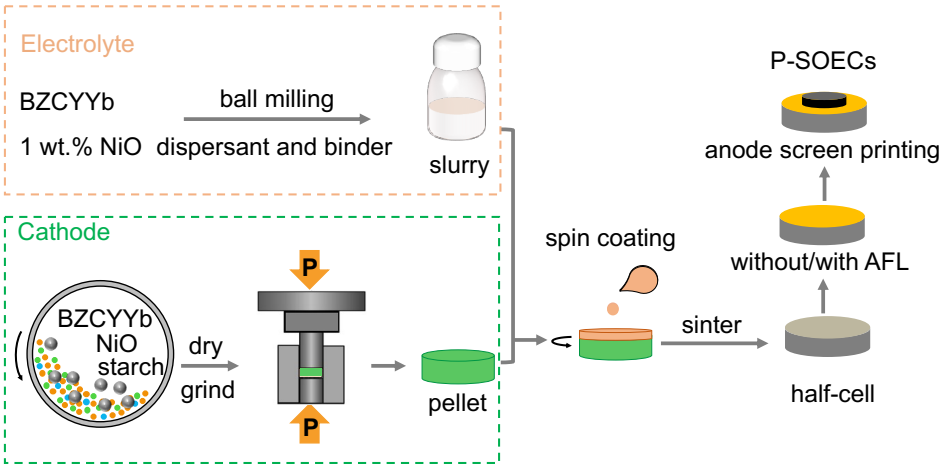

Figure 2-2 The schematic diagram for fabrication of protonic solid oxide electrolysis cells.

2.3 Fabrication of anode functional layer

The anode functional layers (AFLs) in this thesis were prepared by radio frequency (RF) sputtering (chapter 3) and pulsed laser deposition (PLD, chapter 4 and 5), respectively. In the case of RF sputtering, the AFL of $La_{0.5}Sr_{0.5}CoO_{3-\delta}$ (LSC) thin film was deposited on the electrolyte layer at 500 °C. Figure 2-3a simply gives the working principles of RF sputtering. RF sputtering runs an energetic wave through an inert Ar gas in a vacuum chamber which becomes ionized. The LSC target is bombarded by these high energy ions and sputter off atoms as a fine plasma covering the half-cell pellet.

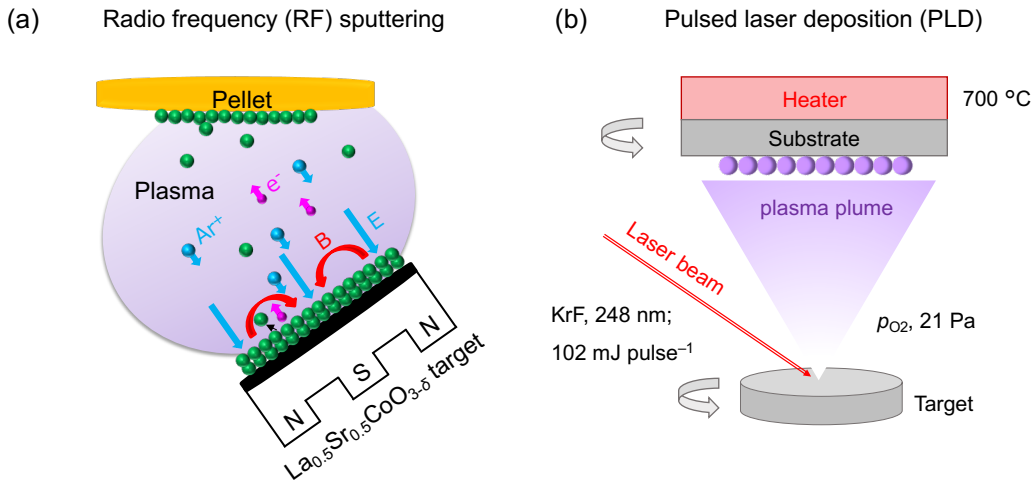

Figure 2-3 Diagram of method for anode functional layer fabrication. (a) Radio frequency (RF) sputtering. (b) Pulsed laser deposition (PLD).

To explore the effect of other oxides as AFLs for P-SOECs, the PLD technology (Figure 2-3b) was applied in this thesis and the corresponding targets were prepared by the synthesised powders in chapter 2.1. PLD is a physical vapor deposition technique, in which, the target is stricken by the high-power laser beam in a vacuum chamber with the presence of oxygen. And then, material is vaporized and deposited as a thin film on the substrate. All AFLs prepared by PLD in this thesis were performed under 700 °C and an oxygen pressure of 21 Pa by a KrF excimer laser (248 nm, Coherence Comp109) with an energy of 102 mJ $pulse^{-1}$ and a repetition rate of 5 Hz.

2.4 Characterization

2.4.1 Phase and microstructure

The phase purity of anode and electrolyte materials was identified by X-ray powder diffraction (XRD, Rigaku, Ultima IV) with Cu Kα radiation at a scan rate of 5° min^{-1} in the 2θ range from 20° to 80°. The phase structure of AFL thin film deposited on a silicon plate was characterized using a grazing incidence X-ray diffractometer (GIXRD, Rigaku, RINT-2000) at a scan speed of 0.5° min^{-1} and a grazing incidence angle of 2°. Field emission scanning electron microscopy (FESEM, SIGMA500, ZEISS) was employed to examine the microstructures of anode powders, AFL surfaces, electrolyte surfaces and P-SOECs. Element mapping and high-resolution transmission electron microscopy (HRTEM) images were obtained using a field-emission TEM (Jeol JEM-2010 or Titan^{3TM} G2 60-300) equipped with an EDS apparatus. The samples for TEM were prepared using the focused ion beam technique (HITACHI FB-2100).

2.4.2 Electrochemical analysis

The slurry of anode materials was screen-printed on the electrolyte or AFL surfaces to obtain the full cells and then P-SOECs were mounted in a laboratory-constructed test station with the seal of a molten glass ring gasket. First, the cathode was reduced by H_2 to form a porous Ni-BZCYYb cermet cathode. For steam electrolysis, steamed air was fed to the anode and humidified 10% hydrogen in Ar gas was fed to the cathode. Steamed air was prepared using a temperature-controlled water bubbler and the water partial pressure (p_{H2O}) was set from 0.03 to 0.4 atm according to the detailed measurement conditions. A Solartron 1260A frequency response analyzer implemented with a Solartron 1287 potentiostat in the frequency range of 10^6–10^{-1} Hz with an alternating current (AC) amplitude of 30 mV under open circuit voltage (OCV) conditions and different direct current (DC) potentials. Current-voltage (*I-V*) curves were recorded using the same apparatus as displayed in Figure 2-4.

2.4.3 Hydrogen production and Faradaic efficiency

After the reduction of NiO in the cells, the temperature was maintained at 500 or

600 °C. Subsequently, the steam partial pressure was fixed at 0.2 atm to evaluate the hydrogen production and faradaic efficiency. Under galvanostatic electrolysis conditions, the variation of the hydrogen concentration in the cathode out-gas was monitored using gas chromatography (490 Micro GC, Agilent Technologies) as shown in Figure 2-4. The efficiency under steam electrolysis was calculated as the ratio of the measured hydrogen evolution rate and the theoretical data from the applied current as shown in Equation (2-1).

$$\eta = \frac{n_{H_2,\,measured}}{n_{H_2,\,theoretical}} = \frac{n_{H_2,\,measured}}{I \times (n \times F)^{-1}} \times 100\% \qquad (2\text{-}1)$$

Where, $n_{H2,\,measured}$ is the measured hydrogen evolution rate, I is the applied current, n (2) is the electron transport number of steam electrolysis, and F is Faraday's constant (96485 C mol^{-1}).

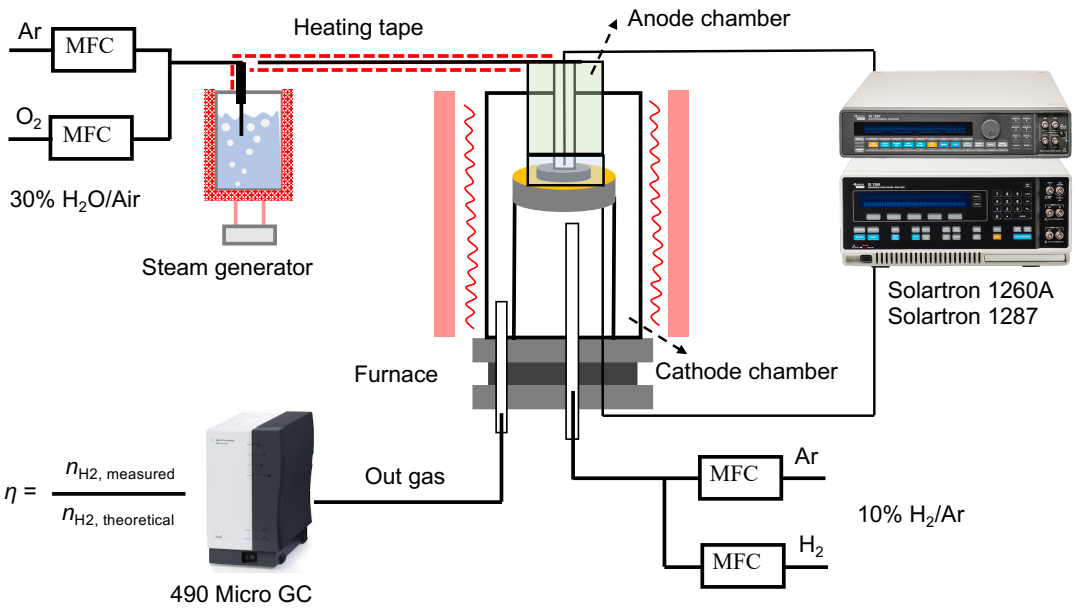

Figure 2-4 Measurement setup of steam electrolysis for P-SOECs.

2.5 Reference

1. Z. Du, P. Yang, L. Wang, Y. Lu, J. B. Goodenough, J. Zhang and D. Zhang, *J. Power Sources*, 2014, **265**, 91–96.

Chapter 3 Effect of $La_{0.5}Sr_{0.5}CoO_{3-\delta}$ anode functional layer for protonic solid oxide electrolysis cells based on high Zr-content electrolyte

3.1 Objective of chapter 3

As mentioned in chapter 1.4, protonic solid oxide electrolysis cells (P-SOECs) based on proton-conducting perovskites, that is, $Ba(Ce,Zr,M)O_{3-\delta}$ (M = Y, Yb, etc.) are attractive alternatives to high temperature solid oxide electrolysis cells (SOECs) because the relatively low activation energy of proton conduction (0.4–0.6 eV) enables operation in the intermediate temperature region (400−700 °C).[1–4] $Ba(Ce, Zr, M)O_{3-\delta}$ tends to be more thermodynamically stable under high H_2O partial pressure (p_{H2O}) with increasing Zr content,[5–7] and thus, Zr-rich side materials are desirable as a practical electrolyte for P-SOECs. Nevertheless, the electrolysis performance of P-SOECs with Zr-rich side electrolyte is considerably inferior to that of P-SOECs with a Ce-rich side electrolyte. For instance, Duan *et al*. conducted a study on $BaZr_{0.1}Ce_{0.7}Y_{0.1}Yb_{0.1}O_{3-\delta}$ (BZCYYb1711) can yield an electric current density of ~1.00 A cm^{-2} at a thermal neutral voltage of 1.30 V at 600 °C,[4] which is considerably higher than the performance of SOECs with YSZ electrolyte.[8,9] However, the cell with $Ba(Zr_{0.5}Ce_{0.4})_{8/9}Y_{0.2}O_{2.9}$ can produce only 0.50 A cm^{-2} at 1.45 V at 600 °C.[10] One major reason for the deteriorated performance in Zr-rich side electrolytes is the relatively large ohmic resistance of the electrolyte. This is because $Ba(Ce,Zr,M)O_{3-\delta}$ tends to show larger grain boundary resistances with increasing Zr content due to the highly refractory nature of $BaZrO_3$ moieties.

In this chapter, we demonstrated that the electrolysis performance of a cell with high Zr-content electrolyte, $BaZr_{0.6}Ce_{0.2}Y_{0.1}Yb_{0.1}O_{3-\delta}$ (BZCYYb6211) can be significantly improved by using a $La_{0.5}Sr_{0.5}CoO_{3-\delta}$ (LSC) thin film as an anode functional layer (AFL), which was fabricated between the electrolyte and anode by radio frequency (RF) sputtering. The implementation of LSC AFL decreased the ohmic resistances due to proton bulk conduction even though LSC was not highly proton conductive. It also

decreased the resistances related to electrochemical proton incorporation at anode-electrolyte–gas triple phase boundaries by a factor of 50% at 600 °C. BZCYYb6211 based P-SOECs yielded 1.22 A cm^{-2} at 600 °C in 1.3 V with the aid of LSC AFL, which is close to the electrolysis current of a similar type of cell using Ce-rich electrolyte $BaZr_{0.1}Ce_{0.7}Y_{0.1}Yb_{0.1}O_{3-\delta}$ (BZCYYb1711). These results reveal that the introduction of an AFL is an effective method to obtain P-SOECs with excellent performance.

3.2 Experimental section

3.2.1 Synthesis of $La_{0.8}Sr_{0.2}Co_{0.7}Ni_{0.3}O_{3-\delta}$ anode powders

We chose $La_{0.8}Sr_{0.2}Co_{0.7}Ni_{0.3}O_{3-\delta}$ (LSCN) as the anode of P-SOECs in this chapter because the previous study of our laboratory has demonstrated that LSCN is efficient for revisable protonic ceramic cells (R-PCCs) with excellent activity and durability.[11] The powders were synthesized via a citrate precursor route, in which the required amounts of nitrate precursors of $La(NO_3)_3 \cdot 6H_2O$ (99.99%, Kanto Chemical Co.), $Sr(NO_3)_2$ (98%, Kanto Chemical Co.), $Co(NO_3)_2 \cdot 6H_2O$ (98%, Kanto Chemical Co.), and $Ni(NO_3)_2 \cdot 6H_2O$ (98%, Kanto Chemical Co.) were dissolved in Milli-Q H_2O. The chelating agent citric acid (CA; $C_6H_8O_7 \cdot H_2O$, 99.5%, Kanto Chemical Co.) was added at a molar ratio of CA:LSCN = 2:1. Gelatinous products were obtained by heating the citrate solution at 60 °C for 3 h with vigorous stirring to evaporate H_2O and promote polymerization. The gel was calcined at 500 °C for 1 h in air and then annealed at 800 °C for 15 h in O_2 to obtain single-phase LSCN powders. In a separate experiment $La_{0.5}Sr_{0.5}CoO_{3-\delta}$ (LSC) was also applied to the anode, which was prepared by the similar method as LSCN.

3.2.2 Synthesis of $BaZr_xCe_{0.8-x}Y_{0.1}Yb_{0.1}O_{3-\delta}$

$BaZr_xCe_{0.8-x}Y_{0.1}Yb_{0.1}O_{3-\delta}$ (x = 0.1, 0.6; BZCYYb1711, BZCYYb6211, respectively) electrolyte powders were prepared with stoichiometric quantities of $BaCO_3$ (High Purity Chemicals, 99.95%), ZrO_2 (High Purity Chemicals, 98%), CeO_2 (High Purity Chemicals, 99.99%), Y_2O_3 (High Purity Chemicals, 99.99%), and Yb_2O_3 (High Purity Chemicals, 99.9%). The mixture was first ball-milled for 10 h using ethanol as the

milling medium, and then the ethanol was removed by heating the mixture at 80 °C. The powders were calcined at 1300 °C for 10 h after slightly grinding by hand. To ensure the formation of phases, milling and calcination were repeated.

3.2.3 Fabrication of protonic solid oxide electrolysis cells

Cathode-supported P-SOECs were fabricated as shown in Figure 3-1. The porous cathode was prepared by ball-milling NiO (High Purity Chemicals, 99.97%), electrolyte powders (either BZCYYb1711 or BZCYYb6211), and starch with a weight ratio of 60:40:7, respectively, for 10 h in ethanol. After drying, the mixture powders were uniaxially pressed into pellets (~12 mm diameter, ~1.8 mm thickness) under 20 MPa and subsequently isostatically pressed under a hydrostatic pressure of 100 MPa. The electrolyte layer was spin-coated on both surfaces of the porous cathode pellets with a slurry, which was prepared by dispersing electrolyte powders with 1 wt.% NiO into a solution containing a dispersant (20 wt.% polyethyleneimine (M_w 28 000) dissolved in α-terpineol) and a binder (5 wt.% surfactant dissolved in α-terpineol). Subsequently, the pellet was first exposed to 1450 °C for 10 min and then at 1400 °C for 8 h in an air atmosphere to form a half-cell. The back side of the sintered pellet was polished with SiC paper. LSC thin film was deposited on the electrolyte layer by radio frequency (RF) sputtering at a base pressure of less than 1×10^{-4} Pa, performed in an ultrahigh-vacuum chamber system (ULVAC ACS-3000). RF sputtering was performed at a sputtering power of 50 W under a flow of 4%–O_2/Ar gas at 50 sccm, and the substrate temperature was maintained at 500 °C. Finally, a LSCN slurry prepared by dispersing the powders into a mixture of dispersant and binder was screen-printed on the electrolyte or LSC AFL as porous anode.

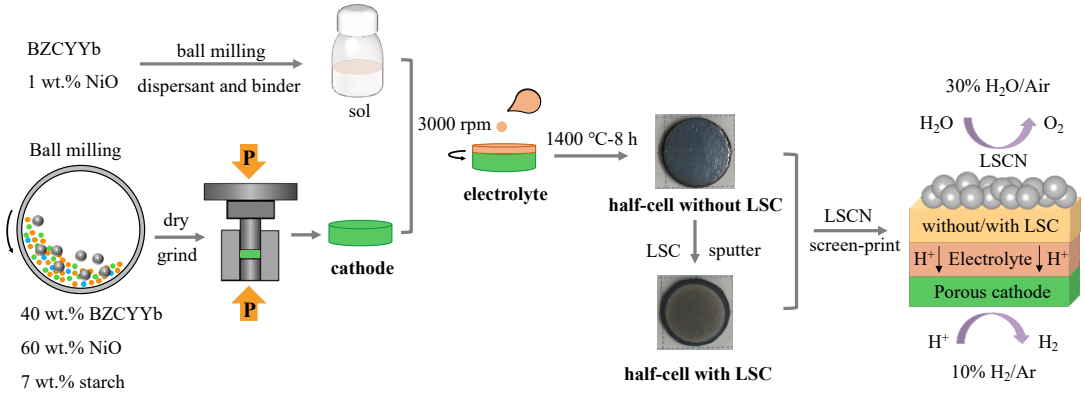

Figure 3-1 Schematic illustration of the fabrication for protonic solid oxide electrolysis cells.

3.2.4 Characterization

The phase was identified by X-ray powder diffraction (XRD, Rigaku, Ultima IV) with Cu Kα radiation at a scan rate of 5° min^{-1} in the 2θ range from 20° to 80°. For the XRD measurements, the sintered body specimens were pulverized in a mortar. The structure of the LSC thin film deposited on a silicon plate was characterized using a grazing incidence X-ray diffractometer (GIXRD, Rigaku, RINT-2000) at a scan speed of 0.5° min^{-1} and a grazing incidence angle of 2°. Field emission scanning electron microscopy (FESEM, SIGMA500, ZEISS) was employed to examine the microstructures of the cells. High-resolution transmission electron microscopy (HR-TEM) was performed using a field-emission TEM (Jeol JEM-2010) equipped with an energy dispersive X-ray spectrometer (EDX).

For steam electrolysis, P-SOECs were mounted in a laboratory-constructed test station with the seal of a molten glass ring gasket. The cathode was reduced at 700 °C for 3 h by supplying 60%–H_2/Ar gas to the cathode side and 3%–H_2O/Ar to the anode side to form a porous Ni-BZCYYb cermet cathode. For steam electrolysis, steamed air was fed to the anode at a total flow of 62 sccm, and humidified hydrogen gas with a ratio of H_2O/H_2/Ar = 2/10/90 was fed to the cathode at a total flow rate of 20.4 sccm. Steamed air was prepared using a temperature-controlled water bubbler with an inlet of 20%–O_2/Ar mixed gas. The water partial pressure (p_{H2O}) of steamed air was set to 0.3

atm. Humidified hydrogen gas was prepared by bubbling 10%–H_2/Ar = 10/90 in pure water maintained at 25 °C. The impedance spectra of P-SOECs were measured using a Solartron 1260A frequency response analyzer implemented with a Solartron 1287 potentiostat in the frequency range of 10^6–10^{-1} Hz with an alternating current (AC) amplitude of 30 mV under open circuit voltage (OCV) conditions and different direct current (DC) potentials. Current-voltage (*I-V*) curves were recorded using the same apparatus.

The amount of hydrogen evolution through steam electrolysis was determined by analyzing the exhaust gas from the cathode side using a gas chromatograph (490 Micro GC, Agilent Technologies). The Faraday efficiency, η, was calculated according to Equation (2-1) as depicted in Chapter 2.4.3.

3.3 Results and discussion

3.3.1 Material characterization

In general, water tolerance of proton conducting perovskite is increased with Zr contents of B site cations.[5–7,12,13] In this regard, $BaZr_{0.6}Ce_{0.1}Y_{0.1}Yb_{0.1}O_{3-\delta}$ (BZCYYb6211) is attractive electrolyte for steam electrolysis conducted under high water partial pressure (p_{H2O}) condition. $BaZr_{0.1}Ce_{0.7}Y_{0.1}Yb_{0.1}O_{3-\delta}$ (BZCYYb1711) has been recognized as a state-of-the-art electrolyte of proton conducting perovskites with satisfactory high proton conductivity, as mentioned in chapter 3.1.[4,14–16] Here the effect of the AFL was examined on both BZCYYb1711 and BZCYYb6211 electrolytes. Both electrolyte powders were successfully prepared as single-phase monoclinic and cubic perovskites, respectively. Figure 3-2 shows the powder XRD patterns of a sintering cake for dense BZCYYb films on BZCYYb-NiO composite supports. All the diffraction peaks were consistent with those of the BZCYYb perovskites and NiO. The peaks of BZCYYb6211 emerged at higher angles than the corresponding peaks of BZCYYb1711, indicating that the lattice constants of the former were smaller than those of the latter due to the substitution of Ce^{4+} (0.87 Å) by Zr^{4+} (0.72 Å). The surface SEM images of BZCYYb1711 and BZCYYb6211 electrolyte films are shown in Figure

3-2b and c, respectively. Due to the easy sinterability of the Ce-rich phase compared to that of the Zr-rich phase,[17,18] the average grain size of BZCYYb1711 (*ca.* 20–25 μm) was considerably larger than that of BZCYYb6211 (*ca.* 3–4 μm).

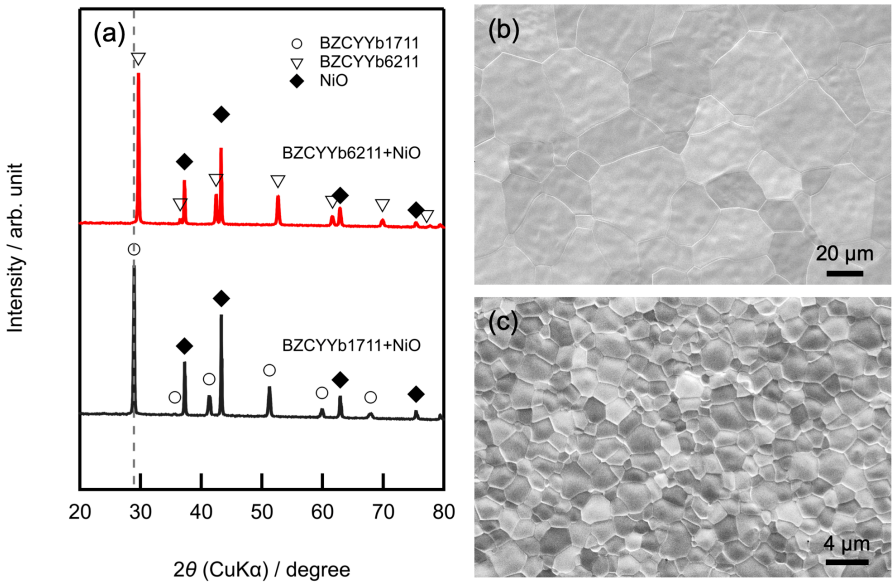

Figure 3-2 (a) Powder XRD patterns of a sintering cake comprising a dense BZCYYb film and BZCYYb-NiO composite bulk. (b) and (c) show surface SEM images of BZCYYb1711 and BZCYYb6211 electrolyte films, respectively.

The single phase of LSCN anode layer was a porous agglomerate of oxide particles with a diameter of several tens of nanometers (Figure 3-3a and b). Figure 3-3c and d shows the cross-sectional SEM images of BZCYYb1711 and BZCYYb6211 P-SOECs comprising a porous cathode support, electrolyte film, AFL, and LSCN anode. Ni-BZCYYb cathode supports retain interpenetrating networks of macro-and micropores, which must be formed via the combustion of starch and the reduction of NiO, thus providing a sufficient gas diffusion pathway. A highly dense electrolyte film of BZCYYb1711 and BZCYYb6211 was uniformly formed over a wide area of corresponding porous Ni-BZCYYb cathode with a thickness of ~14 μm.

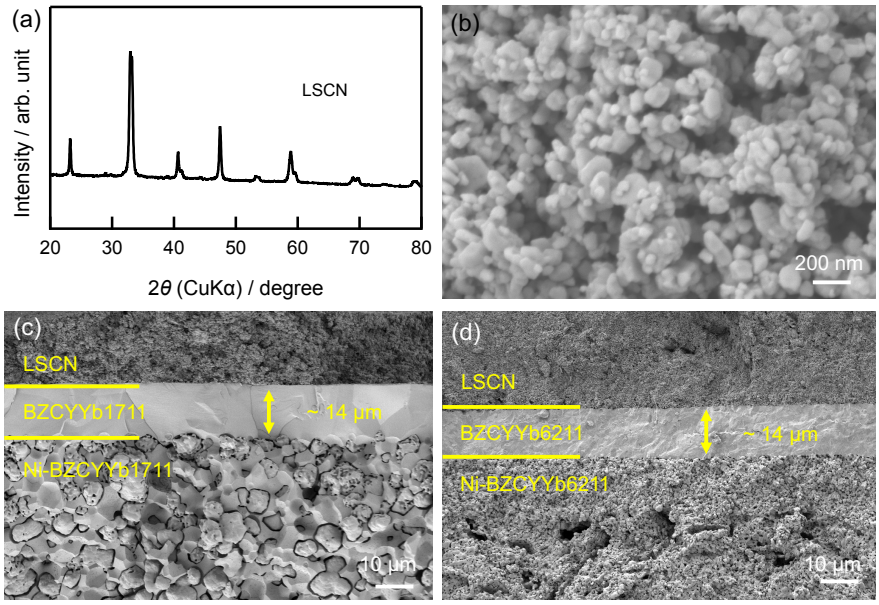

Figure 3-3 (a) XRD patterns and (b) SEM image of LSCN anode. Cross-sectional SEM images of cathode-supported P-SOECs of BZCYYb1711 (c) and BZCYYb6211 (d), respectively.

The SEM and TEM images of the interface between LSC AFL and BZCYYb6211 electrolyte revealed that the LSC AFL with a thickness of ~90 nm was uniformly formed over the surface of the electrolyte (Figure 3-4a and b). The GIXRD patterns of the LSC thin film deposited on a silicon wafer by RF sputtering were identical to those of rhombohedral $La_{0.5}Sr_{0.5}CoO_{2.91}$ ($R\bar{3}c$, PDF-48-0122; Figure 3-5). Further characterization was conducted for the LSC AFL of the cell before printing the porous anode. Figure 3-4c shows the scanning TEM (STEM)-EDX mapping analysis, confirming that La, Sr, and Co atoms were uniformly distributed throughout the film while preserving the same molar ratio of La:Sr:Co = 1:1:2 as the parent phase. HRTEM results exhibited a clear lattice fringe with an interplanar lattice distance of 0.271 nm (Figure 3-4d), which corresponds to the (104) crystal plane, indicating that a well-defined LSC thin film was uniformly formed over the electrolyte surface.

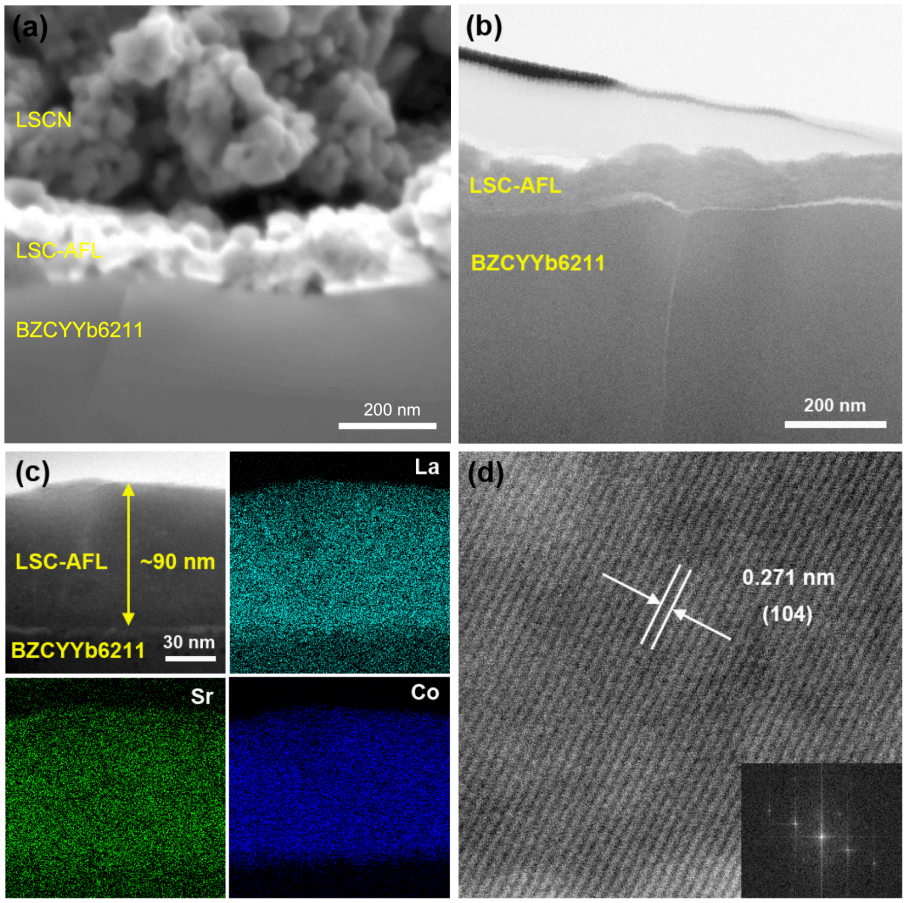

Figure 3-4 Cross-sectional SEM (a) and TEM (b) images of BZCYYb6211 cell. (c) STEM-EDX mapping and (d) HRTEM image of LSC thin film deposited on BZCYYb6211 electrolyte. The inset of (d) shows the fast Fourier transform patterns of the lattice fringe image.

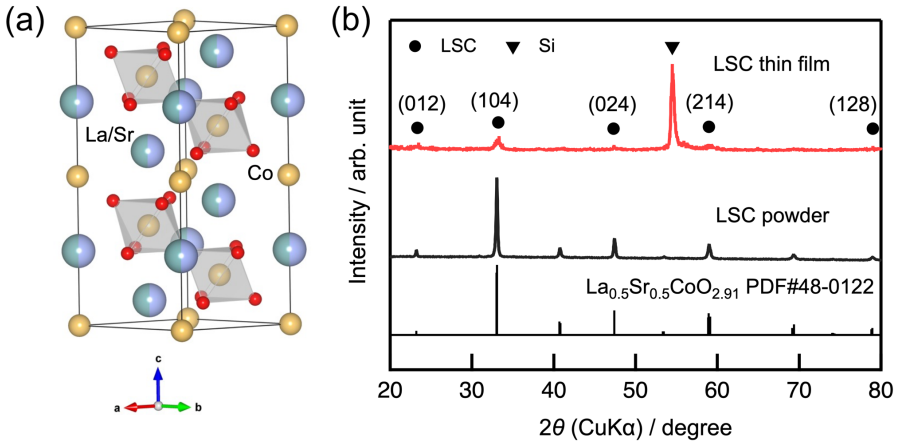

Figure 3-5 (a) Crystal structure of $La_{0.5}Sr_{0.5}CoO_3$. (b) XRD patterns of prepared LSC powder and LSC thin film deposited on a silicon wafer.

3.3.2 Performances of P-SOECs without and with LSC AFL

The electrochemical performance of P-SOECs based on BZCYYb1711 and BZCYYb6211 electrolytes was evaluated in the temperature range of 700–500 °C by supplying 30%–H_2O/Air and humidified 10%–H_2/Ar gases to the anode and cathode, respectively. Figure 3-6 shows the current-voltage relationships of the P-SOECs with and without LSC AFL (~90 nm). For the cell without LSC AFL layer, the OCVs of BZCYYb1711 and BZCYYb6211 cells were 0.93 and 0.92 V, respectively, at 600 °C (Figure 3-6a and c, respectively), which were slightly lower than the theoretical value (E_{Nernst}) of 0.96 V as calculated by conventional Nernst equation. The steam electrolysis currents of the BZCYYb1711 cell were equal to 2.10, 1.11, 0.57, 0.30, and 0.15 A cm^{-2} at 700, 650, 600, 550, and 500 °C, respectively, at the thermal neutral point (approximately 1.3 V in the temperature range; Figure 3-6a). BZCYYb6211 exhibited inferior performance to BZCYYb1711 at relatively high temperatures, with electrolysis currents of 1.50 and 0.96 A cm^{-2}, at 700 and 650 °C, respectively, in 1.3 V. The electrolysis currents of the former were similar to those of the latter at temperatures below 600 °C, yielding 0.55, 0.30, and 0.14 A cm^{-2} at 600, 550, and 500 °C, respectively (Figure 3-6c). The electrolysis currents of P-SOECs significantly increased with the introduction of the LSC AFL between the electrolyte film and anode at all temperatures analyzed (Figure 3-6b and d). With the LSC AFL, the currents of BZCYYb1711 and BZCYYb6211 base cells provided OCVs similar to those of cells without LSC AFL, were 3.07 and 3.07 A cm^{-2}, respectively, at 700 °C by applying 1.3 V cell voltage. These values were 46.19% and 104.46% higher than the corresponding values of the cells without LSC AFL, respectively (Figure 3-6e and f, respectively). Similarly, the currents at 1.3 V were 1.13 and 1.22 A cm^{-2} for BZCYYb1711 and BZCYYb6211 base cells, at 600 °C, which were 97.55% and 120.61% higher than the values of the corresponding cells without LSC AFL, respectively. Even at the relatively low temperature of 500 °C, the BZCYYb1711 and BZCYYb6211 base cells with LSC AFL exhibited 0.31 A cm^{-2} and 0.30 A cm^{-2} at 1.3 V, and 0.65 and 0.76 A cm^{-2} at 1.5 V, respectively. The values at 1.3 V were 110.81% and 117.73% higher than those of cells without LSC AFL,

respectively (Figure. 3-6e and f).

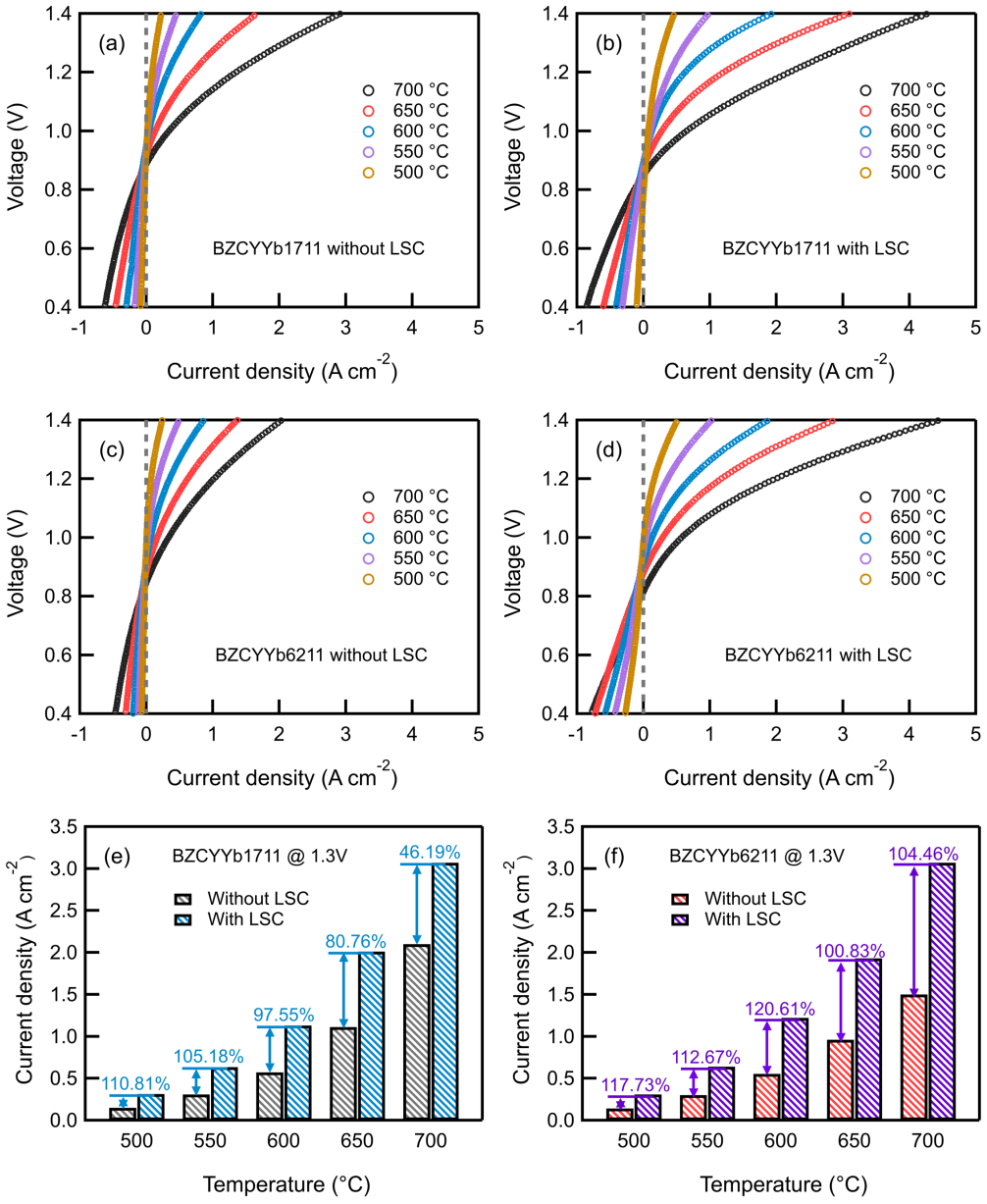

Figure 3-6 Electrochemical performance of (a) and (b)BZCYYb1711 base cells and (d) BZCYYb6211 base cells. (a) and (c) are the cells without LSC AFL, and (c) and (d) are cells with LSC AFL. Electrolysis current density at 1.3 V for (e) BZCYYb1711 and (f) BZCYYb6211 base cells.

Table 3-1 Performances of steam electrolysis based on P-SOECs at 600 ℃ under 1.3 V in recent years.

Configuration of electrolysis cell: anode/electrolyte (thickness)/cathode	Inlet gas composition		OCV/E_{Nernst} (V)	I (A cm^{-2})	Ref.
	Anode	Cathode			
LSCN8273/BZCYYb1711 (14 μm)/Ni-BZCYYb1711	Air (30% H_2O)	10% H_2/Ar (3% H_2O)	0.93/0.96	0.57	This
LSCN8273/BZCYYb6211 (14 μm)/Ni-BZCYYb6211	Air (30% H_2O)	10% H_2/Ar (3% H_2O)	0.92/0.96	0.55	This
LSCN8273/LSC/BZCYYb1711 (14 μm)/Ni-BZCYYb1711	Air (30% H_2O)	10% H_2/Ar (3% H_2O)	0.89/0.96	1.13	This
LSCN8273/LSC/BZCYYb6211 (14 μm)/Ni-BZCYYb6211	Air (30% H_2O)	10% H_2/Ar (3% H_2O)	0.91/0.96	1.22	This
SFM/BZY82 (16 μm)/Ni-BZY82	Air (3% H_2O)	10% H_2/N_2	0.86/1.05	0.21	19
SEFC/BZCY172 (15 μm)/Ni-BZCY172	Air (10% H_2O)	97% H_2 (3% H_2O)	0.99/1.05	~0.40	20
SLF/BZCY352 (20 μm)/Ni-BZCY352	Air (20% H_2O)	97% H_2 (3% H_2O)	0.96/1.04	0.46	21
NBSCF-BZCYYb1711/BZCYYb1711 (20 μm)/Ni-BZCYYb1711	Air (10% H_2O)	97% H_2 (3% H_2O)	1.03/1.05	0.75	15
PNO-BZCY262/ BZCY262 (20 μm)/ Ni-BZCY262	Air (40% H_2O)	100% H_2	0.98/1.02	0.60	22
LSN/BZCY172 (15 μm)/Ni-BZCY172	Air (20% H_2O)	97% H_2 (3% H_2O)	1.02/1.04	0.42	23
PBSCF(3D)/BZCYYb (20 μm)/Ni-BZCYYb	O_2 (12% H_2O)	5% H_2/Ar	0.99/1.00	0.85	16
PBCC95/BZCYYb4411 (20 μm)/Ni-BZCYYb4411	O_2 (20% H_2O	100% H_2	1.06/1.16	0.72	24
PNC/BZCYYb4411 (15 μm)/Ni-BZCYYb4411	Air (10% H_2O)	10% H_2/Ar	1.01/1.00	1.18	25
PNO/LCO|BZCYYb1711 (bilayer 20 μm)/Ni-BZCYYb1711	Air (60% H_2O)	100% H_2	0.95/1.00	0.33	26
LSN/BZCYYbCu (13 μm)/Ni-BZCYYbCu	Air (20% H_2O)	97% H_2 (3% H_2O)	0.99/1.06	0.59	27
PBSCF/BZCYYb4411 (15 μm)/Ni-BZCYYb4411	Air (3% H_2O)	5% H_2/Ar	0.92/1.03	1.31	28
BCFZY/BZCYYb1711 (12 μm)/Ni-BZCYYb1711	Air (10% H_2O)	100%Ar	–	1.00	4
PNC/BZCYYbGd (25 μm)/Ni-BZCYYbGd	O_2 (20% H_2O)	100% H_2	1.02/1.09	0.56	29
BZCY36-BCFZY/BZCYSm (25 μm)/Ni-BZCYSm	Air (12% H_2O)	97% H_2 (3% H_2O)	1.05/1.08	0.37	30
LSN- BZCYYbCu/BZCYYbCu (13 μm)/Ni-BZCYYbCu	Air (20% H_2O)	97% H_2 (3% H_2O)	0.98/1.08	1.03	31
SFM-BZY82/BZY82 (18 μm)/Ni-BZCY172	Air (3% H_2O)	20% H_2/N_2	0.92/1.08	0.38	32
PBSCF/BHCYYb3511 (10 μm)/Ni-BHCYYb3511	Air (3% H_2O)	97% H_2 (3% H_2O)	1.04/1.13	1.45	33

Abbreviations: $Sr_2Fe_{1.5}Mo_{0.5}O_{6-\delta}$ (SFM); $BaZr_{0.8}Y_{0.2}O_{3-\delta}$ (BZY82); $SrEu_2Fe_{1.8}Co_{0.2}O_{7-\delta}$ (SEFC); $BaZr_{0.1}Ce_{0.7}Y_{0.2}O_{3-\delta}$ (BZCY172); $Sr_{2.8}La_{0.2}Fe_2O_{7-\delta}$ (SLF); $BaZr_{0.3}Ce_{0.5}Y_{0.2}O_{3-\delta}$ (BZCY352); $NdBa_{0.5}Sr_{0.5}Co_{1.5}Fe_{0.5}O_{5+\delta}$ (NBSCF); $Pr_2NiO_{4+\delta}$ (PNO); $BaZr_{0.2}Ce_{0.6}Y_{0.2}O_{3-\delta}$ (BZCY262); $La_{1.2}Sr_{0.8}NiO_4$ (LSN); $PrBa_{0.5}Sr_{0.5}Co_{2-x}Fe_xO_{5+\delta}$ (PBSCF), $BaZr_{0.1}Ce_{0.7}Y_{0.2-x}Yb_xO_{3-\delta}$ (BZCYYb); $(PrBa_{0.8}Ca_{0.2})_{0.95}Co_2O_{6-\delta}$ (PBCC95); $BaZr_{0.4}Ce_{0.4}Y_{0.1}Yb_{0.1}O_{3-\delta}$ (BZCYYb4411); $PrNi_{0.5}Co_{0.5}O_{3-\delta}$ (PNC); $BaZr_{0.1}Ce_{0.68}Y_{0.1}Yb_{0.1}Cu_{0.02}O_{3-\delta}$ (BZCYYbCu); $BaCo_{0.4}Fe_{0.4}Zr_{0.1}Y_{0.1}O_{3-\delta}$ (BCFZY); $BaZr_{0.2}Ce_{0.5}Y_{0.1}Yb_{0.1}Gd_{0.1}O_{3-\delta}$ (BZCYYbGd); $BaZr_{0.1}Ce_{0.7}Y_{0.1}Sm_{0.1}O_{3-\delta}$ (BZCYSm).

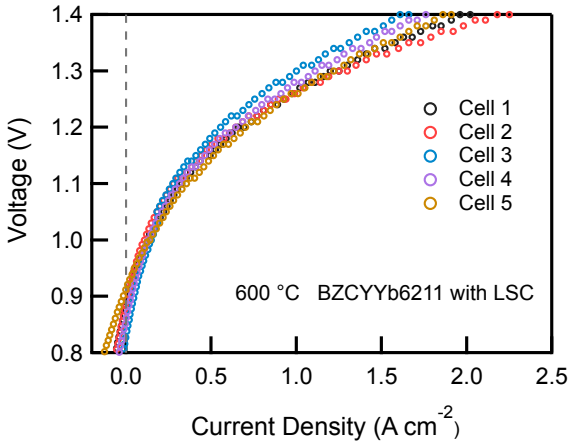

Figure 3-7. *I-V* curves for five samples of BZCYYb6211 base electrolysis cells with LSC AFL at 600 °C.

The electrolysis currents of the cells with LSC AFL were considerably higher than those of most previously reported P-SOECs, as summarized in Table 3-1. Figure 3-7 shows *I-V* curves for several samples of BZCYYb6211 cells with LSC AFL at 600 °C, indicating that the curves are very similar to each other, which confirms the excellent performance of the current cells.

Figure 3-8 shows the current-voltage-power (*I-V-P*) curves of BZCYYb1711 and BZCYYb6211 base cells with and without LSC AFL in the fuel cell mode. The peak power densities (PPDs) of BZCYYb1711 and BZCYYb6211 cells with LSC AFL were considerably higher than those of cells without LSC AFL. For instance, the PPDs of the BZCYYb6211 cell with LSC AFL were 316, 297, 233, 171, and 110 mW cm^{-2} at 700, 650, 600, 550, and 500 °C, respectively, which were considerably higher than the values of the cell without LSC AFL at each temperature. These results indicate that AFL promotes both oxygen evolution and reduction reactions in protonic ceramic cells.

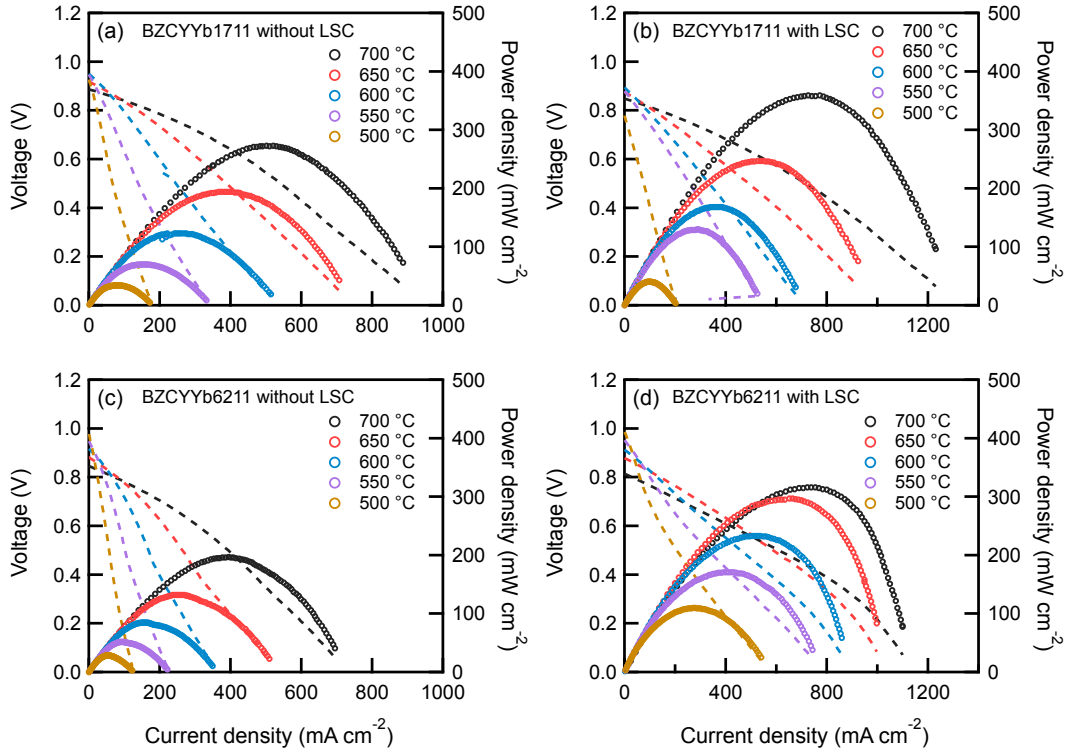

Figure 3-8 Current-voltage-power (*I-V-P*) curves of fuel cell mode for the BZCYYb1711 base cells ((a) and (b)) and the BZCYYb6211 base ones ((c) and (d)) performed with 30%–H_2O/Air and humidified 10%–H_2/Ar gases to the air and fuel electrodes, respectively. (a) and (c) are the cells without LSC AFL, and (c) and (d) ones with LSC AFL. The gas condition of the fuel cell mode is same as that of the steam electrolysis cell, i.e., 30%–H_2O/Air and humidified 10%–H_2/Ar gases were fed to the air and fuel electrodes, respectively.

Figure 3-9 shows the voltage responses and H_2 evolution rates of BZCYYb1711 and BZCYYb6211 cells without and with LSC AFL during galvanostatic electrolysis at 500 °C. Here, the constant current was set to 0.15 A cm^{-2} for the cells without AFL (Figure 3-9a) and 0.24 A cm^{-2} for the cells with AFL (Figure 3-9b and c) to investigate the behavior near the thermal neutral point around 1.3 V. The hydrogen concentrations in the cathode exhaust gases were monitored by gas chromatography, which allowed the determination of the H_2 evolution rate. The concentrations were in equilibrium for approximately 1 h after the beginning of electrolysis in every cell, and thus the average rates after 1 h were used to calculate the Faraday efficiency (see chapter 2.4.3). The

efficiency of BZCYYb1711 without and with LSC was approximately 76% and 71%, respectively. The efficiency of less than 100% is due to the hole conductivity of $Ba(Zr,Ce,Y)O_{3-\delta}$ electrolytes,[34–36] which is attributed to the relatively low steam pressure (p_{H2O}) at the anode and hydrogen pressure (p_{H2}) at the cathode because the transport number of holes in the $BaZr_{0.7}Ce_{0.2}Y_{0.1}O_{2.95}$ electrolyte is close to 0 with increasing pressure of p_{H2O} and p_{H2} to 25 and 50 atm, respectively.[34] Both BZCYYb6211 and BZCYYb1711 cells with LSC achieved an efficiency of 70%. These values of Faraday efficiency were consistent with the corresponding values ranging from 40% to 86% for the P-SOECs at 1.3 V under low p_{H2O} and p_{H2} conditions.[25,28] The slight degradation in Faraday efficiency indicates the LSC AFL promotes not only proton but also hole transport in electrolyte, which is probably due to the modification of hydrogen and/or oxygen potential at the interface. Nevertheless, the hydrogen production rate clearly increases from ~40 to ~60 μmol min^{-1} cm^{-2} at 1.3 V by LSC AFL as shown in Figure 3-9.

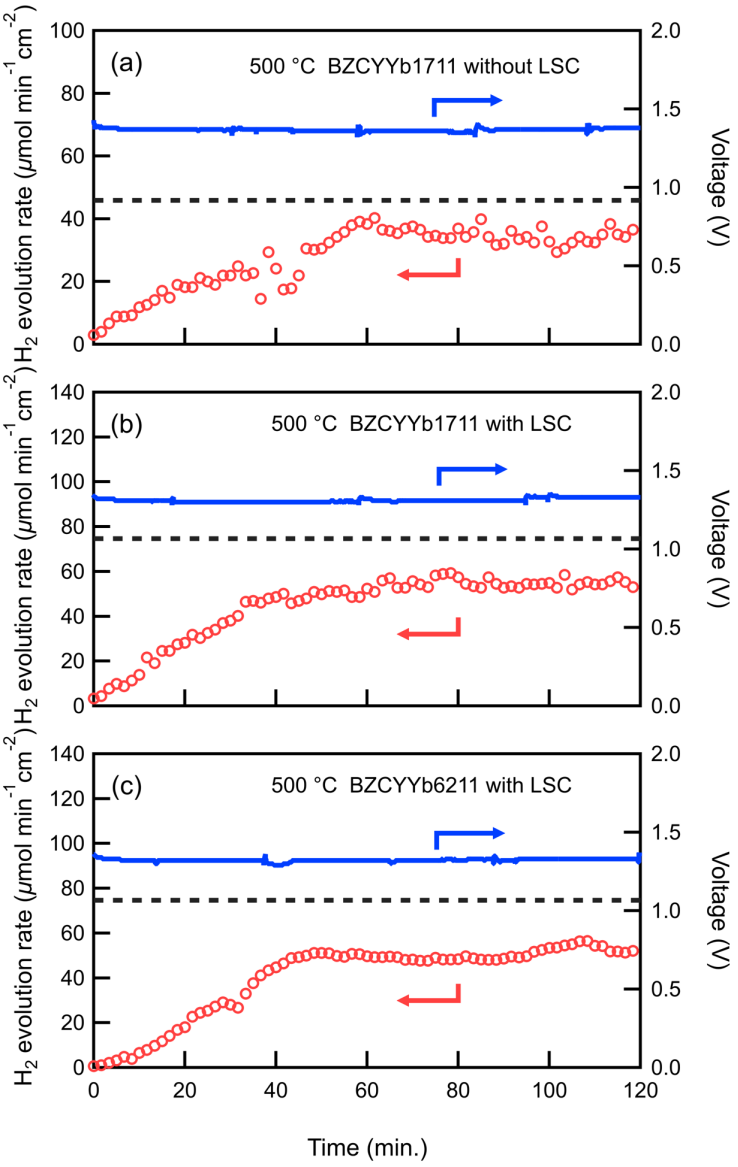

Figure 3-9 Responses of cell voltages and transients of H_2 gas evolution rates during galvanostatic electrolysis at 500 °C. (a) BZCYYb1711 cell without LSC AFL, (b) BZCYYb1711 cell with LSC AFL, and (c) BZCYYb6211 cell with LSC AFL. The constant currents were set to 0.15 A cm^{-2} for (a) and 0.24 A cm^{-2} for (b) and (c). Blue lines show the cell voltage and red symbols show the H_2 evolution rate determined by gas chromatography. Black dashed lines indicate the rate calculated with 100% Faradaic efficiency.

3.3.3 Impacts on ohmic and polarization resistances by LSC AFL

Electrochemical impedance spectra (EIS) were recorded under various DC conditions and temperatures, as shown in Figure 3-10, 3-11 and 3-12, to deconvolute the ohmic and polarization resistances of the P-SOECs. Usually, the impedance spectra of solid electrochemical cells include the high-frequency *x*-intercept region, corresponding to ohmic loss, that is, the bulk resistances (R_o) and the following arcs are associated with the interfacial polarization resistances (R_p) on the anode side.[8,20,36,37] The P-SOECs yield two distinct arcs in the EIS spectra: an S_{HF} arc (Figure 3-11a and c) in the high-frequency region of 10^5–10^3 Hz, and an S_{LF} (Figure 3-11a and c) arc in the low-frequency region of 10^3–10^{-1} Hz. Hence, the EIS spectra of P-SOECs at 600 and 500 °C were fitted with the equivalent circuit L_s-R_o-(R_{HF}-CPE$_{HF}$)-(R_{LF}-CPE$_{LF}$) depicted in the inset of Figure 3-11b, where *L*, *R*, and CPE are the inductance, resistance, and constant phase element, that is, pseudo-capacitance, respectively. L_s comes from the electrical metal lead, and R_o is mainly attributed to proton conduction in the electrolyte. Parallel components of (R_{HF}-CPE$_{HF}$) and (R_{LF}-CPE$_{LF}$) were used to represent S_{HF} and S_{LF}, respectively. Therefore, R_{HF} and R_{LF} provide the polarization resistance related to S_{HF} and S_{LF}, respectively. In all cells, the observed EIS spectra were well fitted with the equivalent circuit model, as shown in Figure 3-11a–d, and the results are summarized in Table 3-2.

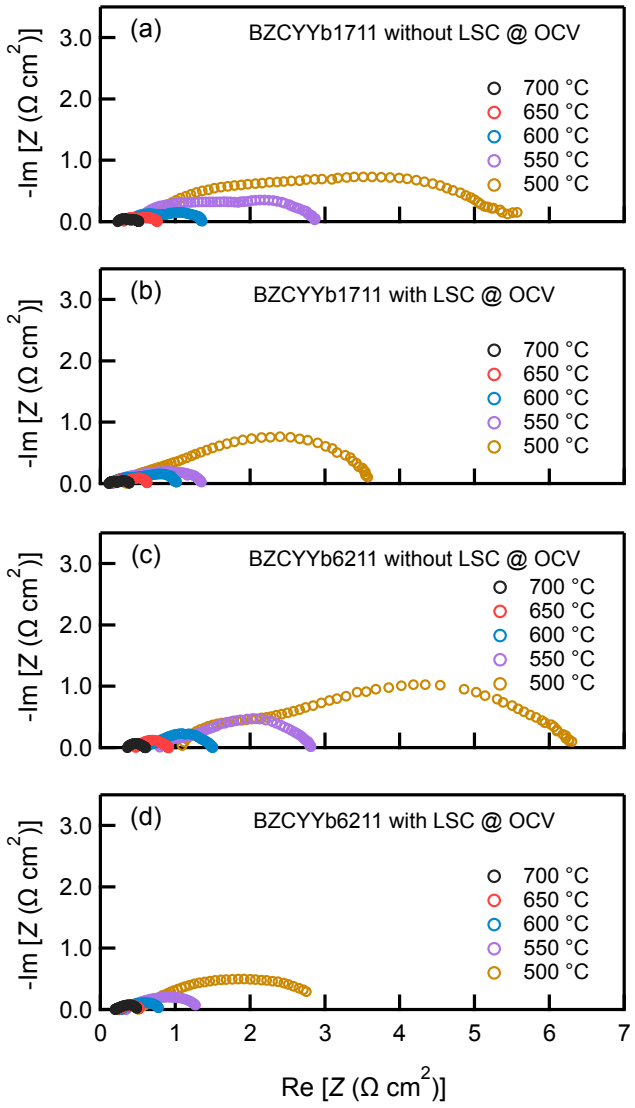

Figure 3-10 EIS for BZCYYb1711 ((a) and (b)) and BZCYYb6211 ((c) and (d)) cells without and with LSC AFL at various temperatures under OCV.

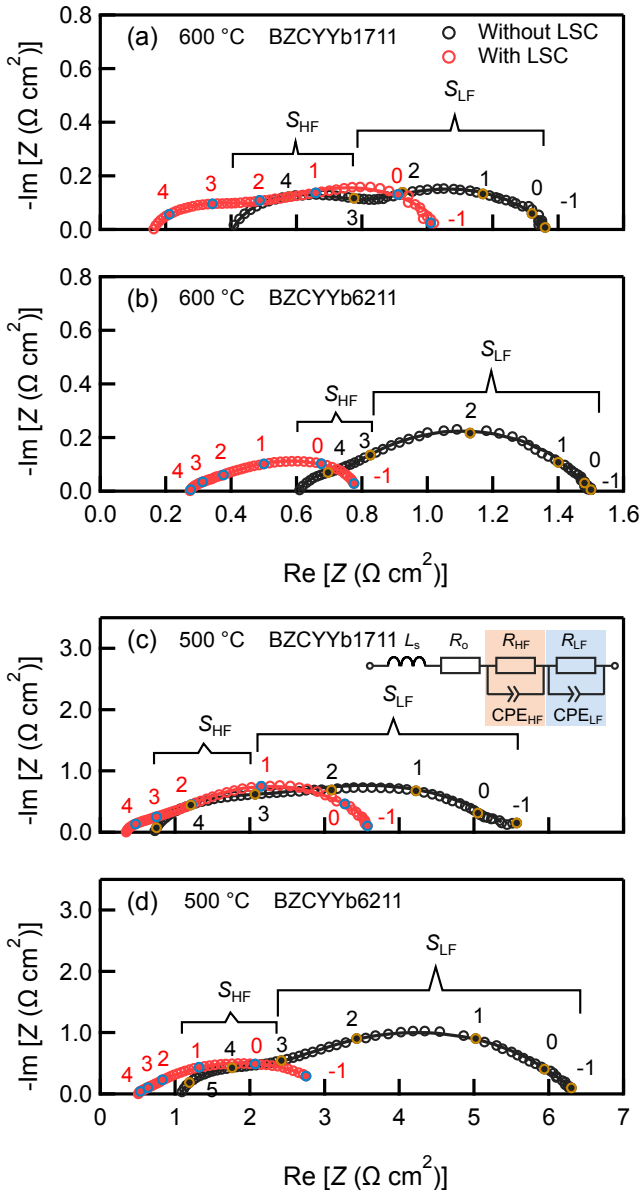

Figure 3-11 EIS of BZCYYb1711 and BZCYYb6211 cells without (black) and with (red) LSC AFL under OCV conditions. (a) and (b) The spectra at 600 °C, and (c) and (d) the spectra at 500 °C. Circles are the observed data and solid lines are the fitting results with the equivalent circuit depicted in the inset of (c).

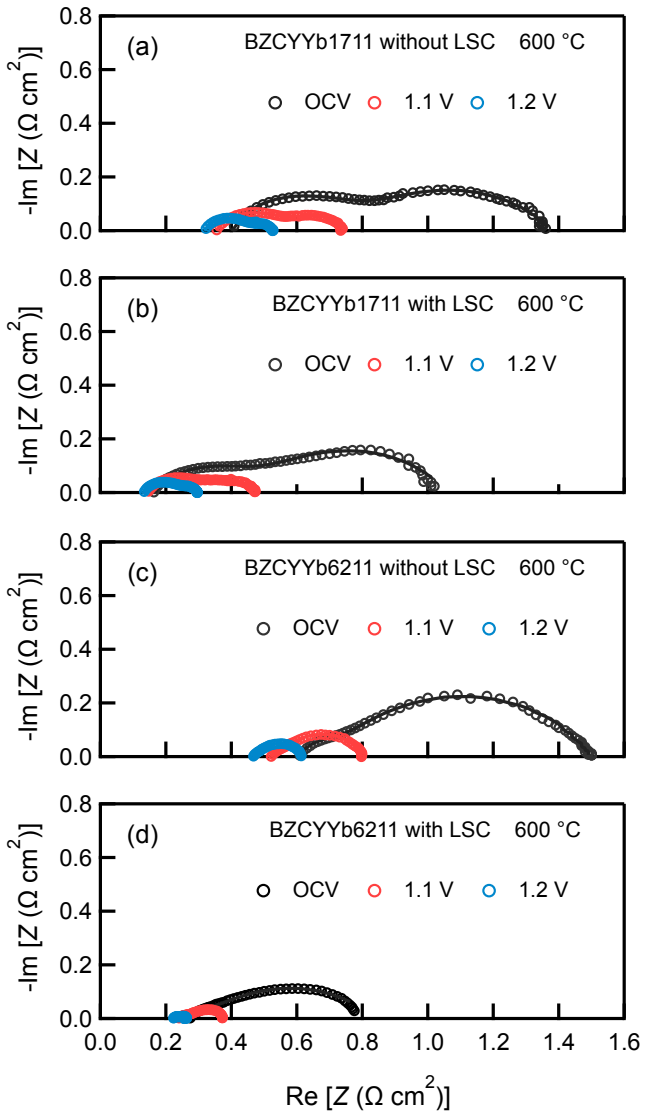

Figure 3-12 EIS of BZCYYb1711 and BZCYYb6211 cells without ((a) and (c)) and with ((b) and (d)) LSC AFL under various cell voltages at 600 °C.

Table 3-2 Parameters of equivalent-circuit fitting analysis for impedance spectra of BZCYYb1711 and BZCYYb6211 cells without and with LSC anode functional layer.

P-SOECs	T (°C)	R_o (Ω cm^2)	S_{HF} arc			S_{LF} arc		
			R_{HF} (Ω cm^2)	f_{HF} (Hz)	E_a (eV)	R_{LF} (Ω cm^2)	f_{LF} (Hz)	E_a (eV)
BZCYYb1711	600	0.30	0.52	1.14×10^4	0.70	0.56	22.3	1.04
without LSC	500	0.61	1.29	4.38×10^3		3.66	28.2	
BZCYYb6211	600	0.52	0.21	3.50×10^4	1.15	0.77	11.2	0.95
without LSC	500	0.83	1.72	6.94×10^3		4.58	27.8	
BZCYYb6211 without LSC (LSC as anode)	600	0.49	0.10	4.98×10^4	-	0.71	11.0	-
	500	0.86	0.88	5.52×10^4		8.59	21.2	
BZCYYb1711	600	0.12	0.40	1.28×10^3	0.44	0.54	3.35	0.88
with LSC	500	0.29	0.58	2.30×10^3		2.87	7.95	
BZCYYb6211	600	0.26	0.06	8.46×10^2	0.09	0.51	3.44	0.79
with LSC	500	0.47	0.07	7.76×10^3		2.69	1.82	

In case of the cells without LSC AFL, R_o of BZCYYb1711 was lower than that of BZCYYb6211 by 20–50% in the entire measured temperature range (Figure 3-10 and 3-11). The values of BZCYYb1711 were 0.30 and 0.61 Ω cm^2 at 600 and 500 °C, respectively, whereas those of BZCYYb6211 cells were 0.52 and 0.83 Ω cm^2 at 600 and 500 °C, respectively. The relatively large R_o of BZCYYb6211 could be attributed to the grain boundary resistances because the BZCYYb6211 film had a smaller grain size than the BZCYYb1711 film (Figure 3-2). R_o was considerably reduced with increasing cell voltage in both cells, which is probably due to the increment of both proton and hole currents by the modification of proton and hole defect profiles across the electrolyte film by the applied electrochemical potential field (Figure 3-12).[38, 39] R_o of BZCYYb1711 decreased from 0.30 to 0.27 Ω cm^2 with switching from OCV to 1.2 V at 600 °C (Figure 3-12a), and similarly, R_o of BZCYYb6211 decreased from 0.52 to 0.45 Ω cm^2 (Figure 3-12c). Figure 3-13a and b show the Arrhenius plots of R_o^{-1},

revealing that the activation energies of bulk proton conduction were 0.37 and 0.28 eV for BZCYYb1711 and BZCYYb6211, respectively, which were similar to the early corresponding reports of BZCYYb1711 (~0.40 eV) and BZCY622 (~0.33 eV).[33, 40]

The R_{HF} and R_{LF} significantly decreased with increasing cell voltage (Figure 3-12), which confirmed that the concentration overpotential owing to the slow gas diffusion was relatively small; thus, both resistances were correlated with the anode reaction kinetics. Without LSC AFL, BZCYYb1711 cells exhibited larger R_{HF} than BZCYYb6211 cells, although the R_{LF} of both cells was similar (Figure 3-11a and b). At 600 °C, R_{HF} of BZCYYb1711 and BZCYYb6211 was 0.52 and 0.21 Ω cm^2, respectively, whereas R_{LF} was 0.56 and 0.77 Ω cm^2 at OCV, respectively. Based on the reverse mode of the cathode reactions on protonic solid oxide fuel cells,[41, 42] the anode reactions in P-SOECs were roughly represented as shown in Figure 3-15a. Step-1 is the dissociative adsorption of water on the gas-electrode-electrolyte triple phase boundary (TPB), Step-2 is the electrochemical proton incorporation into BZCYYb electrolytes, Step-3 is the electrochemical diffusion of oxygenic species in LSCN, and Step-4 is the associative desorption of oxygen.[43] Each elementary step can be given as follow:

$$\text{Step-1: } H_2O(g) \longrightarrow O^{2-}(TPB) + 2H^{+}(TPB) \quad (3\text{-}1)$$

$$\text{Step-2: } O^{2-}(TPB) + 2H^{+}(TPB) + h^{+} \longrightarrow O^{-}(TPB) + 2H^{+}(ele) \quad (3\text{-}2)$$

$$\text{Step-3: } O^{-}(TPB) + h^{+} \longrightarrow O(an) \quad (3\text{-}3)$$

$$\text{Step-4: } O(an) \longrightarrow 1/2\ O_2(g) \quad (3\text{-}4)$$

Here, “an” indicates that a species is on the anode surface, “TPB” indicates species adsorbed at the electrode-gas-electrolyte triple phase boundary, and “ele” indicates the species in the electrolyte.

Several authors have reported that P-SOECs based on Ba(Zr,Ce,M)$O_{3-\delta}$ electrolytes exhibit two distinct semiarcs at approximately 10^5–10^2 Hz and 10^2–10^{-1} Hz,[21,22,37,43] mainly due to the polarization of the electrochemical reactions at the anode/electrolyte interface. In general, the low-frequency semiarc could be primarily related to the mass transfer on the anode, that is, the surface diffusion or associative desorption of oxygenic species on the anode (Step-3 and 4, respectively). The high-frequency semiarc is

probably associated with the charge transfer at the TPB, that is, electrochemical proton incorporation (Step-2).[37,41,44] In fact, these general descriptions fit the features of R_{HF} and R_{LF} in our cells. The R_{LF} of BZCYYb1711 cells was equivalent to that of BZCYYb6211 cells, indicating that the same LSCN anode purely contributed to R_{LF} (Figure 3-11a and b). In contrast, the charge transfer kinetics at TPB must vary with the electrolyte materials, such that the different R_{HF} values among both cells confirm the correlation of R_{HF} with coupled hole/proton transfer at TPB (Step-2).

Arrhenius plots of R_{HF}^{-1} and R_{LF}^{-1} under OCV indicated activation energies of 0.70 and 1.04 eV, respectively, for BZCYYb1711 (Figure 3-13c and e), and 1.15 and 0.95 eV, respectively, for BZCYYb6211 (Figure 3-13d and f). The activation energy of R_{LF} was very close to the related energy (0.77−1.21 eV) for oxide ion diffusion on cobaltite perovskite,[45] which proved the assignment of R_{LF} to the oxygen diffusion on LSCN. The activation energy of R_{HF} was similar to those (0.51−1.00 eV) of the corresponding resistance components for P-SOECs with Ba(Zr,Ce,M)$O_{3-\delta}$ electrolytes.[22,23]

EIS revealed that R_o, R_{HF}, and R_{LF} significantly decreased due to the use of LSC AFL in both BZCYYb1711 and BZCYYb6211 cells. The impact of LSC AFL on R_o was clearly demonstrated by the Arrhenius plots as shown in Figure 3-13a and b. Although the activation energies of proton conduction remained unchanged (0.37 and 0.28 eV for BZCYYb1711 and BZCYYb6211, respectively), the values of R_o almost decreased to half for BZCYYb1711 and BZCYYb6211, with the use of LSC AFL. For instance, R_o of BZCYYb1711 decreased from 0.30 to 0.12 Ω cm^2 and that of BZCYYb6211 from 0.52 to 0.26 Ω cm^2 at 600 °C under OCV (Figure 3-11a and b and Table 3-2). These results imply that R_o, that is, ohmic loss, includes large contributions of proton conduction near the anode/electrolyte interface, and thus, LSC AFL sufficiently increases the number of mobile protons or conduction paths near the interface (Figure 3-15b).

In contrast, the activation energy for R_{HF} drastically decreased with LSC AFL (Figure 3-13c and d). R_{HF} of BZCYYb1711 decreased with LSC from 0.52 to 0.40 Ω cm^2, and from 1.29 to 0.58 Ω cm^2 at 600 and 500 °C, respectively (Table 3-2), and the related activation energy decreased from 0.70 to 0.44 eV with LSC (Figure 3-13c). The

reduction in R_{HF} was more evident in BZCYYb6211 than BZCYYb1711 cells (Figure 3-13d and Table 3-2). R_{HF} decreased from 0.21 to 0.06 and from 0.72 to 0.07 Ω cm^2 at 600 and 500 °C, respectively, by using LSC AFL. Moreover, R_{HF} of the BZCYYb6211 cell with LSC AFL exhibited a less-pronounced temperature dependence, and thus, the related activation energy was equal to 0.09 eV, which was one order of magnitude smaller than the values of the cell without LSC AFL. These results indicate that LSC AFL can significantly promote hole/proton transfer at the TPB (Figure 3-15b). It is warrant noticing that the activation energy of R_{HF} of BZCYYb6211 is much smaller than that of BZCYYb1711 with LSC AFL.

The changes in R_{LF} with LSC were small in comparison to R_{HF} for both BZCYYb1711 and BZCYYb6211 cells (Figure 3-13e and f). From the Arrhenius plots of R_{LF}^{-1} under OCV, the activation energies slightly decreased from 1.04 and 0.95 eV to 0.88 and 0.79 eV for BZCYYb1711 and BZCYYb6211, respectively. This indicates that the R_{LF} is purely related to the surface kinetics of the LSCN anode.

Because the BZCYYb electrolyte is covered by a dense layer of LSC (Figure 3-4), the anode reactions occur mainly near the gas-AFL-electrode triple phase boundary (hereafter denoted as a-TPB). This strongly suggests that LSC AFL exhibits partial proton conductivity under the anode conditions of steam electrolysis, which is consistent with the report that a $La_{1-x}Sr_xCoO_{3-\delta}$ series show minor proton conduction via hydration under a relatively high p_{H2O} atmosphere.[46] Based on this, we ascribe LSC AFL as a proton-electron-oxide ion triple conducting phase.

The electrochemical proton incorporation (reaction (3-2)) can be rewritten for the cell with AFL as follows:

$$O^{2-}(\text{a-TPB})+2H^{+}(\text{a-TPB})+h^{+} \longrightarrow O^{-}(\text{a-TPB})+2H^{+}(\text{AFL}) \qquad (3\text{-}5)$$

EIS revealed that LSC significantly decreased the activation energy of R_{HF} (Figure 3-13c and d), which indicates that LSC AFL involves a decrease in the energy barrier height of electrochemical proton incorporation. Although the rate-determining step of reaction (3-5) is still unclear, the activation energy of reaction (3-5) must be smaller than that of reaction (3-2). EIS also confirmed that R_o was sufficiently decreased by the

aid of AFL. When electrochemical proton incorporation is encouraged, the proton concentration near the underlayer of the anode can be increased, which may lead to a reduction in the proton-conducting resistance.

To evaluate the activity of LSC as an anode, the BZCYYb6211 cell applied by LSC porous anode without AFL was also constructed. The LSC anode cell exhibited a current of 0.65 and 0.14 A cm^{-2} at 600 and 500 °C under 1.3 V, which are similar to the values of the corresponding cell using LSCN anode without the AFL (Figure 3-14), confirming that the LSC anode has similar activity as LSCN anode. These results prove that the effect of LSC AFL does not rely on the activity of LSC and thus AFL has inherent role to promote the electrochemical proton incorporation.

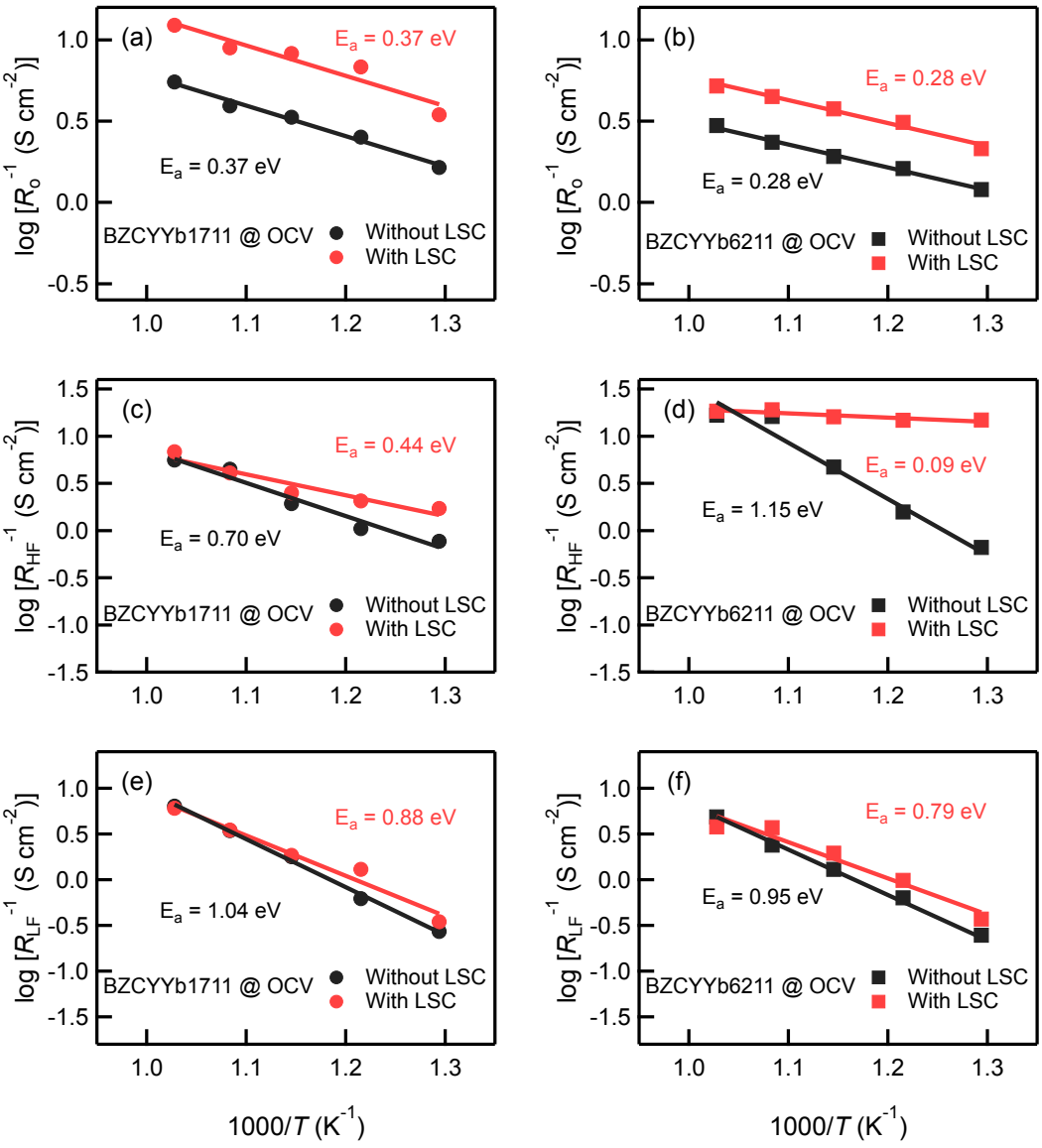

Figure 3-13 Arrhenius plots of ohmic resistances (R_o) and polarization resistances (R_{HF} and R_{LF}) of (a), (c) and (e) BZCYYb1711 and (b), (d) and (f) BZCYYb6211 cells under OCV conditions, as determined by equivalent circuit analysis. Black and red symbols show the cells without and with LSC AFL, respectively.

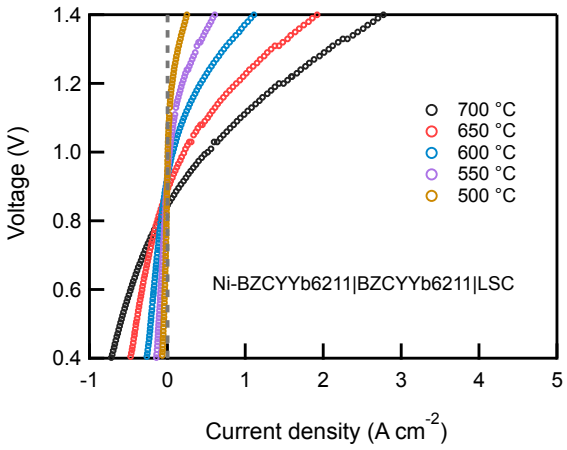

Figure 3-14 *I-V* curves of BZCYYb6211 cell with a $La_{0.5}Sr_{0.5}CoO_{3-\delta}$ (LSC) anode.

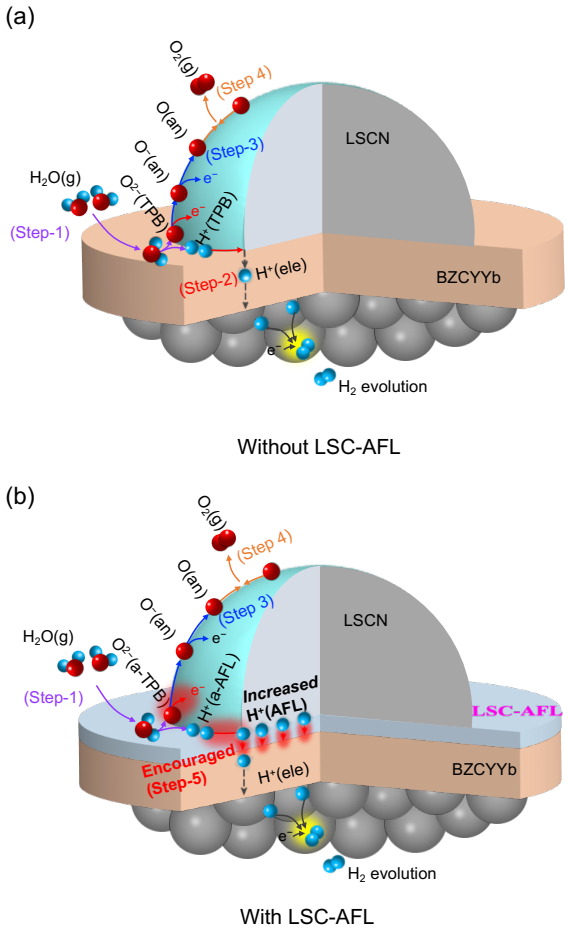

Figure 3-15 Schemes for the anode reactions of P-SOECs (a) without LSC AFL and (b) with LSC AFL at the triple-phase boundary.

3.3.4 Durability test

Finally, the long-term durability of the BZCYYb6211 electrolysis cell with LSC AFL was examined by galvanostatic electrolysis at 1 A cm^{-2} at 500 °C for 100 h (Figure 3-16a). It is known that $Ba(Zr,Ce)O_3$ solid solutions can show a higher tolerance to steam with increasing Zr content. As mentioned earlier, BZCYYb6211 cells exhibited performance similar to those of BZCYYb1711 cells with LSC AFL despite the relatively high Zr content. Hence, BZCYYb6211 is very attractive as an electrolyte for steam electrolysis cells operating under high H_2O conditions. The cell showed excellent durability with only a 1% increase in cell voltage for 100 h. The EIS of the cells before and after the long-term durability tests (Figure 3-16c) confirmed that the changes in the ohmic resistance and polarization resistance at high-frequency were relatively small (Figure 3-16b). Bulk resistance (R_o) increased from 0.31 to 0.33 Ω cm^2, whereas R_{HF} in high-frequency region of 10^5–10^3 Hz slightly decreased from 0.09 to 0.08 Ω cm^2 after 100 h of operation. R_{LF} value in low-frequency region of 10^3–10^{-1} Hz became 2.5 times higher than the value before the durability test, indicating that the deterioration of cell performance was mainly because of the degradation of the anode material, rather than the electrolyte and AFL. Anyway, these results indicate that LSC AFL can persist for a long time under the anode conditions of P-SOECs. There is a simultaneous improvement in the ohmic resistance and interfacial charge transfer resistances of P-SOECs.

The results clearly demonstrate that the LSC AFL developed in this chapter is significantly advantageous for use in P-SOECs to accelerate charge transfer at the TPB and increase the number of mobile protons or conduction paths near the anode/electrolyte interface, as shown in Figure 3-15b. In conclusion, the anode functional thin layer is a promising technology for P-SOECs and offers an opportunity to explore other active materials to improve the steam electrolysis performance at intermediate temperatures.

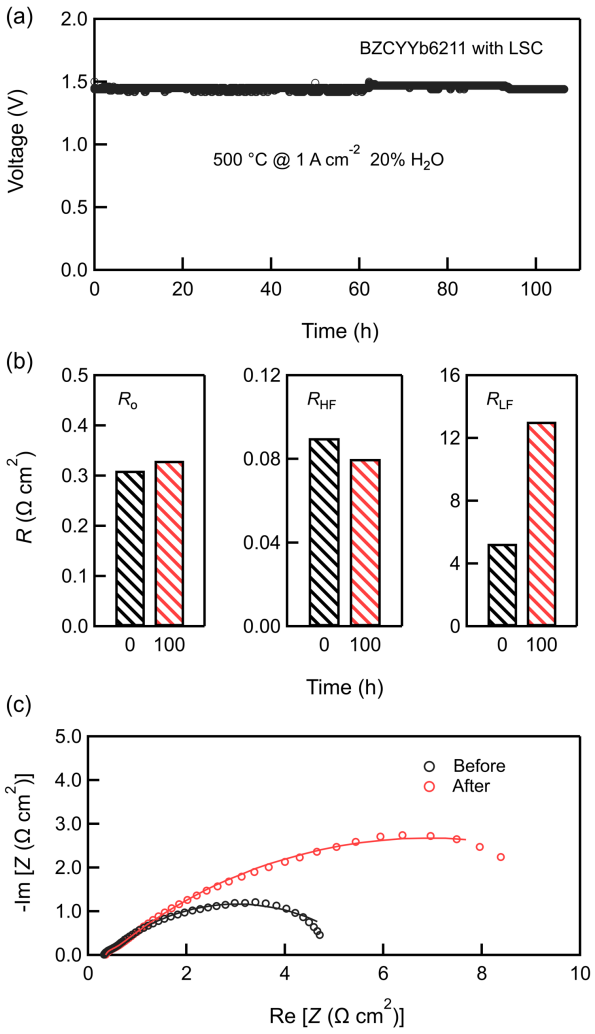

Figure 3-16 (a) Long-term durability tests of cell BZCYYb6211 with LSC AFL in 20%–H_2O/Air at 500 °C. (b) Comparison of ohmic resistances (R_o) and polarization resistances (R_{HF} and R_{LF}) before and after ~100 h operation, which was determined from the impedance spectra measured under OCV condition (c).

3.4 Conclusion

P-SOECs with or without LSC AFL were successfully fabricated using BZCYYb1711 or BZCYYb6211 as the electrolyte and LSCN as the anode in chapter 3. Here, the novel LSC AFL was demonstrated to be a promising technology for P-SOECs owing to the established connection between the anode/electrolyte. BZCYYb6211 with LSC AFL exhibited an excellent current of 1.22 A cm^{-2} at 600 °C and 1.3 V, despite the larger grain boundary surfaces compared with BZCYYb1711. This result was attributed to the decreased ohmic loss caused by the increased number of mobile protons or conduction paths near the anode/electrolyte interface and the polarization resistance at high frequencies by promoting hole or proton transfer at the anode-electrolyte-gas triple phase boundary. The BZCYYb6211 cell showed a Faraday efficiency of ~70% for H_2 evolution and excellent stability with only ~1% increment in cell voltage for 100 h. The current results offer an opportunity to explore more active anode functional materials to improve the electrochemical performance of steam electrolysis at intermediate temperatures.

3.5 References

1. L. Lei, J. Zhang, Z. Yuan, J. Liu, M. Ni and F. Chen, *Adv. Funct. Mater.*, 2019, **29**, 1903805.
2. N. Wang, S. Hinokuma, T. Ina, C. Zhu, H. Habazaki and Y. Aoki, *J. Mater. Chem. A*, 2020, **8**, 11043–11055.
3. C. Duan, J. Huang, N. Sullivan and R. O'Hayre, *Appl. Phys. Rev.*, 2020, **7**, 011314.
4. C. Duan, R. Kee, H. Zhu, N. Sullivan, L. Zhu, L. Bian, D. Jennings and R. O'Hayre, *Nat. Energy*, 2019, **4**, 230–240.
5. J. LÜ, L. Wang, L. Fan, Y. Li, L. Dai and H. Guo, *J. Rare Earths*, 2008, **26**, 505–510.
6. Z. Zhong, *Solid State Ionics*, 2007, **178**, 213–220.
7. J. Lagaeva, D. Medvedev, A. Demin and P. Tsiakaras, *J. Power Sources*, 2015, **278**, 436–444.
8. J. Lin, L. Chen, T. Liu, C. Xia, C. Chen and Z. Zhan, *J. Power Sources*, 2018, **374**, 175–180.
9. K. Joong Yoon, M. Biswas, H. J. Kim, M. Park, J. Hong, H. Kim, J. W. Son, J. H. Lee, B. K. Kim and H. W. Lee, *Nano Energy*, 2017, **36**, 9–20.
10. K. Leonard, Y. Okuyama, Y. Takamura, Y. S. Lee, K. Miyazaki, M. E. Ivanova, W. A. Meulenberg and H. Matsumoto, *J. Mater. Chem. A*, 2018, **6**, 19113–19124.
11. N. Wang, H. Toriumi, Y. Sato, C. Tang, T. Nakamura, K. Amezawa, S. Kitano, H. Habazaki, Y. Aoki, *ACS Appl. Energy Mater.* 2021, **4**, 554–563.
12. P. Sawant, S. Varma, B. N. Wani and S. R. Bharadwaj, *Int. J. Hydrogen Energy*, 2012, **37**, 3848-3856.
13. E. Fabbri, A. Depifanio, E. Dibartolomeo, S. Licoccia and E. Traversa, *Solid State Ionics*, 2008, **179**, 558-564.
14. L. Yang, S. Wang, K. Blinn, M. Liu, Z. Liu, Z. Cheng and M. Liu, *Science*, 2009, **326**, 126–129.
15. J. Kim, A. Jun, O. Gwon, S. Yoo, M. Liu, J. Shin, T. H. Lim and G. Kim, *Nano Energy*, 2018, **44**, 121–126.
16. W. Wu, H. Ding, Y. Zhang, Y. Ding, P. Katiyar, P. K. Majumdar, T. He and D. Ding, *Adv. Sci.*, 2018, **5**, 1800360.
17. K. Katahira, Y. Kohchi, T. Shimura and H. Iwahara, *Solid State Ionics*, 2000, **138**, 91–98.
18. Y. Guo, Y. Lin, R. Ran and Z. Shao, *J. Power Sources*, 2009, **193**, 400–407.
19. L. Lei, Z. Tao, X. Wang, J. P. Lemmon and F. Chen, *J. Mater. Chem. A*, 2017, **5**, 22945–22951.
20. D. Huan, N. Shi, L. Zhang, W. Tan, Y. Xie, W. Wang, C. Xia, R. Peng and Y. Lu,

ACS Appl. Mater. Interfaces, 2018, **10**, 1761–1770.

21. D. Huan, W. Wang, Y. Xie, N. Shi, Y. Wan, C. Xia, R. Peng and Y. Lu, *J. Mater. Chem. A*, 2018, **6**, 18508–18517.
22. W. Li, B. Guan, L. Ma, S. Hu, N. Zhang and X. Liu, *J. Mater. Chem. A*, 2018, **6**, 18057–18066.
23. S. Yang, Y. Wen, J. Zhang, Y. Lu, X. Ye and Z. Wen, *Electrochim. Acta*, 2018, **267**, 269–277.
24. W. Tang, H. Ding, W. Bian, W. Wu, W. Li, X. Liu, J. Y. Gomez, C. Y. Regalado Vera, M. Zhou and D. Ding, *J. Mater. Chem. A*, 2020, **8**, 14600–14608.
25. H. Ding, W. Wu, C. Jiang, Y. Ding, W. Bian, B. Hu, P. Singh, C. J. Orme, L. Wang, Y. Zhang and D. Ding, *Nat. Commun.*, 2020, **11**, 1907.
26. W. Li, B. Guan, L. Ma, H. Tian and X. Liu, *ACS Appl. Mater. Interfaces*, 2019, **11**, 18323–18330.
27. S. Yang, S. Zhang, C. Sun, X. Ye and Z. Wen, *ACS Appl. Mater. Interfaces*, 2018, **10**, 42387–42396.
28. S. Choi, T. C. Davenport and S. M. Haile, *Energy Environ. Sci.*, 2019, **12**, 206–215.
29. S. Rajendran, N. K. Thangavel, H. Ding, Y. Ding, D. Ding and L. M. Reddy Arava, *ACS Appl. Mater. Interfaces*, 2020, **12**, 38275–38284.
30. Y. Meng, J. Gao, H. Huang, M. Zou, J. Duffy, J. Tong and K. S. Brinkman, *J. Power Sources*, 2019, 439, 227093.
31. C. Sun, S. Yang, Y. Lu, J. Wen, X. Ye and Z. Wen, *J. Power Sources*, 2020, **449**, 227498.
32. L. Lei, J. Zhang, R. Guan, J. Liu, F. Chen and Z. Tao, *Energy Conver. Manag.*, 2020, **218**, 113044.
33. R. Murphy, Y. Zhou, L. Zhang, L. Soule, W. Zhang, Y. Chen and M. Liu, *Adv. Funct. Mater.*, 2020, **30**, 2002265.
34. E. Vøllestad, R. Strandbakke, M. Tarach, D. Catalan Martinez, M. L. Fontaine, D. Beeaff, D. R. Clark, J. M. Serra and T. Norby, *Nat. Mater.*, 2019, **18**, 752–759.
35. S. M. Babiniec, S. Ricote and N. P. Sullivan, *Int. J. Hydrogen Energy*, 2015, **40**, 9278–9286.
36. M. Dippon, S. M. Babiniec, H. Ding, S. Ricote and N. P. Sullivan, *Solid State Ionics*, 2016, **286**, 117–121.
37. H. Toriumi, T. Kobayashi, S. Hinokuma, T. Ina, T. Nakamura, K. Amezawa, C. Zhu, H. Habazaki and Y. Aoki, *Inorg. Chem. Front.*, 2019, **6**, 1587–1597.
38. S. Jeong, T. Yamaguchi, M. Okamoto, C. Zhu, H. Habazaki, M. Nagayama and Y. Aoki, *ACS Appl. Energy Mater.*, 2020, **3**, 1222–1234.
39. R. J. Kee, H. Zhu, B. W. Hildenbrand, E. Vøllestad, M. D. Sanders, R. P. O'Hayre, *J. Electrochem. Soc.*, 2013, **160**, F290−F300.

40. S. Jeong, T. Yamaguchi, M. Okamoto, C. Zhu, H. Habazaki, M. Nagayama and Y. Aoki, *ACS Appl. Energy Mater.*, 2020, **3**, 1222–1234.
41. F. He, T. Wu, R. Peng and C. Xia, *J. Power Sources*, 2009, **194**, 263-268.
42. E. Fabbri, L. Bi, D. Pergolesi and E. Traversa, *Adv. Mater.*, 2012, **24**, 195-208.
43. T. Kobayashi, K. Kuroda, S. Jeong, H. Kwon, C. Zhu, H. Habazaki and Y. Aoki, *J. Electrochem. Soc.*, 2018, **165**, F342–F349.
44. Y. Zhang, D. Xie, B. Chi, J. Pu, J. Li and D. Yan, *Asia-Pac. J. Chem. Eng.*, 2019, **14**, E2322.
45. M. V. Ananyev, N. M. Porotnikova and E. K. Kurumchin, *Solid State Ionics*, 2019, **341**, 115052.
46. D. Han, Y. Okumura, Y. Nose and T. Uda, *Solid State Ionics*, 2010, **181**, 1601-1606.

Chapter 4 Design of anode functional layer for protonic solid oxide electrolysis cells

4.1 Objective of chapter 4

Protonic solid oxide electrolysis cells (P-SOECs) offer advantages over oxide-ion-conducting solid oxide electrolysis cells (SOECs); they do not require hydrogen purification[1] and undergo lesser thermal corrosion due to moderate operating temperatures (400–700 °C)[2,3]. Despite these advantages, recent P-SOECs exhibit several serious drawbacks related to high anode polarization resistances and low Faradaic efficiencies, which are due to the sluggish four-electron transfer oxygen evolution reaction (OER) of anode and the generation and migration of hole from anode to electrolyte happen, thus, cause electron leakage, respectively.

The anode reaction on the P-SOECs is progressive at the triple boundary of the proton-conducting phase, electron conducting phase, and gas phase. Hence, it is highly desirable to design anode materials with a triple conductivity for protons, oxide ions, and electrons for P-SOECs, instead of mixed O^{2-}/e^- double-conducting materials for SOECs, as a means to extend the effective reaction area. Cells with $H^+/O^{2-}/e^-$ triple-conducting phases, $BaCo_{0.4}Fe_{0.4}Zr_{0.1}Y_{0.1}O_{3-\delta}$ (BCFZY),[4] $PrNi_{0.5}Co_{0.5}O_{3-\delta}$ (PNC),[5] $PrBa_{0.5}Sr_{0.5}Co_{2-x}Fe_xO_{5+\delta}$ (PBSCF),[6–9] $NdBa_{0.5}Sr_{0.5}Co_{1.5}Fe_{0.5}O_{5+\delta}$ (NBSCF),[10] and $PrBa_{0.8}Ca_{0.2}Co_2O_{5+\delta}$ (PBCC)[11] have been reported to achieve high performance over 1 A cm^{-2} at 600 °C under 1.3 V for steam electrolysis, possibly due to the reduction of anode polarization by spatially expanding reaction zones to the whole anode particles from the triple-phase boundary (TPB). Theoretical analysis clarifies that enhanced anodic reaction kinetics is crucial for increasing the Faradaic efficiency of electrolysis, because the rate of hole injection into the $Ba(Zr,Ce,M)O_{3-\delta}$ electrolyte is inversely proportional to the rate of the interfacial anode reaction.[12] Therefore, the design of efficient anode reaction zones with a high proton- and electron-conductive phase is crucial to address issues related to the polarization resistance and Faradaic efficiency.

In chapter 3, the use of the well-known O^{2-}/e^- double-conducting $La_{0.5}Sr_{0.5}CoO_{3-\delta}$

(LSC) film (90 nm) at the anode-electrolyte interface could decrease the ohmic and polarization resistances of $BaZr_{0.6}Ce_{0.2}Y_{0.1}Yb_{0.1}O_{3-\delta}$ (BZCYYb6211) base cells. This finding indicates that the effects of the anode functional layer (AFL) widely range from enhanced interfacial proton transfer to the anode reaction kinetics. Hence, there is considerable motivation to explore optimal materials as AFL (Figure 4-1). In this chapter, a series of double- or triple-conducting oxides ($LaSrCoO_{4+\delta}$ (LSC4) $La_{0.5}Sr_{0.5}CoO_{3-\delta}$ (LSC), $LaNiO_{3-\delta}$ (LNO) or $Ba_{0.95}La_{0.05}Fe_{0.8}Zn_{0.2}O_{3-\delta}$ (BLFZ), $BaCo_{0.4}Fe_{0.4}Zr_{0.1}Y_{0.1}O_{3-\delta}$ (BCFZY), $BaPr_{0.8}Y_{0.2}O_{3-\delta}$ (BPY), $PrBa_{0.5}Sr_{0.5}Co_{1.5}Fe_{0.5}O_{5-\delta}$ (PBSCF) were applied as interfacial functional layers (~100–140 nm) between the $La_{0.6}Sr_{0.4}Co_{0.2}Fe_{0.8}O_{3-\delta}$ (LSCF) anode and electrolyte in BZCYYb6211-based P-SOECs.

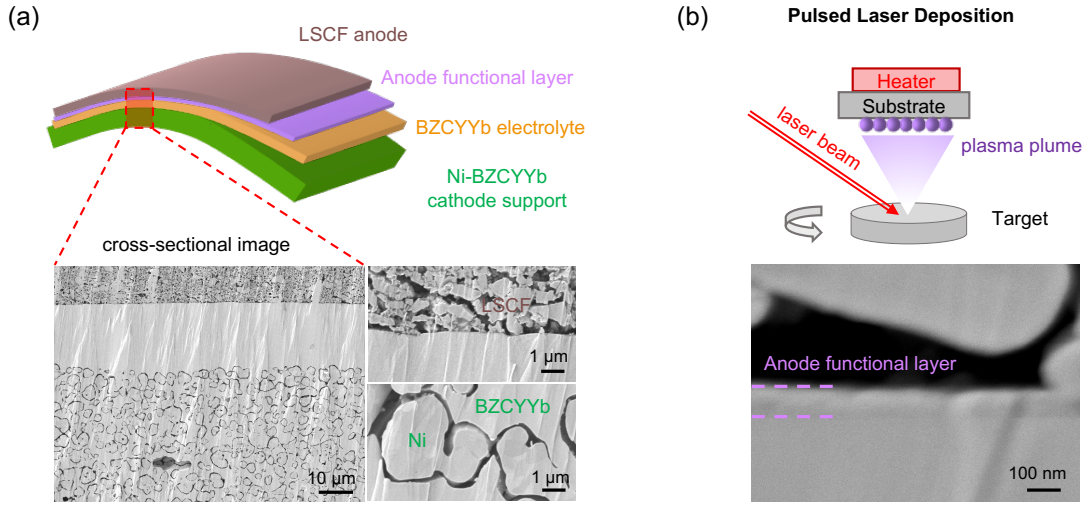

Figure 4-1 Structural configuration of P-SOECs. (a) Cross-sectional SEM image of cathode-supported P-SOECs. (b) Anode functional layer (AFL) prepared by pulsed laser deposition (PLD).

4.2 Experimental section

4.2.1 Material synthesis

LSC4, PBSCF, and BLFZ powders were synthesized by a citrate precursor route, where citric acid (CA; $C_6H_8O_7 \cdot H_2O$, 99.5%, Kanto Chemical Co.) was used as a

chelating agent at a molar ratio of CA : LSC4 (PBSCF, BLFZ) = 2:1. The precursor solution of LSC4 was prepared by dissolving the required stoichiometric amounts of $La(NO_3)_3 \cdot 6H_2O$ (99.99%, Kanto Chemical Co.), $Sr(NO_3)_2$ (98%, Kanto Chemical Co.), and $Co(NO_3)_2 \cdot 6H_2O$ (98%, Kanto Chemical Co.) in Milli-Q H_2O with CA. The gelatinous product was obtained by heating and stirring to evaporate H_2O and promote polymerization. The gel was calcined at 500 °C for 1 h, following which the ground precursor powder was calcined at 1000 °C in air for 8 h. The LSC4 powders were pelletized into a disk and subsequently sintered at 1100 °C for 6 h to obtain the target for pulsed laser deposition (PLD). PBSCF and BLFZ targets were prepared at 1000 °C and 1200 °C for 6 h, respectively by the same process, using $Pr(NO_3)_3 \cdot nH_2O$ (99.5%, FUJIFILM Wako Pure Chemical Corporation), $Ba(NO_3)_2$ (99%, Kanto Chemical), $Sr(NO_3)_2$, $Co(NO_3)_2 \cdot 6H_2O$, $Fe(NO_3)_3 \cdot 9H_2O$ (99.9%, Wako Pure Chemical Industries), and $La(NO_3)_3 \cdot 6H_2O$, and $Zn(NO_3)_2 \cdot 6H_2O$ (99.9%, FUJIFILM Wako Pure Chemical Corporation). The calcined temperatures of powders and PLD target for LSC were 900 and 1100 °C, for BCFZY were 1100 and 1200 °C. The method for LNO and BPY was modified as described in chapter 2.1.

4.2.2 Fabrication of half-cell and AFL

BZCYYb6211 powder was prepared with stoichiometric quantities of $BaCO_3$ (99.95%, High Purity Chemicals), ZrO_2 (98%, High Purity Chemicals), CeO_2 (99.99%, High Purity Chemicals) Y_2O_3 (99.99%, High Purity Chemicals), and Yb_2O_3 (99.9%, High Purity Chemicals), as described in chapter 3.2 The mixture was ball-milled for 10 h and calcined at 1300 °C in air for 10 h. Milling and calcination were repeated to ensure the formation of the BZCYYb6211 phase. Cathode-supported half-cell with a configuration of NiO-BZCYYb6211|BZCYYb62211 was fabricated by spin coating. The porous cathode was prepared by ball milling NiO (99.97%, High Purity Chemicals), BZCYYb6211, and starch (Kanto Chemical Co.) with a weight ratio of 60:40:10 for 10 h in ethanol. The mixed powder was mechanically pressed into pellets using a uniaxial press (20 MPa for 1 min) and a cold isostatic press (100 MPa for 1 min). The BZCYYb6211 electrolyte layer was spin-coated on both surfaces of the pellet with a

slurry, which was prepared by dispersing the electrolyte powder with 1 wt% NiO into a solution containing a binder (5 wt% surfactant dissolved in α-terpineol) and dispersant (20 wt% polyethyleneimine (*M*w 28 000) dissolved in α-terpineol), followed by exposure to 1500 °C for 10 min and sintering at 1450 °C in air for 8 h to form a half-cell. The back side of the sintered disc was polished using SiC paper. A thin AFL was grown on the BZCYYb6211 electrolyte layer surface via PLD with an Ulvac UPS-10000S ultravacuum chamber system, as shown in Figure 4-1b. The substrate was maintained at 700 °C for thin film growth. The target was ablated by a KrF excimer laser (248 nm, Coherence Comp109) with an energy of 102 mJ pulse^{-1} and a repetition rate of 5 Hz under an oxygen pressure of 21 Pa for 10 min. The phase of the thin film grown on the silicon wafer was characterized using GIXRD (Rigaku, RINT-2000).

4.2.3 Characterization

A commercial LSCF ink (Fuelcellmaterials) was screen-printed on the BZCYYb6211 electrolyte or the AFL as the anode. Pt (Tanaka Co.) paste was painted on the surface of the cathode for current collection. Before measurements, the cells were preannealed at 800 °C to facilitate the adhesion of the LSCF anode. The current–voltage (*I–V*) characteristic curves, electrochemical impedance spectra and Faradaic efficiency were measured as described in chapter 3.2.4. The microstructures of the post-test cells were examined using field-emission scanning electron microscopy (FESEM, SIGMA500, ZEISS). Element mapping and HRTEM images were obtained using a field-emission TEM (Titan^{3TM} G2 60-300) equipped with an EDS apparatus. The samples for TEM were prepared using the focused ion beam technique (HITACHI FB-2100).

4.3 Results

4.3.1 Structural characterization of AFLs

In this study, four triple conductors, PBSCF, BLFZ, BCFZY, and $BaPr_{0.8}Y_{0.2}O_{3-\delta}$ BPY, and three double conductors, LSC, LSC4**,** and LNO were studied. Figure 4-2a, b, and c, show the grazing incidence X-ray diffraction (GIXRD) patterns of the LSC4, PBSCF, and BLFZ thin films deposited on a Si wafer by pulsed laser deposition (PLD) at 700 °C. All diffraction peaks are consistent with those of LSC4 ($LaSrCoO_4$, PDF-50-0093), PBSCF ($PrBaCo_2O_{5.68}$, PDF-53-0131), and BLFZ ($BaFeO_{3-\delta}$, PDF-75-0426), respectively, confirming the formation of LSC4, PBSCF, and BLFZ as a single phase. The surface SEM images show that the dense LSC4, PBSCF, and BLFZ thin films are composed of particles sized tens to hundreds of nanometers, respectively (Figure 4-2d, e and f). Thin films of LNO, LSC, BCFZY, and BPY could also be obtained by PLD as shown in Figure 4-3.

XRD measurements of the pulverized BZCYYb6211 thin film cells confirmed that the oxide preserves a single phase of the cubic perovskite without severe reactions with NiO through sintering at 1450 °C (Figure 4-4a). The BZCYYb6211 electrolyte film is a uniform polycrystalline layer, in which 3–4 μm-sized grains are tightly bound to each other without forming cracks and pinholes (Figure 4-4b). The cross-sectional SEM images of P-SOECs with a BLFZ AFL confirmed that dense BZCYYb6211 electrolyte films (14 μm thickness) were precisely formed over the porous cermet cathodes, and that the LSCF anode is a porous layer consisting of sub-100 nm-sized particles (Figure 4-5). The BLFZ AFL thin film deposited by PLD fully covered the surface of the electrolyte with a thickness of approximately 140 nm (Figure 4-5h). Similarly, the AFLs of other oxides were also formed as a uniform thin film (Figure 4-5h and Figure 4-6).

The microstructures of LSC4 and BLFZ grown on the BZCYYb6211 electrolyte were identified in detail by high-resolution transmission electron microscopy (HRTEM). The cross-sectional TEM images of the BLFZ thin film and BZCYYb6211 electrolyte interface indicate that BLFZ is highly dense and maintains a sharp interface with BZCYYb6211 (Figure 4-7). The images also reveal clear lattice fringes with

interplanar lattice distances of 0.29 and 0.40 nm (Figure 4-7b), which are consistent with the (110) and (100) crystal planes of BLFZ, respectively. The energy dispersive X-ray spectroscopy (EDX) mapping (Figure 4-7c) unequivocally indicates a homogenous distribution of metal atoms. The HRTEM image of the LSC4 thin film also confirmed that well-defined films could be formed by PLD (Figure 4-8).

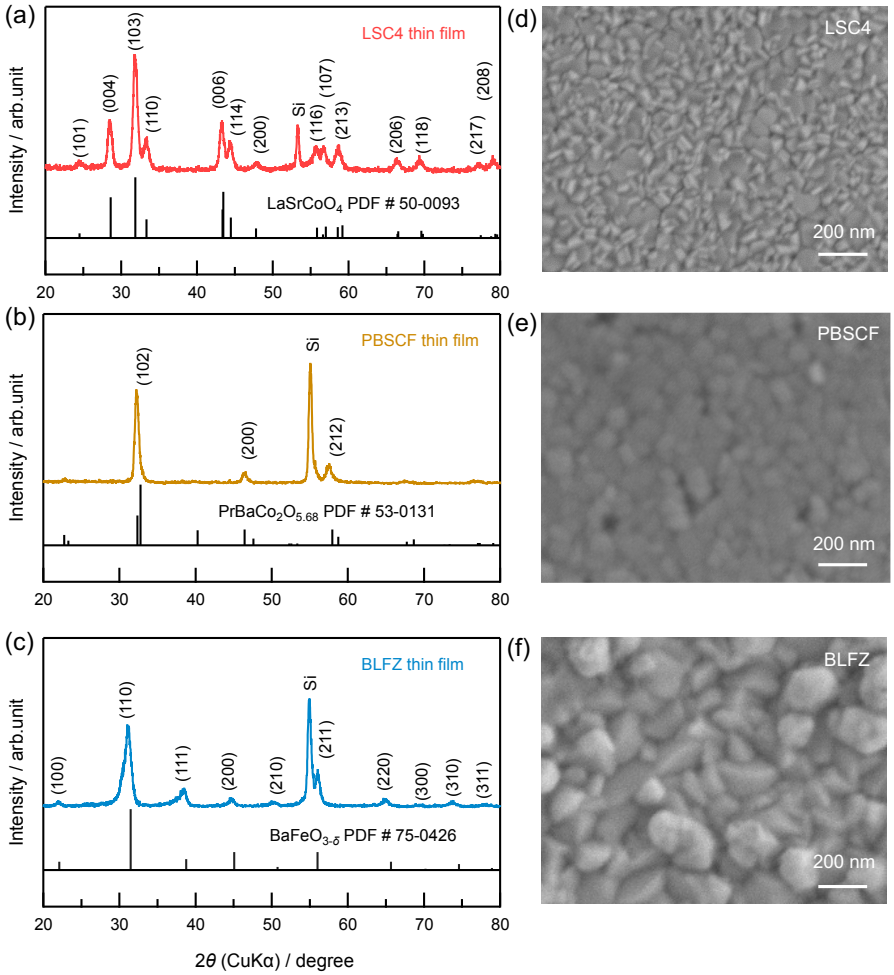

Figure 4-2 GIXRD patterns and the surface SEM images of LSC4, PBSCF and BLFZ thin films deposited on a silicon wafer.

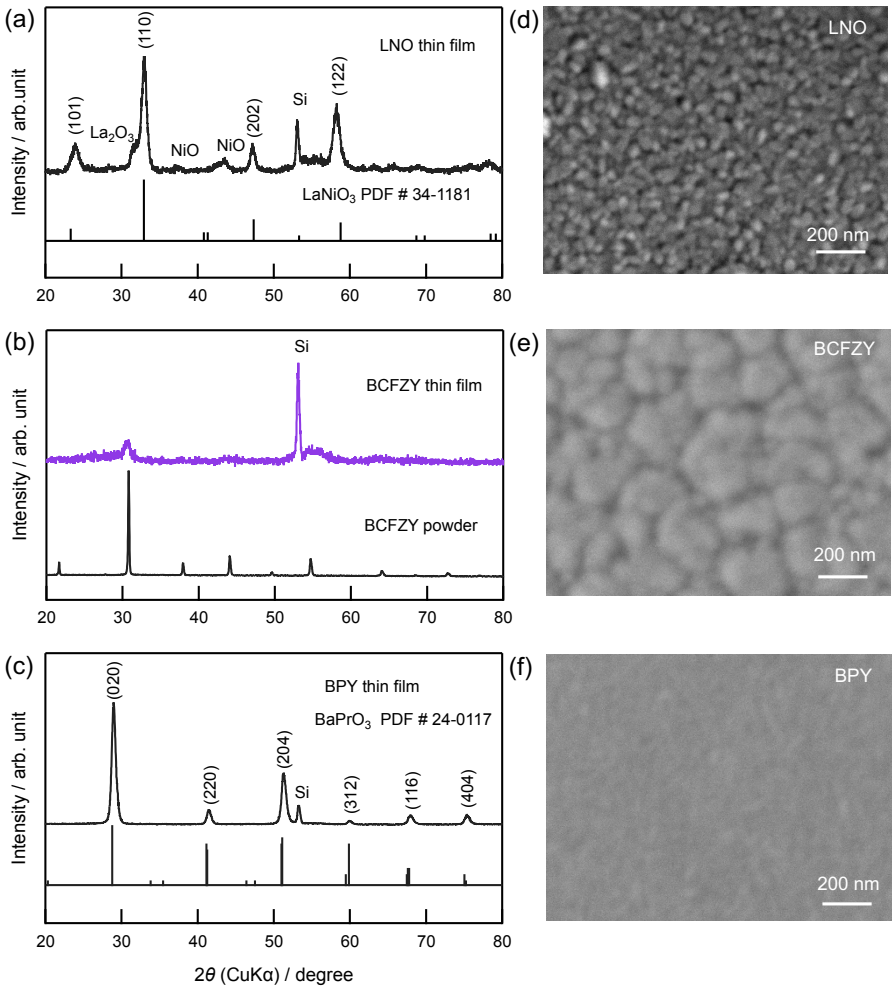

Figure 4-3 GIXRD patterns and the surface SEM images of LNO, BCFZY and BPY thin films deposited on a silicon wafer.

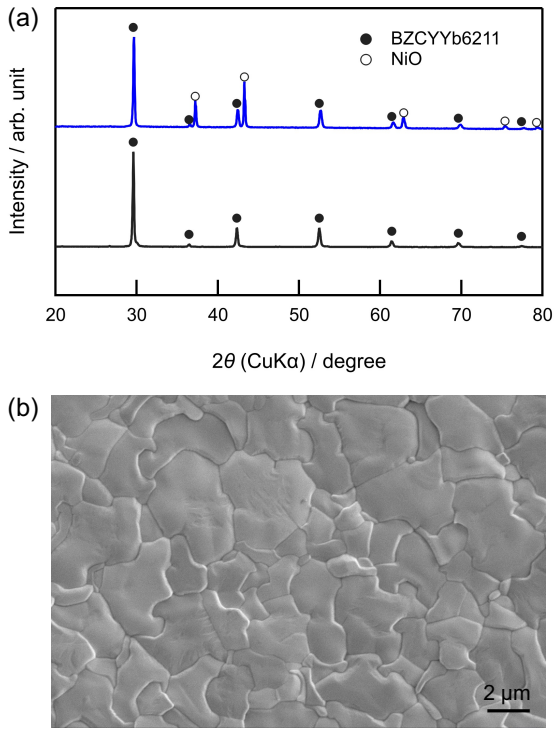

Figure 4-4 XRD and surface SEM image of BZCYYb6211 based cell. (a) Powder XRD patterns of as synthesized BZCYYb6211 at 1300 °C for 10 h and BZCYYb6211-NiO composite bulk at 1450 °C for 8 h. (b) Surface SEM image of BZCYYb6211 electrolyte film.

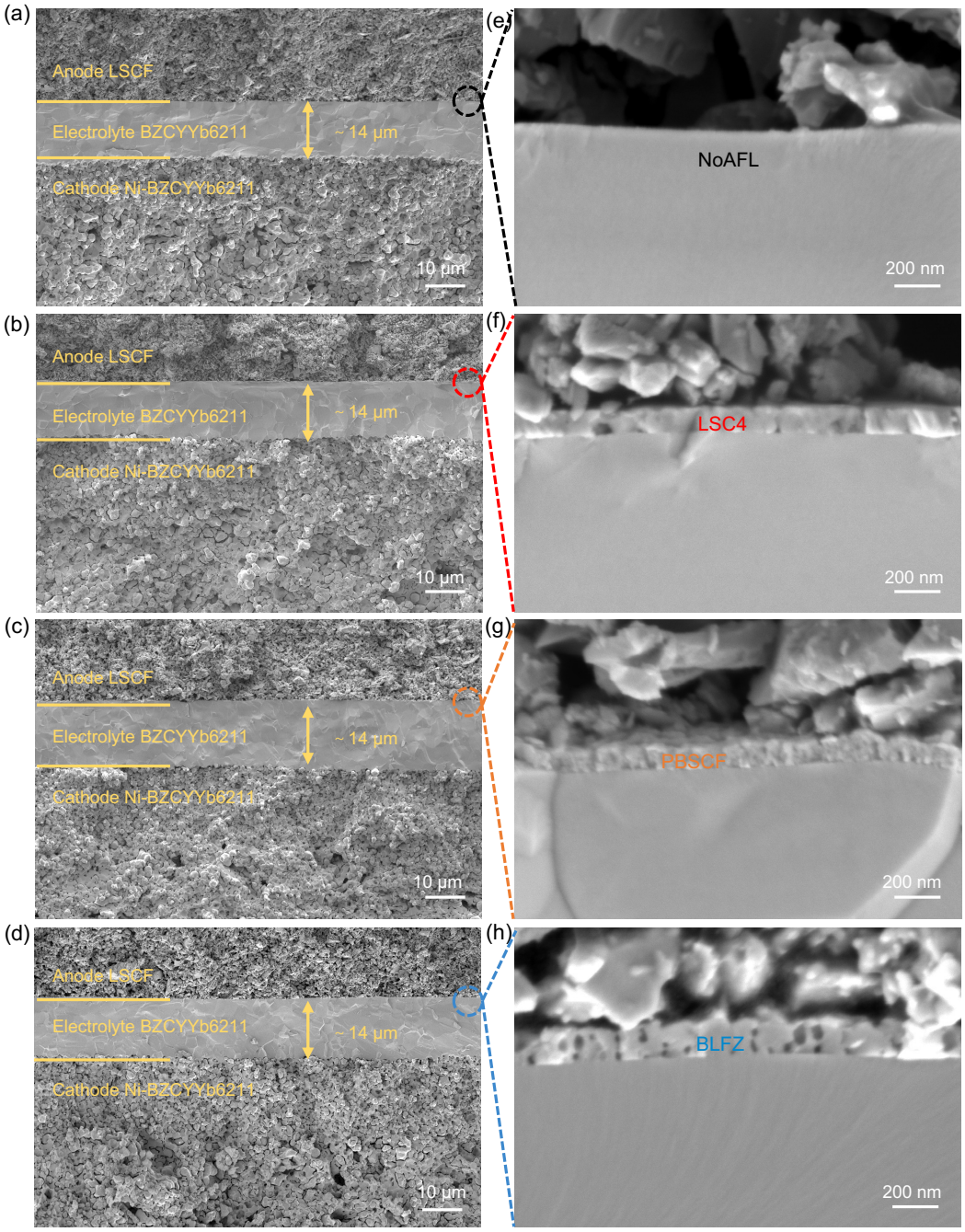

Figure 4-5 Cross-sectional SEM images of Ni-BZCYYb6211 cathode-supported P-SOECs. (a) Cell without anode functional layer (NoAFL). (b)-(d) Cells with LSC4, PBSCF, and BLFZ AFL, respectively. (e)-(h) Corresponding enlarged SEM images of interfaces between LSCF anode and BZCYYb6211 electrolyte.

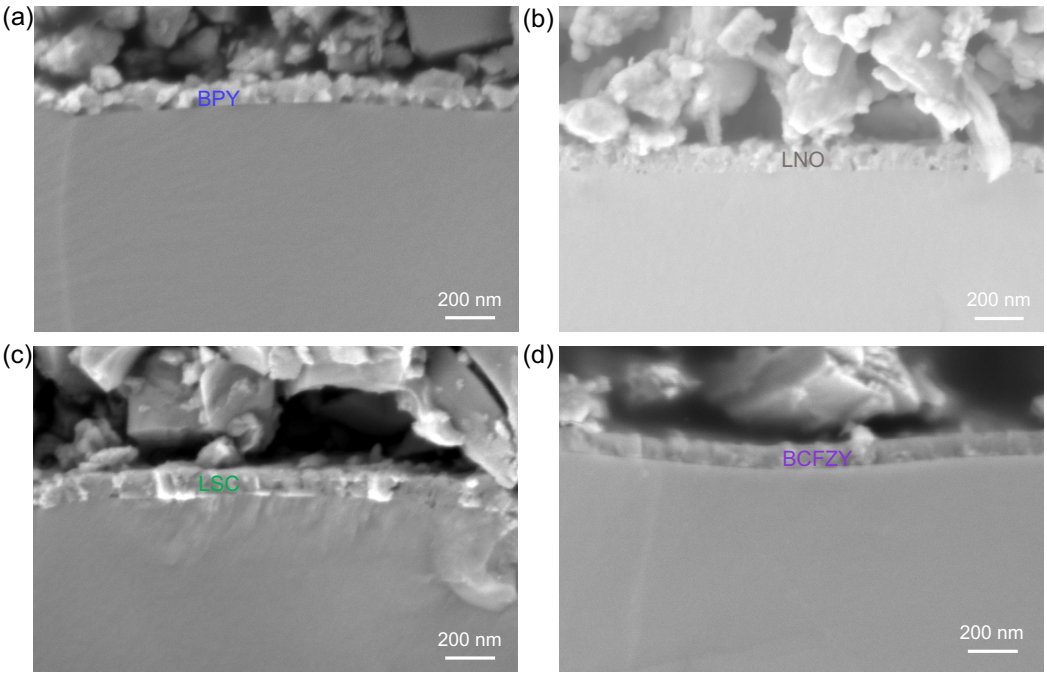

Figure 4-6 Cross-sectional SEM images of the interfaces between LSCF anode and BZCYYb6211 electrolyte of various AFL cells. (a) BPY. (b) LNO. (c) LSC. (d) BCFZY.

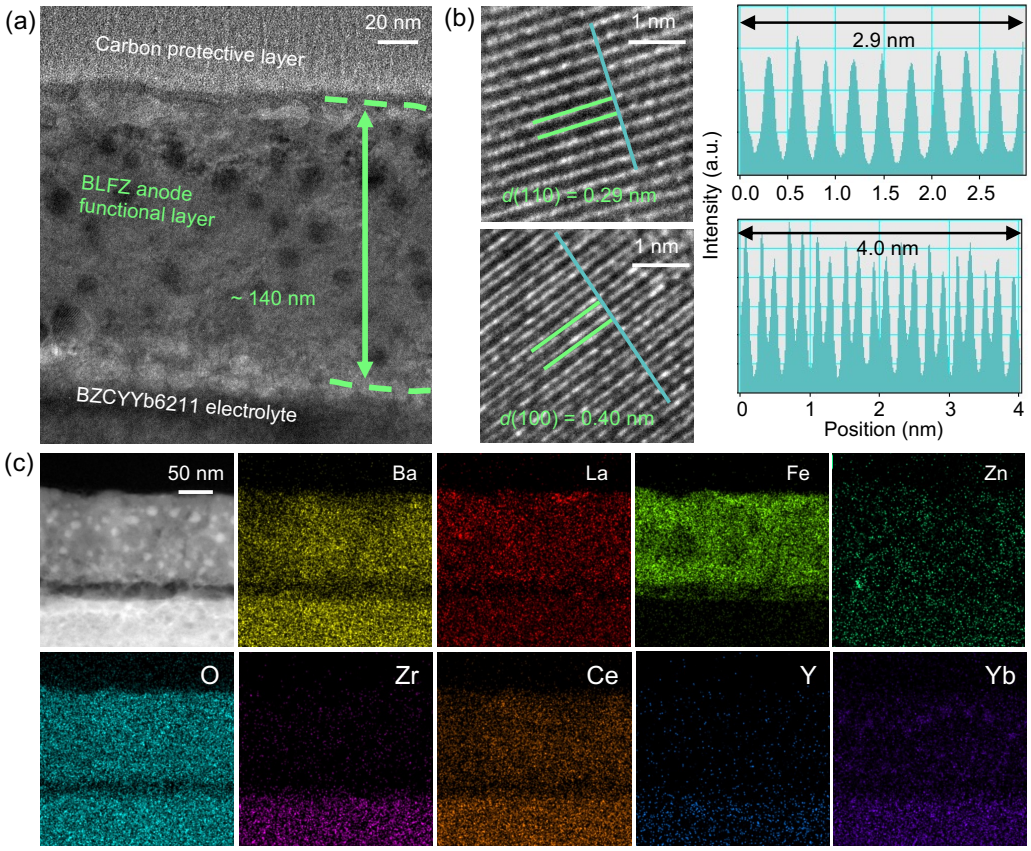

Figure 4-7 High-resolution electron micrographs of BLFZ thin films. (a) Cross-sectional TEM image of interfaces between the BLFZ interlayer and BZCYYb6211 electrolyte. (b) Lattice fringes of BLFZ and corresponding line scan histogram along the blue line. (c) EDX element mapping of BLFZ thin film.

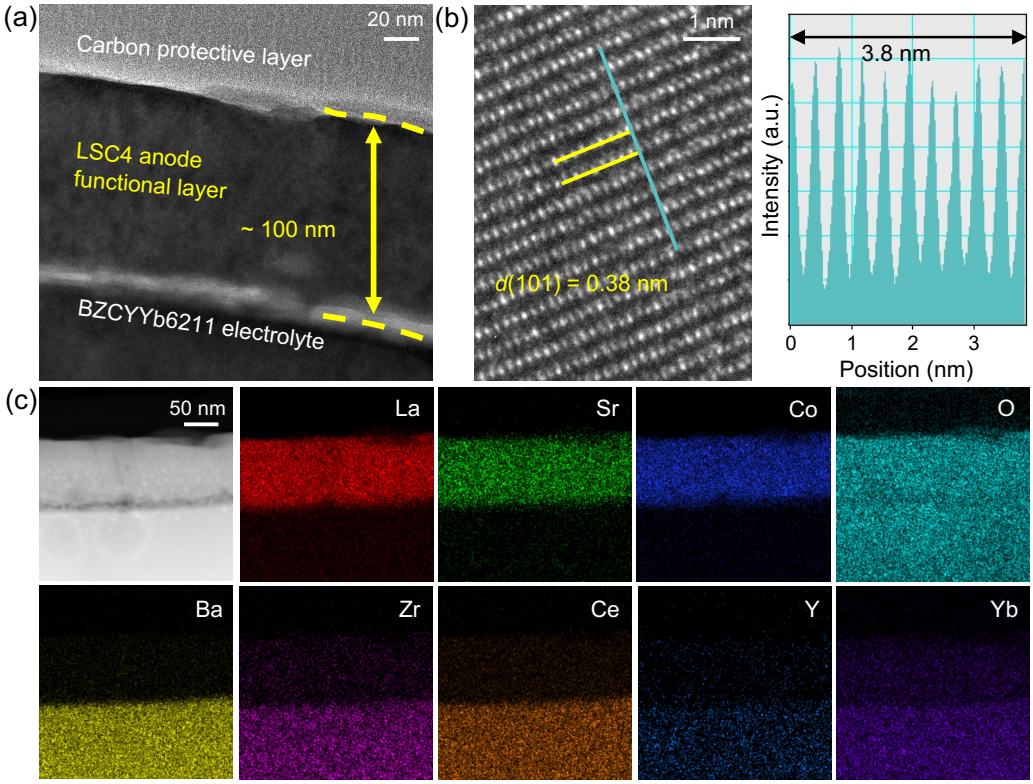

Figure 4-8 High-resolution electron micrographs of LSC4 thin films. (a) Cross-sectional TEM image of interfaces between the LSC4 interlayer and BZCYYb6211 electrolyte. (b) Lattice fringes of LSC4 and corresponding line scan histogram along the blue line. (c) EDX element mapping of LSC4 thin film.

4.3.2 Electrochemical performance of P-SOECs

A series of well-known oxide electrodes for solid oxide fuel cells (SOFCs) or protonic solid oxide fuel cells (H-SOFCs) have been examined as AFLs, including O^{2-}/e^- double conductors of LSC4,[13] LNO,[14] and LSC,[15,16] and H^+/O^{2-}/e^- triple conductors of BCFZY,[4,17,18] BPY,[19] BLFZ,[20,21] and PBSCF[6–9]. All AFLs were formed by PLD with thicknesses adjusted to approximately 100–140 nm (Figure 4-5 and Figure 4-6). Figure 4-9a shows the temperature dependence of the OCVs by supplying a 30%-H_2O/air gaseous mixture to the anode and humidified 10%H_2/Ar to the cathode. The OCVs of the cell without the AFL (NoAFL cell) are 0.91 and 0.96 V at 600 and 500 °C, respectively. The OCVs of the cells vary with the AFL, and the values can be classified into three categories. The cells with LSC and PBSCF AFLs exhibit similar OCVs as the NoAFL cell, as indicated by the black symbols in Figure 4-9a. The cells of the LSC4 and LNO AFLs, indicated by red symbols in Figure 4-9a, possess lower OCVs than those of the NoAFL cell, which are equal to 0.87 and 0.91 V for LSC4 and 0.87 and 0.94 V for LNO at 600 and 500 °C, respectively. However, the OCVs of BCFZY, BPY, and BLFZ, as indicated by the blue symbols in Figure 4-9a, are apparently higher than those of the NoAFL cells, for example, 0.94 and 1.00 V at 600 and 500 °C for the BLFZ AFL cell.

Figure 4-9b-f and Figure 4-10, show the current–voltage (*I–V*) characteristics of the P-SOECs in the fuel cell and electrolysis modes. Here, the electrolysis mode is represented by a positive current. The steam electrolysis currents of the NoAFL cell are 848, 395, and 117 mA cm^{-2} at 700, 600, and 500 °C, respectively, for a bias of 1.3 V, which is close to the thermal neutral voltage of water splitting at 600 °C (1.28 V; Figure 4-9b).[1,22] These currents are similar to those in early reports of P-SOECs with the BZCYYb4411 electrolyte and LSCF anode.[23] The electrolysis currents of P-SOECs widely vary with the choice of AFL. Figure 4-9g plots the currents at 1.3 V for various AFL cells. The LSC4, PBSCF, and BLFZ AFLs largely increase the currents in the range of 500 to 700 °C. On the other hand, the BPY, LNO, and BCFZY perovskite AFLs exhibit electrolysis currents almost similar to that of the NoAFL cell.

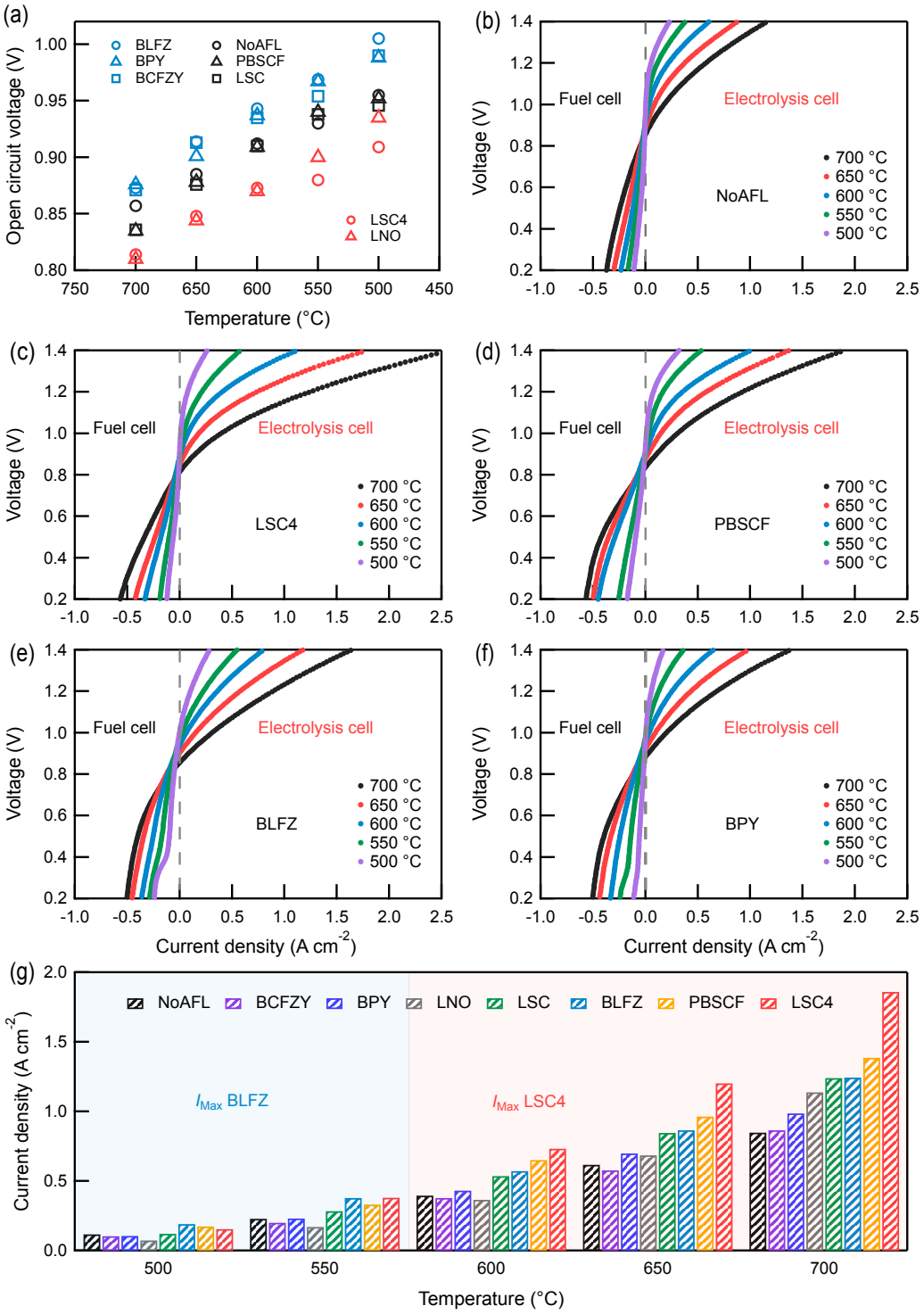

Figure 4-9 Electrochemical performance of P-SOECs without and with the AFL. (a) Open-circuit voltages (OCVs) of P-SOECs with different AFLs as a function of temperature. (b)-(f) *I–V* characteristics of the cell without the AFL (NoAFL; (b)) and the cells with (c) LSC4, (d) PBSCF, (e) BLFZ and (f) BPY AFLs, respectively. (g) Comparison of steam electrolysis currents at 1.3 V.

LSC4 is a p-type semiconductor with a Ruddlesden-Popper type structure,[24,25] and possibly exhibits oxide-ion conductivity. The OCVs of the LSC4 cells were lower than those of the NoAFL cells (Figure 4-9a). Meanwhile, the cell exhibited the highest electrolysis current of the tested AFL at temperatures above 600 °C, with electrolysis currents of 1860, 733, and 154 mA cm^{-2} at 700, 600, and 500 °C, respectively, at 1.3 V (Figure 4-9c, g), which are higher than the corresponding values of the NoAFL cell by 119%, 86%, and 32%, respectively. PBSCF is an $H^+/O^{2-}/e^-$ triple conductor with a hydration enthalpy of approximately 22 kJ mol^{-1} and a proton concentration of 3.5% per formula unit at 200 °C under p_{H2O}/p_0 = 0.020.[26] The cell shows similar OCVs as NoAFL cells in the range from 500 to 650 °C, while the currents of the former are much higher than those of the latter. The currents at 1.3 V were 1386, 651, and 173 mA cm^{-2} at 700, 600, and 500 °C (Figure 4-9d), respectively, which are higher than the corresponding currents for the NoAFL cell by 63%, 65%, and 48%, respectively.

BLFZ has a higher hydration enthalpy (~ 86 kJ mol^{-1}) than PBSCF, and hence, possesses a very high proton concentration (10% per formula unit at 250 °C under p_{H2O}/p_0 = 0.016).[20] The BLFZ cell exhibited the highest OCVs in all temperature ranges and the highest electrolysis currents at temperatures below 550 °C among the tested materials (Figure 4-9a, e, and g). The cell yielded currents of 1245, 570 and 191 mA cm^{-2} at 700, 600, and 500 °C, respectively, at 1.3 V, which are higher than the corresponding values for the NoAFL by 47%, 44%, and 63%, respectively. Hence, the three AFLs, i.e., LSC4, PBSCF, and BLFZ, which yield higher electrolysis currents than NoAFL, can be distinguished from each other according to lower, similar, and higher OCVs in comparison with the NoAFL, and together with BPY (higher OCVs), are investigated in more detail in subsequent sections.

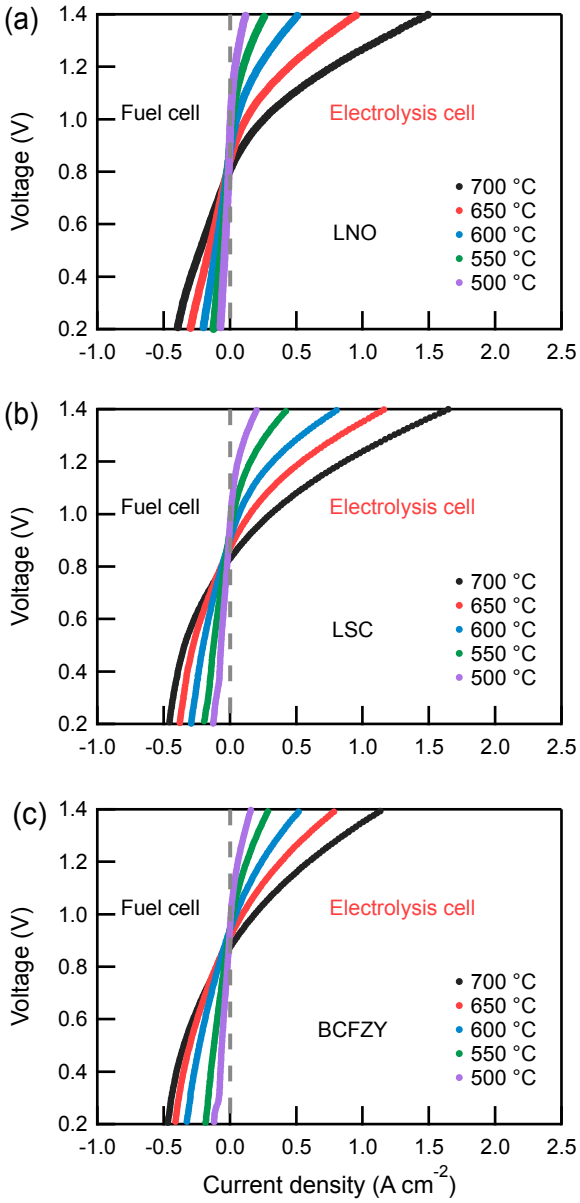

Figure 4-10 Current–voltage (*I–V*) characteristics of various AFL cells. (a) LNO. (b) LSC. (c) BCFZY.

4.3.3 Faradaic efficiency of P-SOECs

$Ba(Zr,Ce,M)O_{3-\delta}$ (M = Y, Yb, etc.) electrolytes show mixed protonic, oxide-ionic, and electronic conduction under steam electrolysis conditions. Mobile proton defects ($OH_O^{\bullet}$) are incorporated by thermodynamic hydration via the association of oxygen vacancies ($V_O^{\bullet\bullet}$) and water vapor:

$$O_O^{\times} + V_O^{\bullet\bullet} + H_2O \longrightarrow 2OH_O^{\bullet} \quad (4\text{-}1)$$

Equation (4-1) uses the Kröger–Vink notation, where $O_O^{\times}$ is the lattice oxygen. Simultaneously, the association between oxygen vacancies and oxygen gas was equilibrated:

$$V_O^{\bullet\bullet} + \frac{1}{2}O_2 \longrightarrow O_O^{\times} + 2h^{\bullet} \quad (4\text{-}2)$$

Here, $h^{\bullet}$ is an electron hole; thus, the migration of $h^{\bullet}$ from the anode to the cathode causes electron leakage, resulting in a decrease in Faradaic efficiency (η).

η was evaluated by calibrating the hydrogen evolution rate under galvanostatic conditions at 600 and 500 °C, in which the current was set to maintain the bias around the thermal neutral potential of 1.3 V (Figure 4-11 and Figure 4-12). At 600 °C, the current was set to 314 mA cm^{-2} for NoAFL (Figure 4-11a) and 570 mA cm^{-2} for BLFZ (Figure 4-11b). Both cells yielded a stable bias at approximately 1.3 V during 2 h of galvanostatic electrolysis. In every cell, the hydrogen production rate could be in equilibrium after approximately 1 h. Hence, η was precisely determined from the average hydrogen evolution rate after 1 h. The η of the NoAFL cell was relatively low (31%), which is attributed to the relatively high hole conductivity of the Zr-rich side phase of the $Ba(Zr,Ce,M)O_{3-\delta}$ electrolyte,[27,28] and the low activity of LSCF. This is consistent with previous reports, where the η of P-SOECs was approximately 20–60% when the anode employed O^{2-}/e^{-} double conductors, such as LSCF,[29] $La_{0.8}Sr_{0.2}MnO_{3-\delta}$ (LSM)[30,31] and $Ba_{0.5}Sr_{0.5}Co_{0.8}Fe_{0.2}O_{3-\delta}$ (BSCF).[29] The η of the BLFZ cell (45%; Figure 4-11b) is higher than that of the NoAFL cell (Figure 4-11a), although the current of the former is two times larger as that of the latter.

Moreover, the BLFZ AFL can achieve the highest η and current at approximately 1.3 V and 500 °C. All cells can retain the DC bias constant at approximately 1.3 V during

galvanostatic electrolysis at 500 °C, in which electrolysis currents of 70, 128, 142 and 214 mA cm^{-2} are applied to the NoAFL, LSC4, PBSCF and BLFZ cells, respectively (Figure 4-11c, d, and Figure 4-12a, b). The BLFZ cell shows an η of 75% (Figure 4-11d) at 1.3 V, which is much higher than (46%) that of the NoAFL cell (Figure 4-11c), and can maintain an η greater than 60% by applying a current of 343 mA cm^{-2} (Figure 4-12c) at 1.4 V. Meanwhile η drops to approximately 30% at 1.3 V when using LSC4 and PBSCF AFLs (Figure 4-12a, b). The η value of our PBSCF AFL cell is lower than the value reported for P-SOECs with an identical AFL (~100 nm), possibly because of the difference between the electrolyte and anode materials.[8]

BPY is favorably hydrated even at 600 °C, retaining similar number of protons as those of the $BaZr_{0.8}Y_{0.2}O_3$ proton conductor [32]. The BPY AFL could also increase the OCVs, as is the case with BLFZ, although the currents are 986, 432, and 106 mA cm^{-2} at 700, 600, and 500 °C near a bias of 1.3 V, similar to those of the NoAFL cell, as displayed in Figure 4-9a and f. Thus, the use of the BPY cell leads to a higher η (58%) than that of NoAFL at 500 °C (Figure 4-12d). These results indicate that the AFL-elevating OCVs can achieve a high η by lowering the hole leakage.

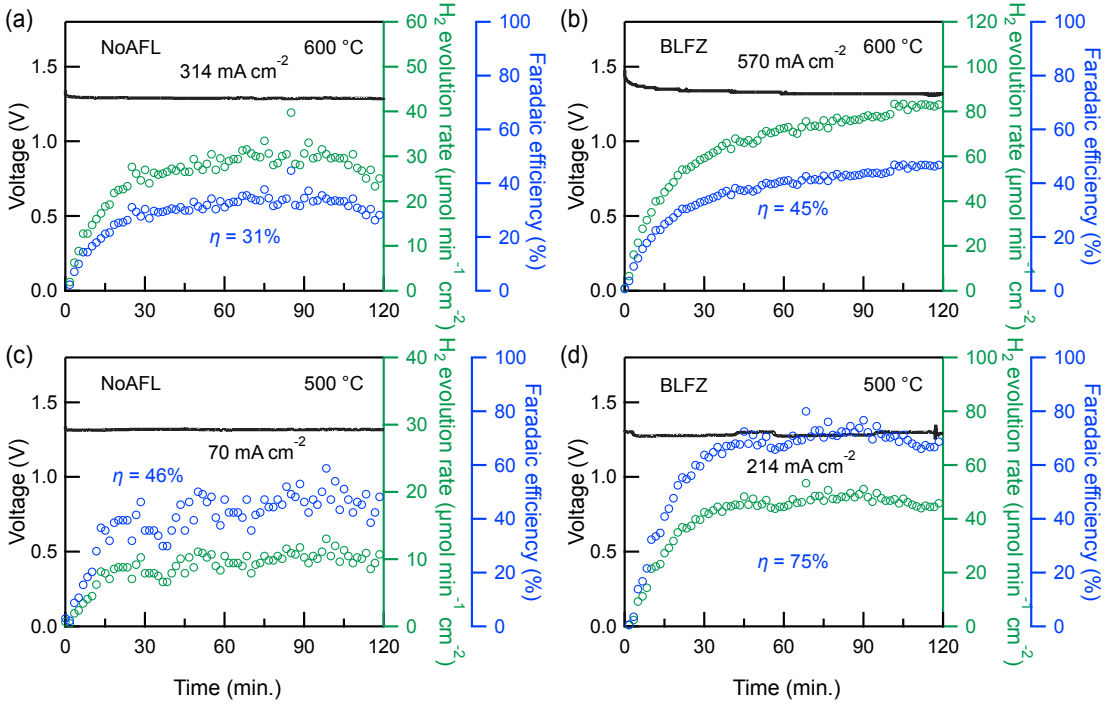

Figure 4-11 Transients of cell voltages and H_2 gas evolution rates during galvanostatic electrolysis. (a)-(b) NoAFL and BLFZ cells at 600 °C. The constant currents were set to 314 and 570 mA cm^{-2} for NoAFL and BLFZ, respectively. (c)-(d) NoAFL and BLFZ cells at 500 °C with applied currents of 70 and 214 mA cm^{-2}, respectively. Black lines depict the cell voltage, green and blue circles show the H_2 evolution rate and corresponding Faradaic efficiency (η).

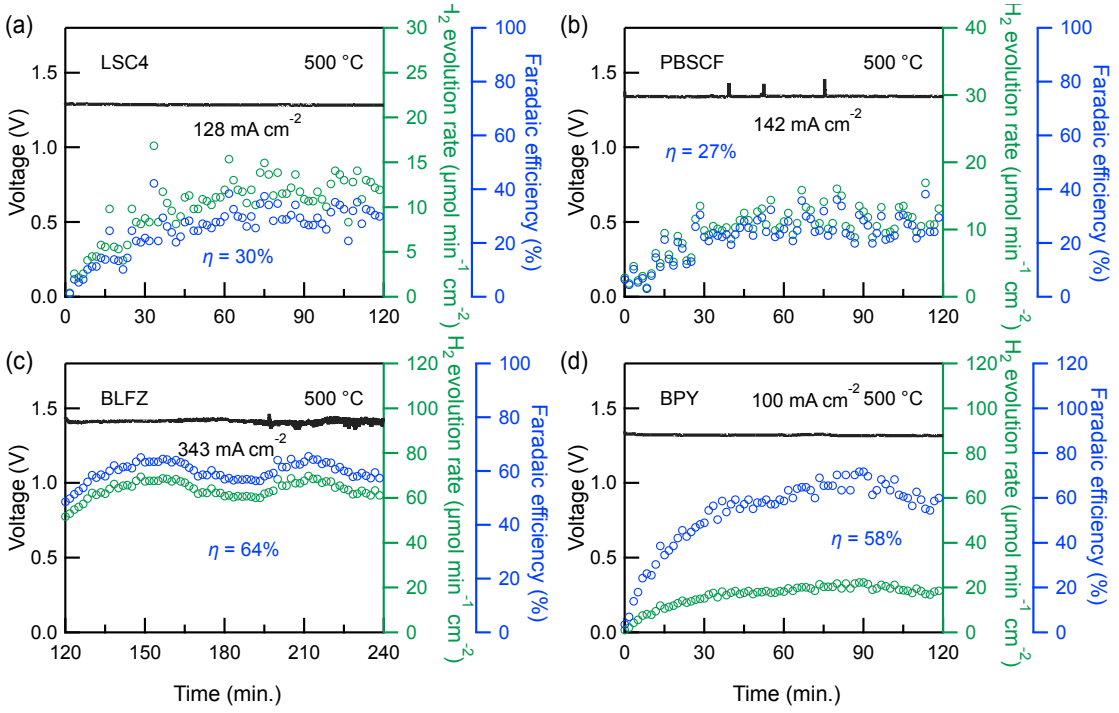

Figure 4-12 Transients of cell voltages and H_2 gas evolution rates during galvanostatic electrolysis at 500 °C. (a) LSC4 AFL cell with applied current of 128 mA cm^{-2} at 1.3 V. (b) PBSCF AFL cell with applied current of 142 mA cm^{-2} at 1.3 V. (c) BLFZ AFL cell with applied current of 343 mA cm^{-2} at 1.4V. (d) BPY AFL cell with applied current of 100 mA cm^{-2} at 1.3 V.

4.3.4 Electrochemical impedance spectroscopy

Electrochemical impedance spectroscopy (EIS) was performed to assess the polarization resistances related to the anodic reaction in the gas-anode-AFL TPB and provide insights into the functionality of the AFL (Figure 4-13). All NoAFL, LSC4, PBSCF, and BLFZ cells show impedance responses. These responses include the *x*-intercept at high frequency (> 10^5 Hz), that is, ohmic loss (R_o) arising from bulk resistances of the electrolyte, and the polarization semicircle with two (700–600 °C) or three (550 and 500 °C) distinct semicircles in the high-frequency (HF), middle-frequency (MF), and low-frequency (LF) regions at approximately 10^5–10^3 Hz, 10^3–10^1 Hz, and 10^1–10^{-1} Hz, respectively, which are denoted as S_{HF}, S_{MF}, and S_{LF} (Figure 4-13i). The anodic polarization is dominant in P-SOECs, as mentioned before, such that the total diameters of the semicircles can provide an approximate estimate of the anodic polarization resistances (R_p). Therefore, the equivalent circuit analysis with a model of R_o–(R_{HF}–CPE_{HF})–(R_{MF}–CPE_{MF})–(R_{LF}–CPE_{LF}) depicted in the inset of Figure 4-13i, was conducted to deconvolute the impedance responses, where R_o and CPE are the resistances from proton conduction in the BZCYYb6211 electrolyte and constant phase element, respectively. The parallel components of (R_{HF}–CPE_{HF}), (R_{MF}–CPE_{MF}), and (R_{LF}–CPE_{LF}) represent the S_{HF}, S_{MF}, and S_{LF} semicircles. R_{HF}, R_{MF}, and R_{LF} provide the corresponding anodic polarization resistances related to S_{HF}, S_{MF}, and S_{LF}, respectively. Hence, R_p is calculated as the sum of R_{HF}, R_{MF}, and R_{LF}. The fitting results for the NoAFL, LSC4, PBSCF, and BLFZ cells are shown as solid lines in Figure 4-14a, b, and the resultant R_o and R_p are summarized together with the results for the BPY cell in Figure 4-14c and d. R_o and R_p and the related activation energies for other AFLs are summarized in Figure 4-15 and Table 4-1.

The R_o values of the LSC4, PBSCF, and BLFZ cells are 0.54, 0.56, and 0.58 Ω cm^2 at 600 °C, respectively, all of which are nearly 50% lower than the value (1.29 Ω cm^2) of the NoAFL cell. The R_p of NoAFL cell is 2.18 Ω cm^2 at 600 °C, and decreases to 1.54, 0.97, and 0.46 Ω cm^2, which are reductions of 29%, 56%, and 79%, respectively, with the use of LSC4, PBSCF and BLFZ, respectively (Figure 4-14a). At 500 °C, the

R_o values of NoAFL, LSC4, PBSCF, and BLFZ cells are 2.06, 0.95, 1.04, and 0.89 Ω cm^2, respectively, and the corresponding R_p values are 14.04, 10.26, 5.89, and 1.85 Ω cm^2, respectively (Figure 4-14b)

The NoAFL cells were constructed with various thicknesses of the BZCYYb6211 electrolyte at 8, 14, and 30 μm, as shown in Figure 4-16a, b, and c; thus, the R_o of the cell was evaluated as a function of the electrolyte thickness (Figure 4-14e). R_o is proportional to the thickness at every temperature, and extrapolation to the linear dependence reveals the existence of a high resistance at zero thickness ($R_o(0)$), which can be assigned to the interfacial contact resistances between LSCF anode and BZCYYb6211 electrolyte. The R_o values for the cell with 0 (i.e., $R_o(0)$) and 14 μm thicknesses are 0.96 and 1.29 Ω cm^2, respectively at 600 °C, which reveals that approximately 80% of ohmic losses in NoAFL cells are due to the interfacial resistances rather than bulk resistances. The thickness dependence of R_o for the BLFZ AFL cells with different electrolyte thicknesses reveals that $R_o(0)$ becomes only 0.31, 0.41, and 0.64 Ω cm^2 at 700, 600, and 500 °C (Figure 4-14e), which are 60% lower than the corresponding values of NoAFL, verifying that the BLFZ AFL significantly decreases the interfacial protonic resistances.

BLFZ AFL possesses much lower values of R_p than other cells (Figure 4-14d, Table 4-1). Moreover, the related E_a of the former (0.78 eV) is lower than the latters (~1.0 eV), confirming the enhancement of the anodic reaction kinetics by the BLFZ AFL. The impedance spectra at 500 °C for the NoAFL, LSC4, PBSCF, BLFZ, and BPY cells were analyzed using the distribution of relaxation time (DRT) technique, which enables deconvolution of the impedance responses to resistive components at each time, as illustrated in Figure 4-14f.[33] The DRT plots could also be divided into three regions: HF, MF, and LF at approximately 10^5–10^3 Hz, 10^3–10^1 Hz, and 10^1–10^{-1} Hz, respectively. NoAFL cells possess relatively large resistive components in the LF region (Figure 4-14f). All AFLs efficiently decreased the resistances in the HF and MF regions, whereas only the BLFZ AFL could significantly decrease the resistance in the LF region. These features imply that the BLFZ AFL takes a different reaction path from the NoAFL cells.

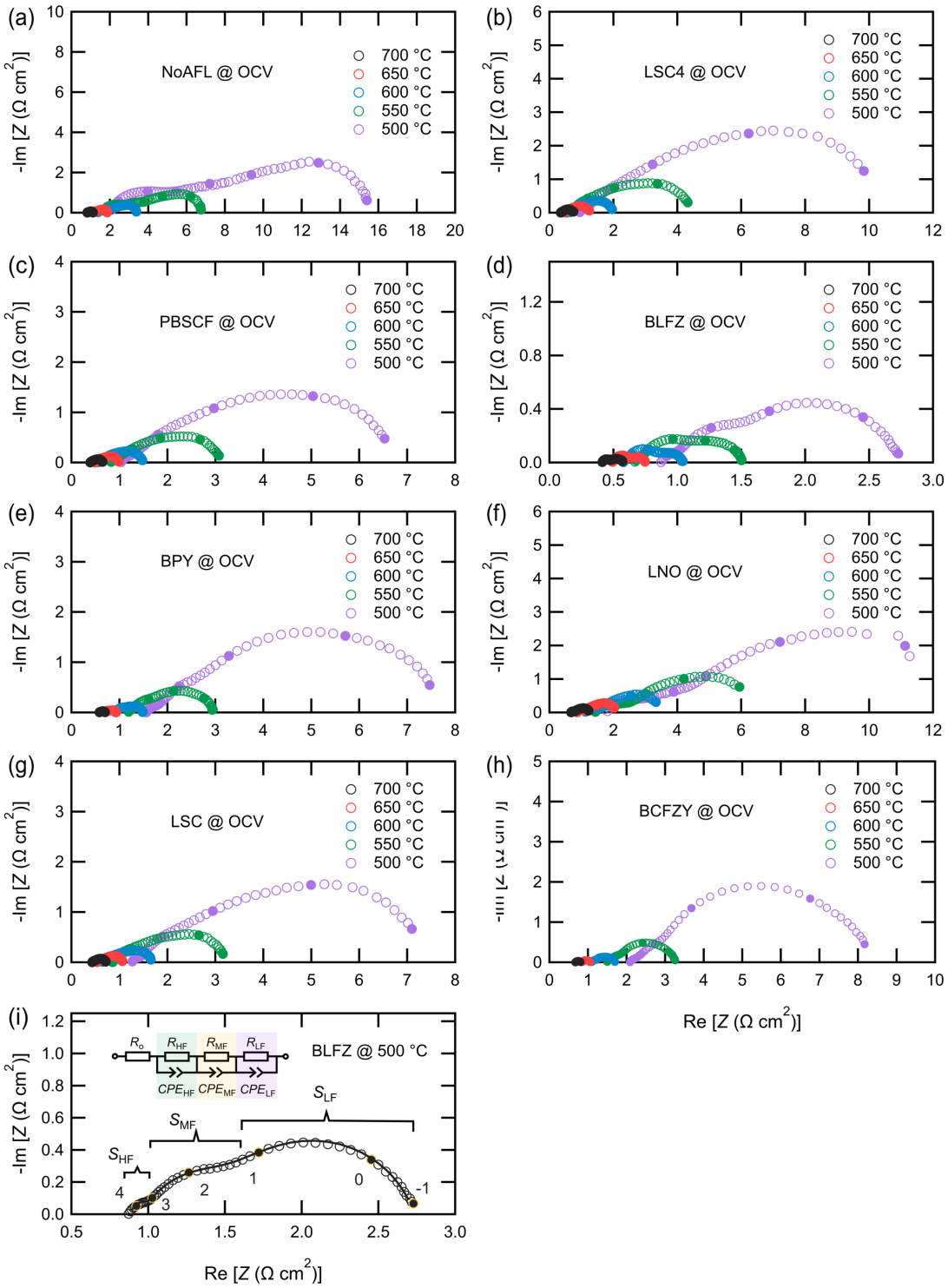

Figure 4-13 Electrochemical impedance spectra (EIS) of P-SOECs with various AFLs ranging from 700 °C to 500 °C under OCV condition. (a) NoAFL. (b) LSC4. (c) PBSCF. (d) BLFZ. (e) BPY. (f) LNO. (g) LSC. (h) BCFZY. (i) EIS of BLFZ AFL cell at 500 °C, circles are observed data and solid line is fitting result with equivalent circuit model of R_o–(R_{HF}–CPE$_{HF}$)–(R_{MF}–CPE$_{MF}$)–(R_{LF}–CPE$_{LF}$)

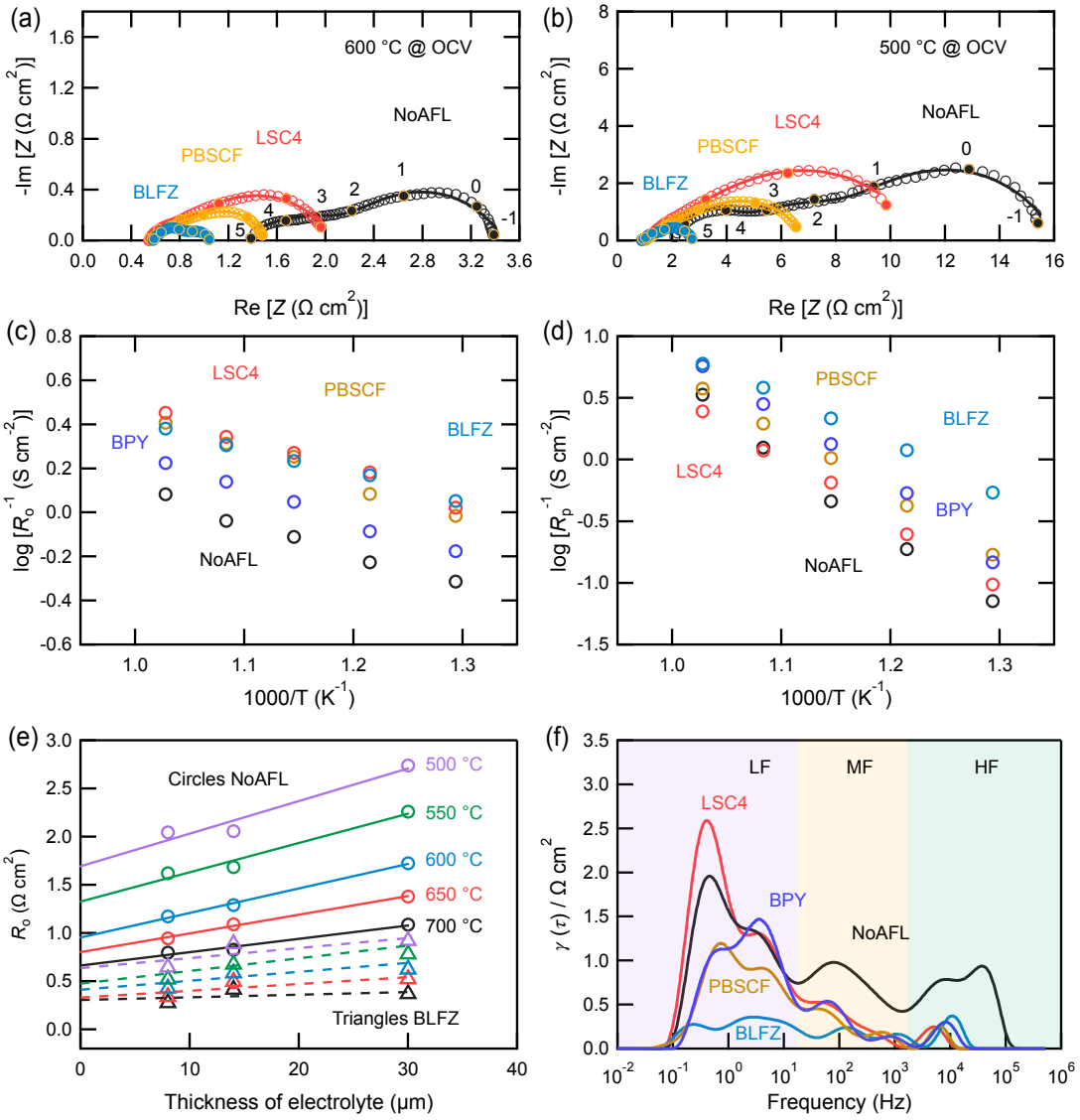

Figure 4-14 Electrochemical impedance spectra of P-SOECs. (a)-(b) Nyquist plots obtained by EIS at 600 and 500 °C, respectively, under open-circuit voltage (OCV) conditions. Circles represent the observed data and solid lines are fitting results with the equivalent circuit. Arrhenius plots of (c) ohmic resistance (R_o) and (d) anodic polarization resistance (R_p), as determined by equivalent circuit analysis using EIS. (e) R_o for the cells with different electrolyte thicknesses. (f) Distribution of relaxation time (DRT) analysis of NoAFL, LSC4, PBSCF, BLFZ and BPY cell at 500 °C.

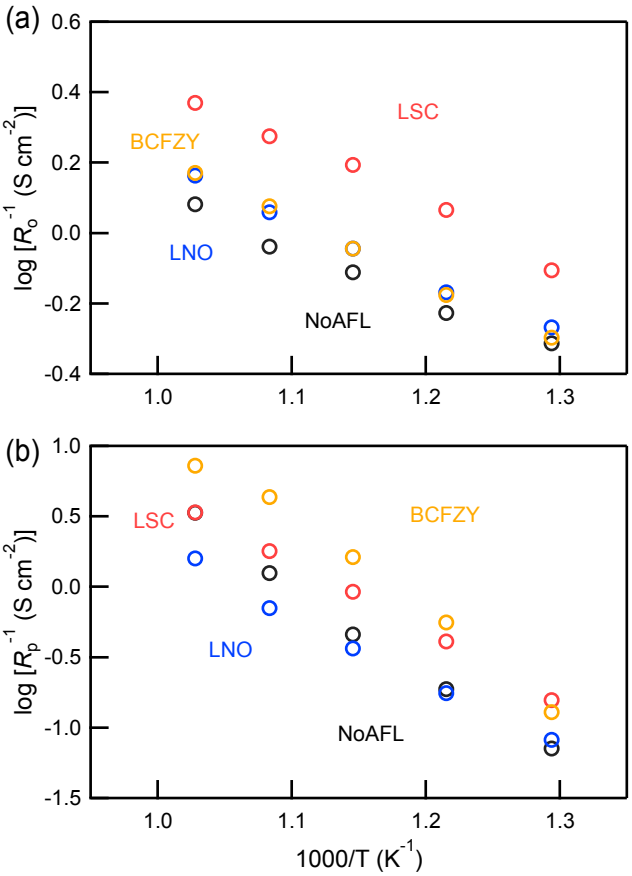

Figure 4-15 Arrhenius plots of (a) ohmic resistance (R_o) and (b) anodic polarization resistance (R_p) as determined by equivalent circuit analysis using EIS for NoAFL, LNO, LSC and BCFZY cell.

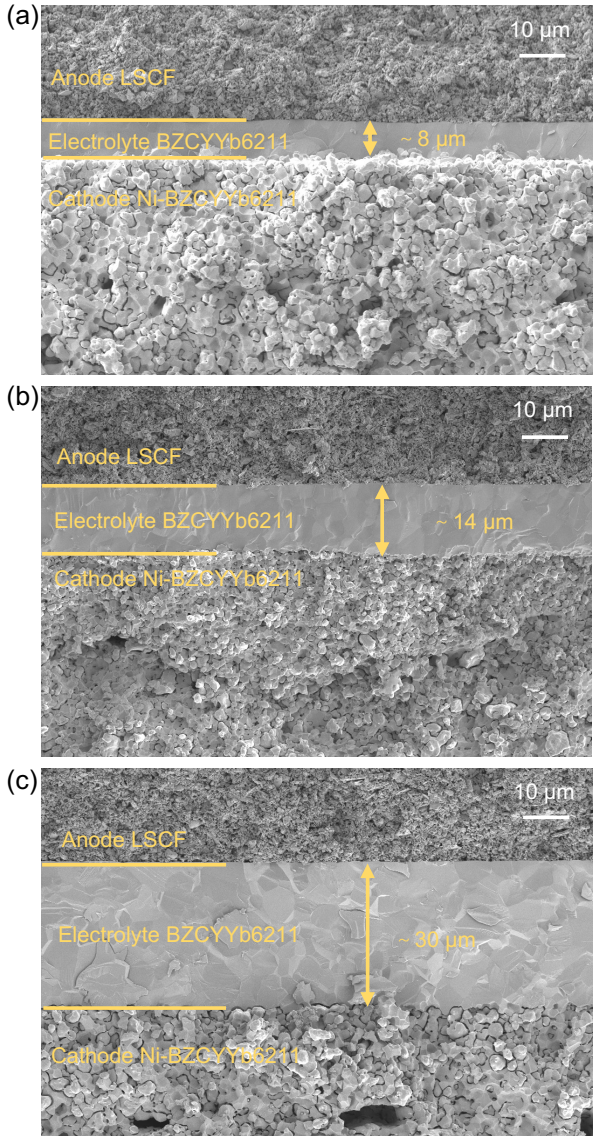

Figure 4-16 Cross-sectional SEM images of NoAFL cells with different thicknesses of BZCYYb6211 electrolyte.

Table 4-1 Comparison of activation energies of ohmic resistance (R_o) and anodic polarization resistance (R_p) for P-SOECs without and with different AFLs.

Anode functional layer (AFL)	Activation energy for R_o	Activation energy for R_p
NoAFL	0.29	1.24
LSC4	0.31	1.04
PBSCF	0.32	1.01
BLFZ	0.24	0.78
BPY	0.31	1.17
LNO	0.32	0.95
LSC	0.35	0.99
BCFZY	0.36	1.32

4.3.5 Anode reaction resistances

Recent studies have successfully employed a combination of reaction order analysis and DRT analysis of EIS to validate the sluggish elementary step in the air electrode reaction on protonic solid oxide cells (P-SOCs). An elementary reaction model was proposed for the anodic reaction on P-SOECs, as shown in Table 4-2.[33–36] In this, the steam dissociative adsorption coupled with proton migration preferentially takes place at the gas-anode-electrolyte TPB (step 1–3), following which multiple charge transfers with the surface diffusion of oxygen species occur on the LSCF anode (step 5–7), together with interfacial proton transfer (step 4); finally associative oxygen desorption (step 8). The BLFZ cell may use the gas-anode-AFL TPB. The reaction orders in terms of steam and oxygen partial pressures, denoted as m and n, respectively, for each elementary step are listed in Table 1, and are calculated by representing the rate equations of every elementary step as a function of p_{H2O}^{-m} and p_{O2}^{-n} through a simple kinetic treatment.[33,34] The polarization resistance related to the step (i) tends to be proportional to p_{H2O}^{-mi} and p_{O2}^{-ni}, so that DRT peaks can be identified through their p_{H2O} and p_{O2} dependencies. Among steps 1-8 in Table 4-2, the resistance related to step 4, that is, interfacial proton transfer resistance, could be assigned to $R_o(0)$, as mentioned

above.

The impedance responses of NoAFL and BLFZ cells were evaluated under various p_{O2} values in the anode side at 500 °C under the OCV (Figure 4-17). The DRT responses to p_{O2} are displayed in Figure 4-18 for NoAFL cells. Five peaks appear at approximately 10^5, 10^4, 10^2, 10^0, and 10^{-1} Hz, which are marked as P1, P2, P3, P4, and P5, respectively; the corresponding resistances were calculated from the peak area, as shown in Figure 4-18b. P3, P4 and P5 apparently respond to p_{O2} with n = 0.15, 0.25 and 0.17, so that these can attribute to step 6–8. P4 and P5 of BLFZ AFL cells are clearly assigned to the charge transfer to O adsorbs (step 7) and the associative desorption (step 8), respectively, as mentioned below. Therefore, P4 and P5 of NoAFL cell could also assign to step 7 and 8, respectively, although the corresponding n value does not perfectly coincide with the ideal one. Hence, P3 that is the largest resistances of fives is assigned to the diffusion of O adsorbs (step 6). This agrees with the previous reports that LSCF anode exhibit large resistances related to oxygen surface diffusion in the frequency region of about 10^2 Hz.[37,38] P1 exhibits negligible dependence on p_{O2}, which is consistent with the feature of step 1–4. Zhou et al reported that P-SOEC exhibits relatively large resistance in a frequency higher than 500 Hz, which might be associated with charge transfer reaction on LSCF-electrolyte interfaces.[38,39] Based on these, P1 should be assigned to the first charger transfer at the TPB. P2 is smaller than P3 by 40% and is not assigned precisely, here.

BLFZ cell also has five peaks (P1-P5) as well as NoAFL cells, but the resistances decrease in the entire frequency region by one order of magnitude with the application of the BLFZ AFL (Figure 4-18c and d). The P5 at 10^{-1} Hz has a large p_{O2} dependence (n = 0.72) and thus can be assigned to step 8. Because P4 of the BLFZ cell has a n = 0.35, which is close to the ideal value of step 7 (n = 3/8), it can be assigned to the second charge transfer step 7. P3 was not sensitive to p_{O2} and the value is only 8% of that of NoAFL cells. These features indicate that the resistances related to surface diffusion are not dominant in BLFZ AFL cell. The P1 of the BLFZ cell is not sensitive to p_{O2}, indicating that the peak is assigned to step 5 as is the case with NoAFL. These results of DRT analysis clarify the distinguishing features of the anode reaction on BLFZ AFL:

1) the resistances related to the charge transfer and associative desorption of oxygen, are much lower than those of NoAFL cell, and 2) the anode reaction proceeds without large overpotential for surface oxygen diffusion over LSCF. Compared to other AFL materials, only BLFZ AFL cell remarkably decrease P4 and P5, i.e., the resistances of step-7 and 8, respectively in LF region. This must be related to the expand of proton accessible reaction areas near AFL-gas-electrolyte TPB due to the excellent proton conductivity in BLFZ, as mentioned below.

Table 4-2 Elementary steps for the anode reaction of P-SOECs and related reaction orders in terms of steam and oxygen partial pressures, which are denoted as *m* and *n*, respectively.

Steps	Reactions	*m*	*n*
Step 1	$H_2O(g) \longrightarrow H_2O$ (TPB)	1	0
Step 2	H_2O (TPB) $\longrightarrow OH^-$(TPB) + H^+(TPB)	1	0
Step 3	OH^-(TPB) $\longrightarrow O^{2-}$(TPB) + H^+(TPB)	1/2	0
Step 4	H^+ (TPB) $\longrightarrow H^+$ (ele)	1/2	0
Step 5	O^{2-} (TPB) + $h^+ \longrightarrow O^-$(TPB)	0	0
Step 6	O^- (TPB) $\longrightarrow O^-$ (an)	0	1/4
Step 7	O^- (an) + $h^+ \longrightarrow$ O (an)	0	3/8
Step 8	2O (an) $\longrightarrow O_2$ (g)	0	1

"an," "TPB," and "ele" indicate species on LSCF anode surfaces, the gas-anode-electrolyte triple-phase boundary and BZCYYb6211 electrolyte, respectively. For AFL cells, "TPB" is replaced to the gas-anode-AFL triple-phase boundary.

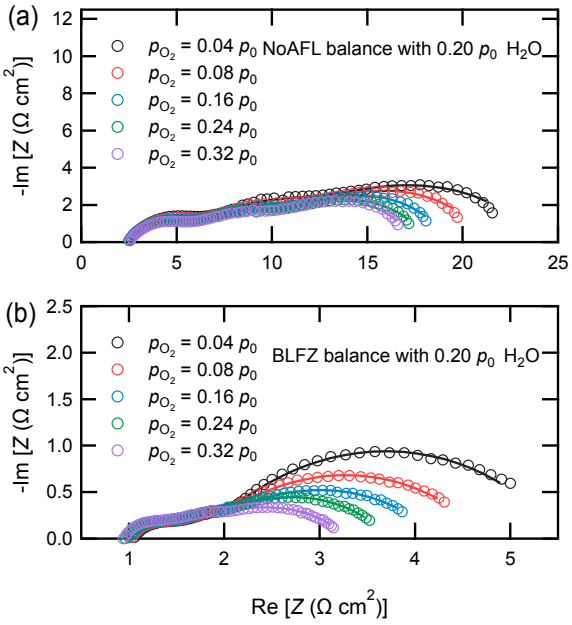

Figure 4-17 EIS of P-SOECs measured at 500 °C of (a) NoAFL and (b) BLFZ AFL cells as a function of oxygen partial pressures (p_{O2}).

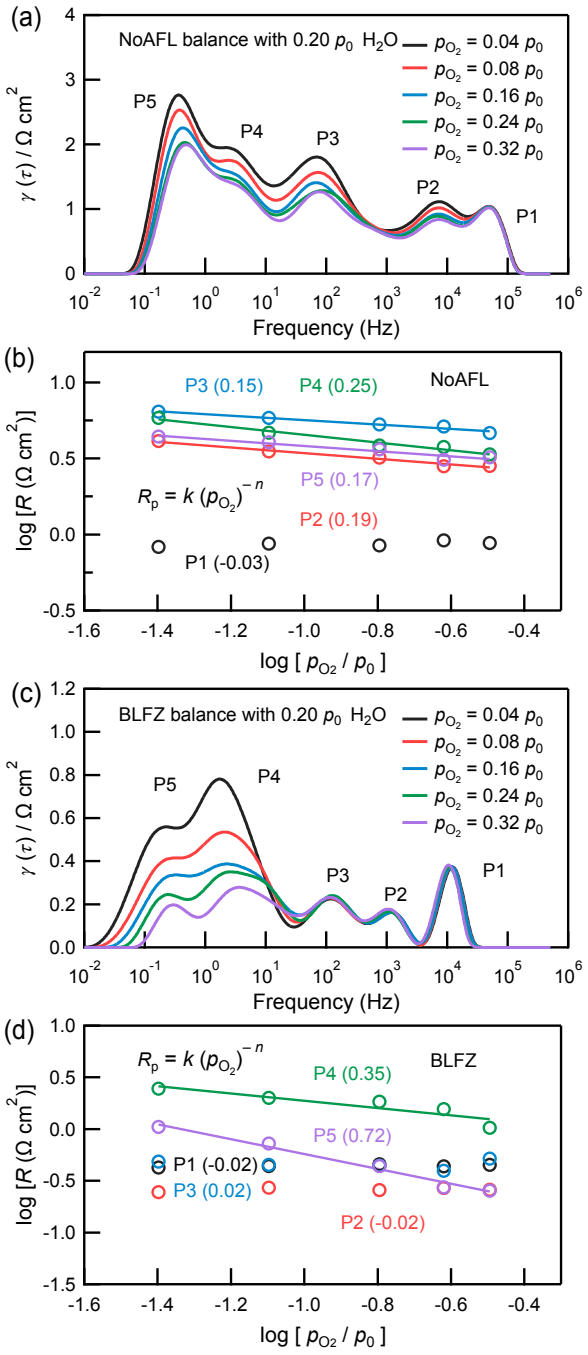

Figure 4-18 DRT plots for the impedance spectra of the (a) NoAFL and (c) BLFZ AFL cells at 500 °C as a function of oxygen partial pressures (p_{O2}). p_{O2} dependences of resistances related to DRT peaks P1–P5 for (b) NoAFL and (d) BLFZ cells.

4.4 Discussion

4.4.1 Improvement of Faradaic efficiency

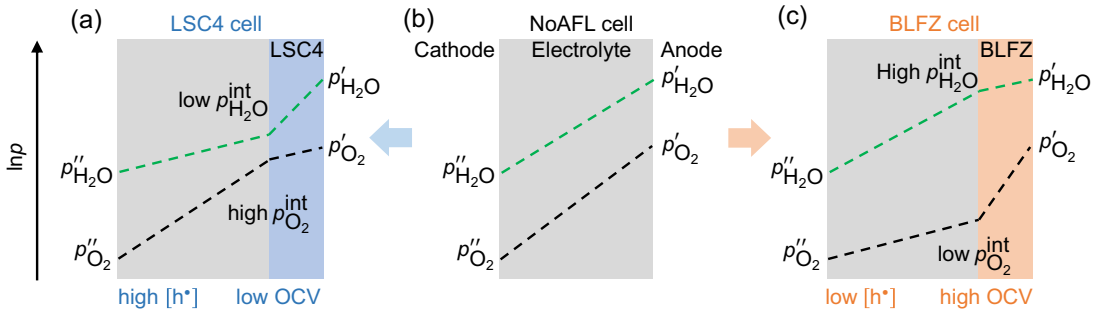

Figure 4-19 Oxygen and water chemical potentials across electrolyte and AFL for (a) LSC4 cell, (b) NoAFL cell and (c) BLFZ cell.

The OCV of NoAFL is varied with expressed by Equation (4-3) due to the mixed conductivity.[40,41]

$$\begin{aligned} \mathrm{OCV} &= t_{\mathrm{o}}E_{\mathrm{o}} + t_{\mathrm{H}}E_{\mathrm{H}} \\ &= t_{\mathrm{o}}\frac{RT}{4F}\ln\left(\frac{p'_{\mathrm{O_2}}}{p''_{\mathrm{O_2}}}\right) + t_{\mathrm{H}}\frac{RT}{2F}\ln\left(\frac{p''_{\mathrm{H_2O}}}{p'_{\mathrm{H_2O}}}\right)\left(\frac{p'^{\,1/2}_{\mathrm{O_2}}}{p''^{\,1/2}_{\mathrm{O_2}}}\right) \end{aligned} \tag{4-3}$$

Here, E_{o} and E_{H} are the thermodynamic OCV values of oxygen and hydrogen concentration cells, respectively, and t_{o} and t_{H} are the transport numbers of oxide ions and protons for BZCYYb6211. $p'_{\mathrm{O_2}}$ and $p'_{\mathrm{H_2O}}$ are oxygen and water partial pressures in the anode gases, respectively. $p''_{\mathrm{O_2}}$ and $p''_{\mathrm{H_2O}}$ are oxygen and water partial pressures in the cathode gases, respectively. OCV of AFL cell is given by similar equation with replacing $p'_{\mathrm{O_2}}$ and $p'_{\mathrm{H_2O}}$ to $p^{\mathrm{int}}_{\mathrm{O_2}}$ and $p^{\mathrm{int}}_{\mathrm{H_2O}}$, respectively, which are p_{O2} and p_{H2O} at AFL/electrolyte interface, respectively. OCV of P-SOECs becomes lower than the ideal value since sum of t_{o} and t_{H} is lower than unity by the partial conductivity of hole carriers formed by Equation (4-4). The hole carrier concentration $\mathrm{h}^{\bullet}$ near the anode/electrolyte interface is greatly influenced by p_{O2} and p_{H2O} at the TPB as follows:[12]

$$[h^{\bullet}] = K_{hyd}^{-1/2} K_{ox}^{1/2} [OH_O^{\bullet}] p_{H_2O}^{-1/2} p_{O_2}^{1/4}$$
$$= K_{hyd}^{-1/2} K_{ox}^{1/2} \exp\left(\frac{F(E - E^0)}{RT}\right) \quad (4\text{-}4)$$

Here, E, E^0, F, R, and T are the redox potential, standard potential, Faraday's constant, gas constant, and temperature, respectively. K_{hyd} and K_{ox} are equilibrium constant of hydration and oxidation reaction (Equation (4-1) and (4-2)), respectively. Equation (4-4) proves that $[h^{\bullet}]$ decreases with increasing p_{H2O} and decreasing p_{O2}.

Figure 4-19 represents schematically the oxygen and water chemical potential terms, i.e., $\ln p_{O2}$ and $\ln p_{H2}$, respectively across electrolyte and AFL. p_{O2} and p_{H2} at both edges are fixed by the value of the anode and cathode gases. The gradients of $\ln p_{O2}$ and $\ln p_{H2O}$ provide the driving forces of oxide ion and proton, respectively, assuming that a constant electrical field is applied in both electrolyte and AFL.

In NoAFL cell, both $\ln p_{O2}$ and $\ln p_{H2O}$ should decrease linearly with going from the anode to the cathode side across electrolyte, respectively, because the fluxes of oxide ions and protons remain constant throughout electrolyte (Figure 4-19b).[42] LSC4 AFL must require large drop of $\ln p_{H2O}$ across the layer to yield the equivalent proton flux as one of BZCYYb electrolyte, owing to the relatively low proton conductivity (Figure 4-19a). It may not, however, involve large drop of $\ln p_{O2}$ due to certain oxide ion conductivity. Hence, $p_{H_2O}^{int}$ and $p_{O_2}^{int}$ of LSC4 AFL cell become relatively low and high, respectively, in comparison to NoAFL cell, which are favourable to form $[h^{\bullet}]$ according to Equation (4-4). Thereby LSC4 cells show low OCV.

BLFZ AFL must need only small drop of $\ln p_{H2O}$ for the sufficient proton flux due to the excellent proton conductivity, which results in relatively high $p_{H_2O}^{int}$ (Figure 4-19c). BLFZ is also expected to involve relatively low $p_{O_2}^{int}$ with relatively large $\ln p_{O2}$ drop because ferrite perovskite $LaFeO_3$ (9×10^{-13} cm^2 s^{-1}) has much smaller oxygen diffusivity than cobaltite $LaCoO_3$ (6×10^{-10} cm^2 s^{-1}).[43] These features favour lowering $[h^{\bullet}]$ in comparison to NoAFL cell, and thus BLFZ AFL cell gives rise to high OCV.

Tuning of $p_{O_2}^{int}$ and $p_{H_2O}^{int}$ as depicted in Figure 4-19 also fits to the changes of

Faradaic efficiencies (η) with AFL. BLFZ AFL develops relatively low of $p_{O_2}^{int}$ and high $p_{H_2O}^{int}$ at the AFL/electrolyte interface by combing high proton and low oxide ion conductivities, which depresses hole carries at the interface. The η of the BLFZ cell is about 75% at 214 mA cm^{-2}, which is nearly two times higher than those of cells with O^{2-}/e^- double-conducting anode materials, including LSM,[30,31] BSCF,[29] SEFC,[44] and SLF[45]. Poorly proton-conducting AFLs, such as LSC4, cause the large drop of $\ln p_{H2O}$ across the layer and thus retain relatively low $p_{H_2O}^{int}$, resulting in increase of $[h^{\bullet}]$ and decrease of η.

4.4.2 Reaction model at gas-anode-AFL TPB

The anode reaction model for the gas–anode–AFL TPB is proposed based on the different polarization behaviors of the NoAFL and BLFZ cells, as shown in Figure 4-20. Since LSCF is an O^{2-}/e^- double conductor, the dissociative adsorption of water dominantly occurs at the TPB, as shown in Figure 4-20a (red zone). NoAFL cell possesses large interfacial protonic resistances, i.e. $R_o(0)$, which is corresponding to 80% of ohmic resistance (Figure 4-14e). Such interfacial contributions must be caused by poor electrical contact, because limited TPB areas between LSCF and BZCYYb6211 narrow proton-accessible electrode area, as shown in Figure 4-20a (red zone). BLFZ AFL drastically improved the electrical contact with decreasing $R_o(0)$ by 60%, because the triple conductivity of the BLFZ AFL can extend proton-accessible electrode areas near TPB (Figure 4-20b, red zone).

Impedance analysis revealed that the NoAFL cell caused high R_p owing to the sluggish diffusion, charge transfer and desorption of O species over LSCF (Figure 4-20a). The effective reaction zones near the TPB are generally proportional to the term D/k, where D is the diffusion constant of the anode reaction intermediates, and k is the surface exchange kinetics determined by the desorption and charge transfer steps.[46,47] Hence, NoAFL cell requires a long distant diffusion for oxygen species (step 6) from the TPB to the LSCF anode to extend the TPB length, thereby resulting in high resistances for diffusion (Figure 4-18a). BLFZ AFL cells have significantly extended

reaction areas near TPB, so that they do not need to extend the reaction areas with surface diffusion, if *k* of BLFZ is larger than LSCF. In fact, the BLFZ AFL exhibits lower resistances for charge transfer to oxygen species and associative oxygen desorption than other AFLs, which confirms that the BLFZ AFL has a significantly large *k*. It is concluded that the BLFZ AFL can facilitate the anode reactions without remarkable diffusion of O adsorbs due to its high proton conductivity and excellent kinetics for associative desorption and charge transfer with water molecules.

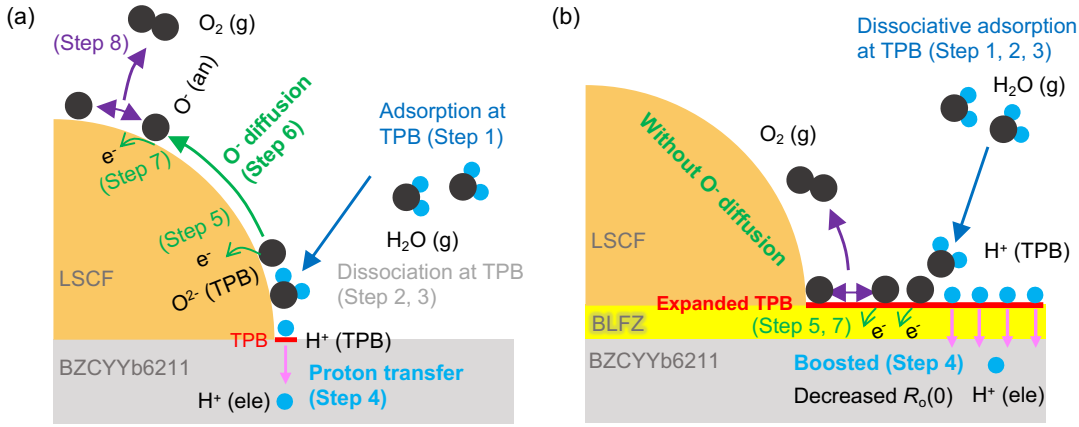

Figure 4-20 Schematic of proposed anodic reaction mechanism of P-SOECs. (a) NoAFL cell. (b) BLFZ AFL cell.

4.5 Conclusion

In this chapter, modification of the anode/electrolyte interface by BLFZ AFL was demonstrated to be a promising strategy to obtain P-SOECs with a high electrochemical performance and hydrogen production. The NoAFL cell offered effective reaction zones for electrochemical water adsorption and proton transfer in the vicinity of the gas-electrolyte-anode TPB, necessitating diffusion of oxygen adsorbs to extend the reaction area for electrochemical associative desorption. The BLFZ AFL provided relatively large proton-accessible electrode areas due to the $H^+/O^{2-}/e^-$ triple conductivity, and thus involved very small interfacial protonic resistances. The extended reaction areas over BLFZ cell enables the anode reactions without aids of enhanced oxygen diffusions, and thus the cells exhibit much lower polarization resistances than those of NoAFL cells. The polarization resistances of BLFZ AFL cells are much lower than those of the cells with other triple-conducting and double-conducting AFLs, which confirms that BLFZ is very active for the various electrochemical steps of anode reactions. Moreover, the BFLZ AFL depresses hole carriers in BZCYYb6211 electrolyte because it retains relatively high p_{H2O} and low p_{O2} at the interface owing to the relatively high proton conductivity but low oxide ion conductivity. Hence the implementation of BLFZ AFL can simultaneously improve the current density and Faradaic efficiency of P-SOECs. The design of optimum AFLs offers a strong tool to simultaneously improve the electrolysis performance and energy conversion efficiency of P-SOECs.

4.6 References

1. L. Bi, S. Boulfrad and E. Traversa, *Chem. Soc. Rev.*, 2014, **43**, 8255–8270.
2. H. Iwahara, H. Uchida, K. Ono and K. Ogaki, *J. Electrochem. Soc.*, 1988, **135**, 529–533.
3. K. D. Kreuer, *Annu. Rev. Mater. Res.*, 2003, **33**, 333–359.
4. C. Duan, R. Kee, H. Zhu, N. Sullivan, L. Zhu, L. Bian, D. Jennings and R. O'Hayre, *Nat. Energy*, 2019, **4**, 230–240.
5. H. Ding, W. Wu, C. Jiang, Y. Ding, W. Bian, B. Hu, P. Singh, C. J. Orme, L. Wang, Y. Zhang and D. Ding, *Nat. Commun.*, 2020, **11**, 1–11.
6. J. A. Wrubel, J. Gifford, Z. Ma, H. Ding, D. Ding and T. Zhu, *Int. J. Hydrogen Energy*, 2021, **46**, 11511–11522.
7. W. Wu, H. Ding, Y. Zhang, Y. Ding, P. Katiyar, P. K. Majumdar, T. He and D. Ding, *Adv. Sci.*, 2018, **5**, 1800360.
8. S. Choi, T. C. Davenport and S. M. Haile, *Energy Environ. Sci.*, 2019, **12**, 206–215.
9. R. Murphy, Y. Zhou, L. Zhang, L. Soule, W. Zhang, Y. Chen and M. Liu, *Adv. Funct. Mater.*, 2020, **30**, 2002265.
10. J. Kim, A. Jun, O. Gwon, S. Yoo, M. Liu, J. Shin, T.-H. Lim and G. Kim, *Nano Energy*, 2018, **44**, 121–126.
11. Y. Zhou, E. Liu, Y. Chen, Y. Liu, L. Zhang, W. Zhang, Z. Luo, N. Kane, B. Zhao, L. Soule, Y. Niu, Y. Ding, H. Ding, D. Ding and M. Liu, *ACS Energy Lett.*, 2021, **6**, 1511–1520.
12. E. Vøllestad, R. Strandbakke, M. Tarach, D. Catalan-Martinez, M. L. Fontaine, D. Beeaff, D. R. Clark, J. M. Serra and T. Norby, *Nat. Mater.*, 2019, **18**, 752–759.
13. F. Meng, C. Sun, J. Shi, H. Zhang, B. Xu and Y. Ding, *Int. J. Hydrogen Energy*, 2019, **44**, 1122–1129.
14. S. U. Rehman, A. Shaur, R.-H. Song, T.-H. Lim, J.-E. Hong, S.-J. Park and S.-B. Lee, *J. Power Sources*, 2019, **429**, 97–104.
15. A. Egger, E. Bucher, M. Yang and W. Sitte, *Solid State Ionics*, 2012, **225**, 55–60.
16. F. Li, L. Jiang, R. Zeng, F. Wang, Y. Xu and Y. Huang, *Int. J. Hydrogen Energy*, 2017, **42**, 29463–29471.
17. Y. Meng, J. Gao, H. Huang, M. Zou, J. Duffy, J. Tong and K. S. Brinkman, *J. Power Sources* **2019**, 439, 227093.
18. C. Duan, J. Tong, M. Shang, S. Nikodemski, M. Sanders, S. Ricote, A. Almansoori and R. O'Hayre, *Science* **2015**, 349, 1321–1326.
19. S. J. Stokes and M. S. Islam, *J. Mater. Chem.* **2010**, 20, 6258–6264.
20. R. Zohourian, R. Merkle, G. Raimondi and J. Maier, *Adv. Funct. Mater.* **2018**, 28. 1801241.

21. Z. Wang, P. Lv, L. Yang, R. Guan, J. Jiang, F. Jin and T. He, *Ceram. Int.* **2020**, 46, 18216–18223.
22. S. D. Ebbesen, S. H. Jensen, A. Hauch and M. B. Mogensen, *Chem. Rev.* **2014**, 114, 10697–10734.
23. N. Wang, H. Toriumi, Y. Sato, C. Tang, T. Nakamura, K. Amezawa, S. Kitano, H. Habazaki and Y. Aoki, *ACS Appl. Energy Mater.* **2021**, 4, 554–563.
24. T. Matsuura, J. Tabuchi, J. Mizusaki, S. Yamauchi and K. Fueki, *J. Phys. Chem. Solids* **1988**, 49, 1403–1408.
25. M. Al Daroukh, *Solid State Ionics*, **2003**, 158, 141–150.
26. S. Choi, C. J. Kucharczyk, Y. Liang, X. Zhang, I. Takeuchi, H.-I. Ji and S. M. Haile, *Nat. Energy* **2018**, 3, 202–210.
27. J. Lagaeva, D. Medvedev and A. Demin, P. Tsiakaras, *J. Power Sources* **2015**, 278, 436–444.
28. D. Han, X. Liu, T. S. Bjørheim and T. Uda, *Adv. Energy Mater.* **2021**, 11, 2003149.
29. S. Li and K. Xie, *J. Electrochem. Soc.* **2013**, 160, F224–F233.
30. S. Li, R. Yan, G. Wu, K. Xie and J. Cheng, *Int. J. Hydrogen Energy* **2013**, 38, 14943–14951.
31. H. Li, X. Chen, S. Chen, Y. Wu and K. Xie, *Int. J. Hydrogen Energy* **2015**, 40, 7920–7931.
32. K. D. Kreuer, S. Adams, W.Münch, A. Fuchs, U. Klock and J. Maier, *Solid State Ionics*, **2001**, 145, 295–306.
33. T. H. Wan, M. Saccoccio, C. Chen and F. Ciucci, *Electrochim. Acta* **2015**, 184, 483–499.
34. F. He, T. Wu, R. Peng and C. Xia, *J. Power Sources*, **2009**, 194, 263.
35. T. Kobayashi, K. Kuroda, S. Jeong, H. Kwon, C. Zhu, H. Habazaki and Y. Aoki, *J. Electrochem. Soc.* **2018**, 165, F342–F349.
36. H. Toriumi, T. Kobayashi, S. Hinokuma, T. Ina, T. Nakamura, K. Amezawa, C. Zhu, H. Habazaki and Y. Aoki, *Inorg. Chem. Front.* **2019**, 6, 1587–1597.
37. 1 J. H. Park, C. H. Jung, K. J. Kim, D. Kim, H. R. Shin, J. E. Hong and K. T. Lee, *ACS Appl. Mater. Interfaces*, 2021, **13**, 2496–2506.
38. Y. Zhou, W. Zhang, N. Kane, Z. Luo, K. Pei, K. Sasaki, Y. Choi, Y. Chen, D. Ding and M. Liu, *Adv. Funct. Mater.*, 2021, **31**, 2105386.
39. Y. Chen, Y. Choi, S. Yoo, Y. Ding, R. Yan, K. Pei, C. Qu, L. Zhang, I. Chang, B. Zhao, Y. Zhang, H. Chen, Y. Chen, C. Yang, B. deGlee R. Murphy, J. Liu and M. Liu, *Joule*, 2018, **2**, 938–949.
40. J. Lyagaeva, N. Danilov, G. Vdovin, J. Bu, D. Medvedev, A. Demin and P. Tsiakaras, *J. Mate. Chem. A*, 2016, **4**, 15390–15399.
41. L. Lei, J. Zhang, Z. Yuan, J. Liu, M. Ni and F. Chen, *Adv. Funct. Materials*, 2019, **29**, 1903805.

42. S. Jeong, T. Yamaguchi, M. Okamoto, C. Zhu, H. Habazaki, M. Nagayama and Y. Aoki, ACS Appl. Energy Mater., 2020, 3, 1222−1234.
43. T. Ishigaki, S. Yamauchi, K. Kishio, J. Mizusaki and K. Fueki, *J. Solid State Chem.*, 1988, **73**, 179–187.
44. D. Huan, N. Shi, L. Zhang, W. Tan, Y. Xie, W. Wang, C. Xia, R. Peng and Y. Lu, *ACS Appl. Mater. Interfaces* **2018**, 10, 1761–1770.
45. D. Huan, W. Wang, Y. Xie, N. Shi, Y. Wan, C. Xia, R. Peng and Y. Lu, *J. Mater. Chem. A* **2018**, 6, 18508–18517.
46. Z. Gao, L. V. Mogni, E. C. Miller, J. G. Railsback and S. A. Barnett, *Energy Environ. Sci.* 2016, **9**, 1602–1644.
47. K. Yakal-Kremski, L. V. Mogni, A. Montenegro-Hernández, A. Caneiro and S. A. Barnett, *J. Electrochem. Soc.* 2014, **161**, F1366–F1374.

Chapter 5 High performance of $Ba_{0.95}La_{0.05}Fe_{0.8}Zn_{0.2}O_{3-\delta}$ anode functional layer with efficient $PrBa_{0.5}Sr_{0.5}Co_{1.5}Fe_{0.5}O_{5+\delta}$ anode for protonic solid oxide electrolysis cells

5.1 Objective of chapter 5

As described in chapter 1.5.1, there exists three kind of anode materials for P-SOECs. O^{2-}/e^- double conductors, composites of O^{2-}/e^- double conductor and proton-conducting electrolyte, and single-phase $H^+/O^{2-}/e^-$ triple conductors. Single-phase $H^+/O^{2-}/e^-$ triple conductors are most promising candidates among the three since they allow using not only TPB but also whole anode particle surface for the anode reaction.

In chapter 4, a series of double- or triple-conducting oxides were examined as AFL, and $Ba_{0.95}La_{0.05}Fe_{0.8}Zn_{0.2}O_{3-\delta}$ (BLFZ) was found to improve simultaneously both cell conductivity and Faradic efficiency. However, the cells tested in chapter 4 using LSCF anode, which is typical double conductor and thus is not desirable anode material. Among various $H^+/O^{2-}/e^-$ triple conducting anode materials, $PrBa_{0.5}Sr_{0.5}Co_{2-x}Fe_xO_{5+\delta}$ (PBSCF) has been recognized as favorable anode for P-SOECs. BLFZ is also $H^+/O^{2-}/e^-$ triple conductor, but the implementation to P-SOECs anode has not been examined. In this chapter, the improvement of P-SOECs with BLFZ AFL was carried out through the optimization of AFL thickness and choice of anode material. The cells with BLFZ anode were confirmed to possess deteriorated performance compared to the cells with PBSCF anode. The best performance in P-SOECs with Zr-rich side electrolyte could be achieved by combination of 150 nm-thick BLFZ AFL and PBSCF anode, and the corresponding cell exhibits current of 1.12 A cm^{-2} at 1.3V with very low anodic reaction resistance of 0.10 Ω cm^2 at 600 °C.

5.2 Experimental section

5.2.1 Material synthesis

PBSCF and BLFZ powders were synthesized by a citrate precursor route as described in chapter 4.2.1.

5.2.2 Fabrication of half-cell and AFL

Half-cells based on BZCYYb6211 electrolyte were prepared by the same procedures in chapter 4.2.2. The thin BLFZ AFL was also grown on the BZCYYb6211 electrolyte layer surface via PLD, and the thickness of BLFZ film was control by different deposition time under an energy of 102 mJ $pulse^{-1}$, a repetition rate of 5 Hz and an oxygen pressure of 21 Pa at 700 °C.

5.2.3 Characterization

XRD and SEM were used to check the phase purity and microstructure of PBSCF and BLFZ powder, and cross-sectional images of cell.

In this chapter, two kind of anode slurries were prepared. In the first case, as prepared PBSCF or BLFZ powders were simply dispersed into a solution containing a binder (5 wt% surfactant dissolved in α-terpineol) and dispersant (20 wt% polyethyleneimine (*M*w 28 000) dissolved in α-terpineol) by ball milling for 3 h with a weight ratio of powder (PBSCF or BLFZ):dispersant:binder = 10:3:1. In the second case, PBSCF and BLFZ were ball milled for 24 h in ethanol. After drying, the powders together with dispersant and binder were ball milled for 10 h to obtain the second kind of anode slurry. Finally, the slurry was screen-printed on the BZCYYb6211 electrolyte or BLFZ AFL as the anode for the measurement of P-SOECs as described in chapter 3.2.4.

5.3 Results and discussion

5.3.1 Characterization of PBSCF and BLFZ

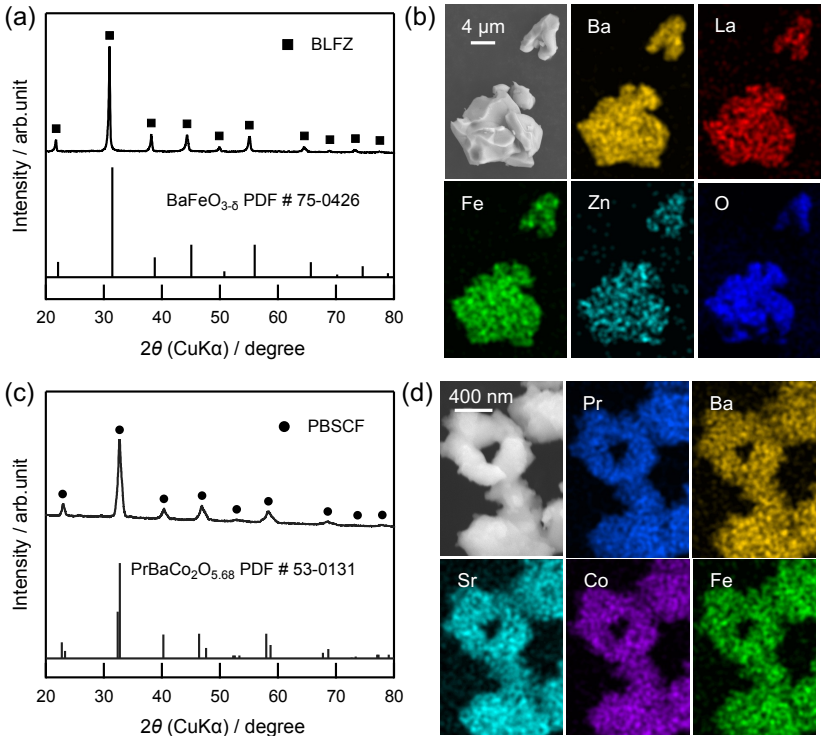

Figure 5-1 Phase and microstructure characterization of BLFZ and PBSCF. (a) and (c) XRD patterns of BLFZ and PBSCF powders. (b) and (d) EDX element mapping of BLFZ and PBSCF particles.

The BLFZ and PBSCF powders were confirmed by XRD, as shown in Figure 5-1a and c. All diffraction peaks of BLFZ and PBSCF are well-matched with cubic $BaFeO_{3-\delta}$ (PDF-75-0426) and tetragonal $PrBaCo_2O_{5.68}$ (PDF-53-0131) perovskite structures, respectively. SEM and the related EDX mapping (Figure 5-1b) indicate that BLFZ has particle sizes of approximately several micrometers and the distribution of metal atoms is highly homogenous. PBSCF particles are much smaller than that of BLFZ with the particle sizes equaling a few hundred nanometers (Figure 5-1d). The large particle size of BLFZ must be attributed to the grain growth, assisted by liquid phase formation of ZnO and BaO mixed phase, such as $BaZnO_2$.[1]

BLFZ was introduced to the interface between BZCYYb6211 electrolyte and PBSCF anode to optimize the thickness of AFL. Figure 5-2a show the typical cross-sectional

SEM image of P-SOEC with porous PBSCF anode. Fives cells were fabricated with BLFZ AFL of 0, 30, 90, 150 and 170 nm thickness, as shown by Figure 5-2b, which are called BLFZ-0, 30, 90, 150 and 170, respectively, based on the thickness. The microstructures of cell with 150 nm thick BLFZ were investigated in detail by high-resolution transmission electron microscopy (HRTEM). The lattice fringes (Figure 5-2c) with interplanar spacing of 0.40 and 0.29 nm are well agreement with the (110) and (100) crystal planes, respectively (PDF-75-0426). The EDX mapping analysis of Fe (Figure 5-2c) confirms a sharp interface was reserved between BLFZ AFL and BZCYYb6211 electrolyte. Hereafter, the cells have different BLFZ AFL thicknesses.

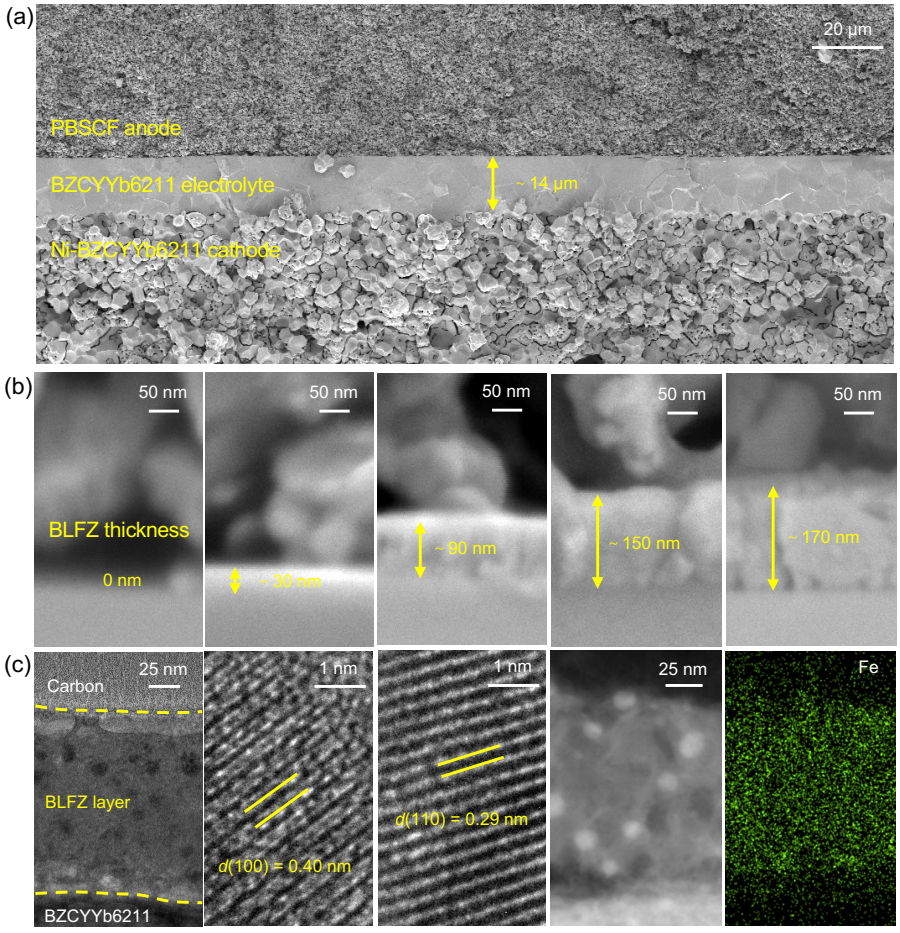

Figure 5-2 (a) Typical cross-sectional SEM image of P-SOECs. (b) P-SOECs with different thickness of BLFZ anode functional layer. (c) Lattice fringes and EDX mapping (Fe) of BLFZ anode functional layer.

5.3.2 Performance and Faradaic efficiency of P-SOECs

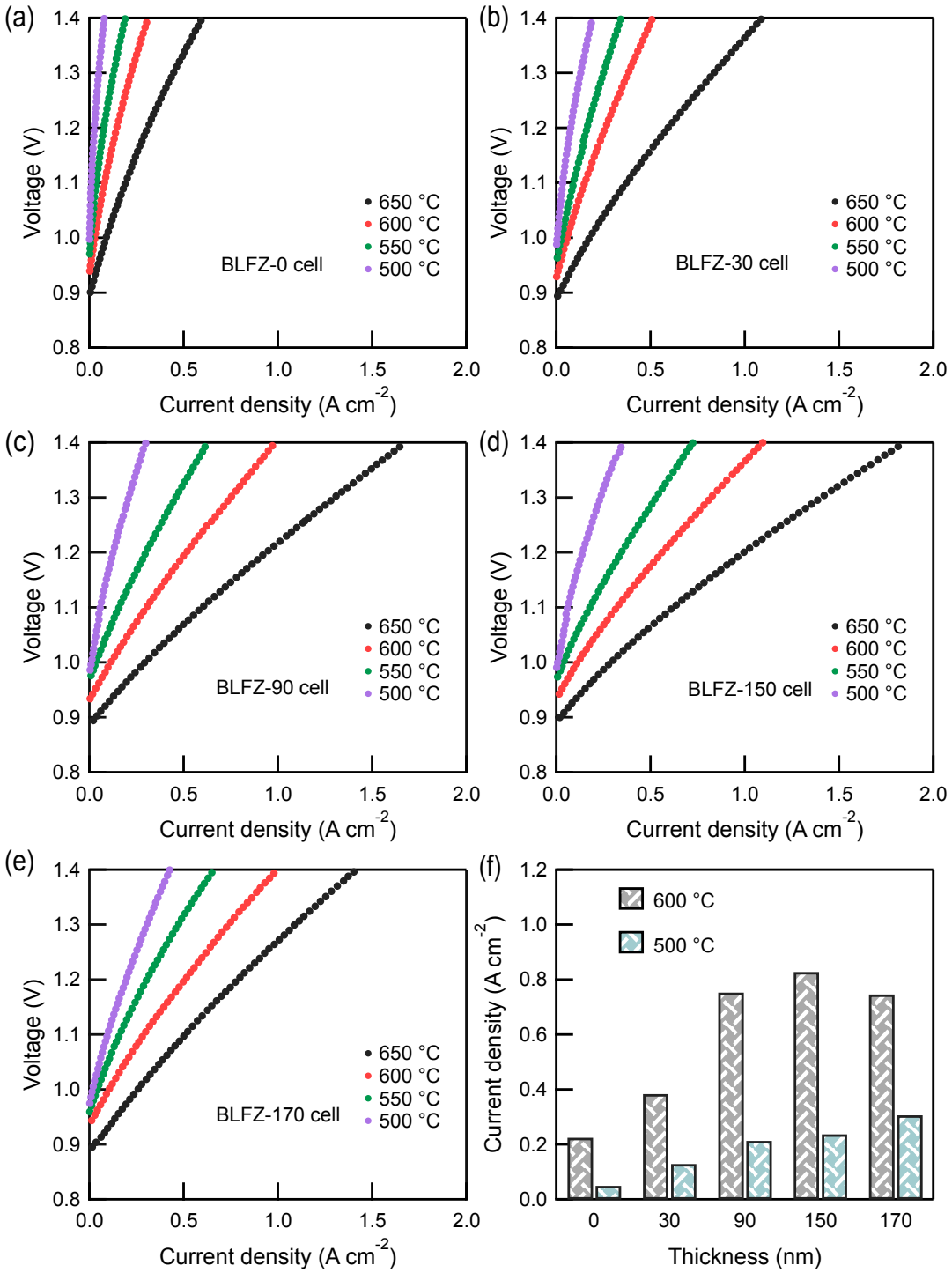

Figure 5-3 Current-voltage (*I-V*) curves of P-SOECs with various thicknesses of BLFZ layer. (a) BLFZ-0, (b) BLFZ-30, (c) BLFZ-90, (d) BLFZ-150, and (e) BLFZ-170 cell. (f) Electrolysis current density in 1.3 V at 600 and 500 °C.

The current-voltage (*I-V*) curves (Figure 5-3) of P-SOECs as a function of BLFZ AFL thickness were recorded by supplying a 30%-H_2O/air gaseous mixture to the PBSCF anode and humidified 10%H_2/Ar to the Ni-BZCYYb6211 cathode, respectively. The open circuit voltage (OCV) of cell without BLFZ AFL, that is BLFZ-0 cell, is 0.94 and 1.00 V at 600 and 500 °C, respectively, which is higher than the values of the cells using LSCF anode (see chapter 4.3). This means the PBSCF anode more efficiently suppress the hole injection into the electrolyte than LSCF. The current densities of BLFZ-0 under 1.3 V bias at 650, 600, 550 and 500 °C are 0.45, 0.23, 0.13 and 0.05 A cm^{-2}, respectively, as shown in Figure 5-3a. All cells with BLFZ AFL show similar OCV as BLFZ-0 cell (same with the highest data in chapter 4.3). The *I-V* curves of cells (Figure 5-3b-e) with BLFZ AFL exhibit higher current densities than the bare cell (BLFZ-0 cell) at each measured temperature. The electrolysis currents at 1.3 V and 600 °C are enhanced to 0.38, 0.75, and 0.83 A cm^{-2}, respectively, for BLFZ-30, -90 and -150 cells, which are higher than the corresponding value (0.23 A cm^{-2}) of BLFZ-0 cell by 65%, 226% and 261%, respectively (Figure 5-3f). However, when the BLFZ AFL thickness is further increased to 170 nm, the current density is slightly deteriorated to 0.75 A cm^{-2} (Figure 5-3e and f), indicating the optimal thickness of BLFZ thin film is around 150 nm.

Figure 5-4 shows the hydrogen evolution rates of BLFZ-0, -90 and -150 cells under galvanostatic electrolysis with corresponding applied currents at 600 and 500 °C measured by gas chromatography. All cells were maintained for 3 h of galvanostatic electrolysis at each fixed current, and in every cell, the hydrogen production rate could be in equilibrium after approximately 1 h. Hence, the average hydrogen evolution rate was determined by data of the following 2 h. BLFZ-0 cell has an average hydrogen evolution rate of 50, 70, 100 and 120 μmol min^{-1} cm^{-2} (Figure 5-4a) at the applied currents of 0.24, 0.34, 0.46 and 0.57 A cm^{-2}, respectively, from which the Faradaic efficiency is calculated to be 69%, 67%, 68% and 67%, respectively (Figure 5-4d). In the case of BLFZ-90 cell, the average hydrogen evolution rates are 140, 180, 210 and 240 μmol min^{-1} cm^{-2} (Figure 5-4b) at currents of 0.70, 0.90, 1.10 and 1.30 A cm^{-2} and the efficiencies are 65, 65, 62 and 58%, respectively (Figure 5-4d). BLFZ-150 cell

shows average hydrogen evolution rates of 170, 180, 210 and 230 μmol min^{-1} cm^{-2} under 0.74, 0.92, 1.10 and 1.40 A cm^{-2} (Figure 5-4c) with efficiencies of 71, 62, 59 and 51% respectively (Figure 5-4d). At thermal neutral potential, i.e., 1.3 V, the hydrogen evolution rates of BLFZ-90 and -150 cells are almost 2 times higher than that of BLFZ-0 cell with keeping Faradaic efficiency about 70%, indicating the increment of the current (Figure 5-3) is coming from enhancement of electrochemical reaction rates by BLFZ AFL and is not caused by the hole leakage.

Figure 5-4e and f are hydrogen evolution rates under galvanostatic electrolysis condition at 500 °C for BLFZ-0 and -150 cells. Here, the constant currents were set so as to apply the bias about 1.3 V. The average hydrogen evolution rate of BLFZ-0 cell is only 10 μmol min^{-1} cm^{-2} (Figure 5-4e) at a current of 0.05 A cm^{-2}, and the efficiency is 67%. BLFZ-150 cell exhibits the evolution rate of 55 μmol min^{-1} cm^{-2} with an efficiency of 82% (Figure 5-4d), which is the highest value in this thesis at the same conditions. The electrolysis current and Faradaic efficiency of BLFZ-150 cell using PBSCF anode are much larger than both BLFZ-0 cell with PBSCF anode and BLFZ-140 cell with LSCF anode (chapter 4), confirming the synergy effects of BLFZ AFL and PBSCF triple conducting anode.

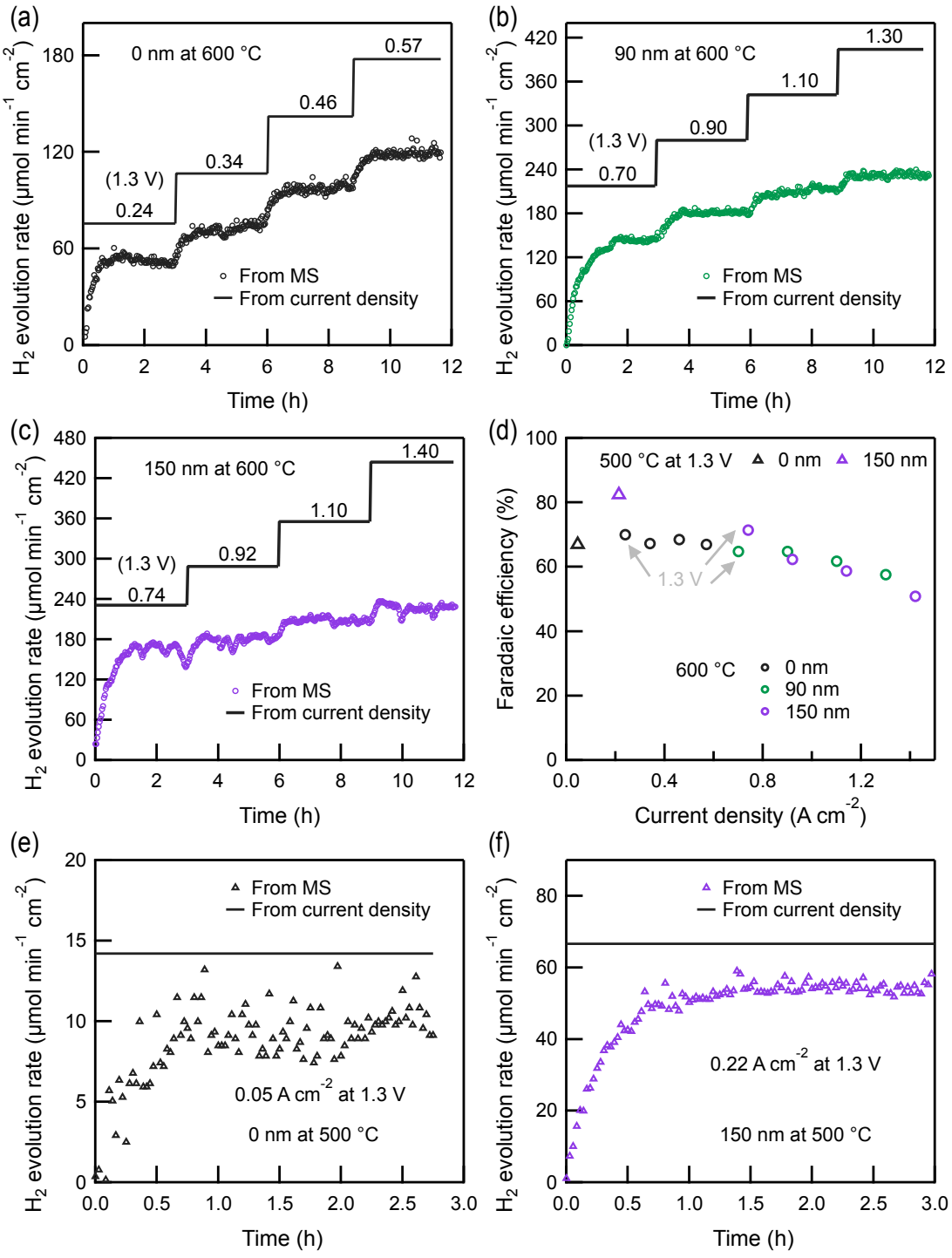

Figure 5-4 Hydrogen evolution rates under galvanostatic electrolysis condition at 600 °C. (a) BLFZ-0 cell with applied currents of 0.24, 0.34, 0.46 and 0.57 A cm^{-2}. (b) BLFZ-90 cell at 0.70, 0.90, 1.10 and 1.30 A cm^{-2}. (c) BLFZ-150 cell at 0.74, 0.92, 1.14 and 1.42 A cm^{-2}. Black lines depict the theoretical hydrogen evolution rates at corresponding current and circles show the real-time detected hydrogen evolution rates. (d) Calculated average Faradaic efficiency from hydrogen evolution rate. Hydrogen

evolution rates of (e) BLFZ-0 and (f) -150 cells under galvanostatic electrolysis condition at 500 °C. The currents are 0.05 and 0.22 A cm^{-2} for BLFZ-0 and -150 cell, respectively, in both of which the applied bias is around 1.3 V.

5.3.3 Electrochemical impedance spectroscopy

Electrochemical impedance spectra (EIS) were recorded from 650 to 500 °C in the frequency range of 10^{6}–10^{-1} Hz with an alternating current (AC) amplitude of 30 mV under open circuit voltage (OCV) conditions and different direct current (DC) potentials as displayed in Figure 5-5 and 5-6. The Nyquist impedance plots of all cells have the *x*-intercept at high frequency region, which corresponds to the ohmic resistance (R_o) from BZCYYb6211 electrolyte and the polarization resistance (R_p) with two distinct semicircles from anodic reaction, respectively. Therefore, the equivalent circuit analysis as described in chapter 3.3.3 and chapter 4.3.4 was conducted to obtain R_p values (Figure 5-5d).

Figure 5-5a and b show the EIS of BLFZ-0, -30, -90, -150 and -170 cells measured under OCV conditions at 600 and 500 °C, respectively. BLFZ-0 cell has R_o of 1.67 and 3.17 Ω cm^2 at 600 and 500 °C, respectively. The relatively large R_o is assigned to the interfacial contact resistances as demonstrated in chapter 4.3.4 (Figure 4-14e). R_o decreases by increasing thickness of BLFZ AFL and the values for 30 nm, 90 nm, 150 nm, and 170 nm thickness equal to 1.01, 0.61, 0.55 and 0.52 Ω cm^2 at 600 °C, respectively, and 1.65, 1.15, 0.95 and 0.74 Ω cm^2 at 500 °C, respectively (Figure 5-5a-c). This feature indicates that BLFZ AFL has significant proton conductivity so as to enhance the proton transfer from reaction sites to electrolyte. The activation energies of R_o (Figure 5-5e) clearly decreases with the thickness of AFL and the values as calculated from the Arrhenius plots of R_o^{-1} (Figure 5-5c) are 0.38, 0.38, 0.40, 0.32 and 0.23 eV for BLFZ-0, 30, 90, 150 and 170 cells, respectively. This result verifies that the interfacial proton migration controls the overall ohmic resistances, and moreover, confirms that the proton transfer barrier at the interface is lowered by the BLFZ AFL.

Similarly, the R_p decreases with thickness of AFL. R_p of BLFZ-0 cell is 1.30 Ω cm^2

at 600 °C, and decreases to 0.46, 0.20, 0.22 and 0.18 Ω cm^2, respectively by 65, 85, 83 and 86% reduction, respectively, with increasing thickness of BLFZ from 30 to 90 to 150 to 170 nm, respectively (Figure 5-5d). At 500 °C, the corresponding R_p values of BLFZ-30, 90, 150 and 170 cells are 2.79, 1.38, 1.13, and 1.08 Ω cm^2, respectively (Figure 5-5b and d). The Arrhenius plots of R_p^{-1} (Figure 5-5d) clearly demonstrates the activation energy gradually decreases from 1.28 to 1.16 to 1.06 to 0.93 to 0.98 eV with increasing thickness from 0 to 30 to 90 to150 to 170 nm, as shown in Figure 5-5e. R_p of BLFZ-150 cell is much smaller than those of BLFZ-0 cells (1.30 and 2.18 Ω cm^2 at 600 °C for PBSCF and LSCF, respectively) with either PBSCF or LSCF anode, confirming that BLFZ AFL plays a crucial role for the anodic reaction on P-SOECs. The R_p of BLFZ-150 cell using PBSCF (0.22 Ω cm^2 at 600 °C) is only 48% of that of BLFZ-140 cell using LSCF anode (0.46 Ω cm^2 at 600 °C, chapter 4.3.4), which verifies the synergy effects of BLFZ AFL with highly active, triple conducting PBSCF.

Impedance spectra of all cells were collected under various cell biases as shown in Figure 5-6 at 500 °C. R_o is slightly decreased with increasing cell biases in all cells, which is probably due to the increment of both proton and hole currents by the modification of proton and hole defect profiles across the electrolyte film at the applied electrochemical potential field.[2,3] Meanwhile, R_p monotonically decreases with increasing cell bias from 50 mV to 200 mV for every cell.

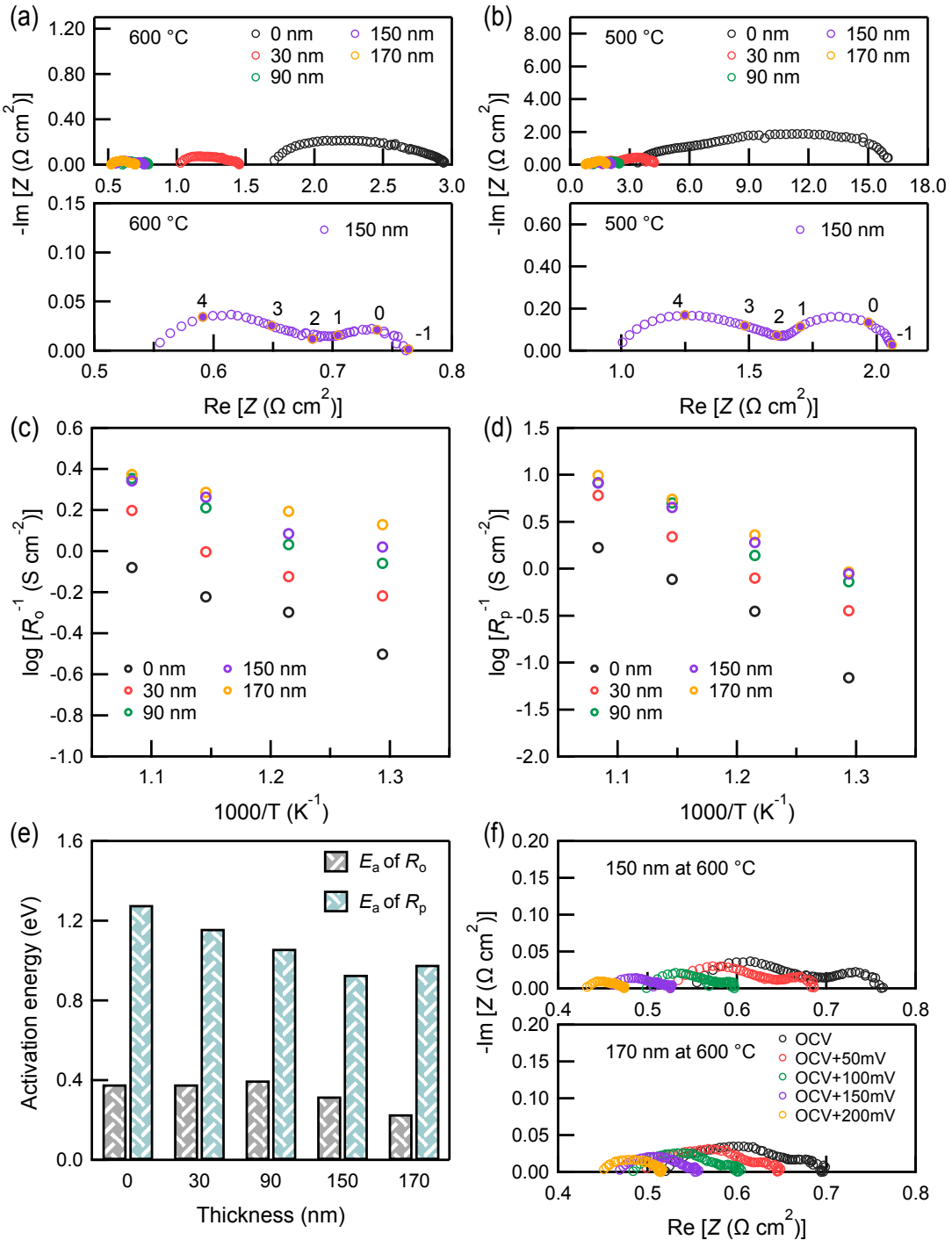

Figure 5-5 Electrochemical impedance spectroscopy (EIS) of P-SOECs as a function of BLFZ AFL thickness. EIS measured at (a) 600 °C, (b) 500 °C under open circuit voltage. Arrhenius plots of (c) ohmic resistance (R_o) and (d) anodic polarization resistance (R_p) as determined by equivalent circuit analysis using EIS. (e) Activation energy for R_o and R_p. (f) Bias-dependence of EIS for BLFZ-150 and 170 cells.

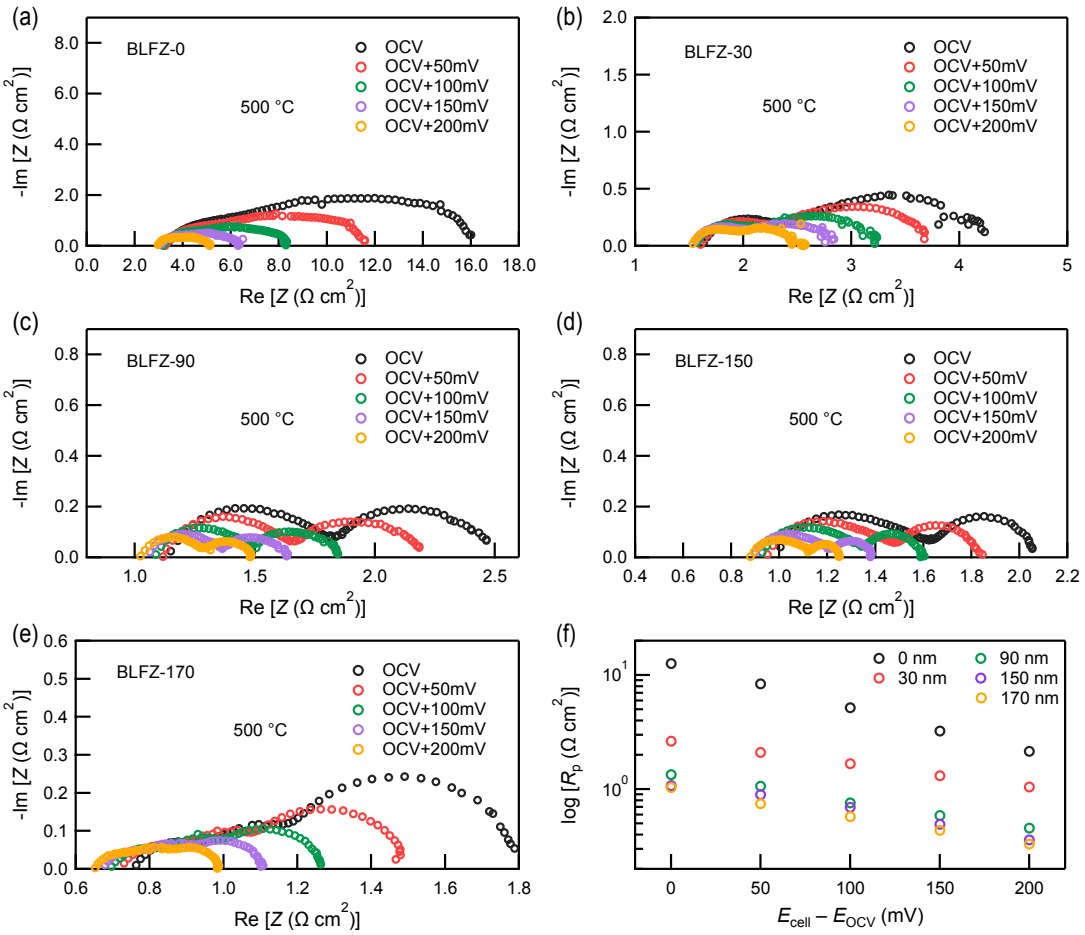

Figure 5-6 Bias-dependence of EIS. Nyquist impedance plots of (a) BLFZ-0 cell, (b) BLFZ-30 cell, (c) BLFZ-90 cell, (d) BLFZ-150 cell and (e) BLFZ-170 cell. (f) R_p of cells at different cell bias values.

5.3.4 Performance of BLFZ anode on P-SOECs

As described in chapter 4.3.2, PBSCF is a $H^+/O^{2-}/e^-$ triple conductor with a hydration enthalpy of approximately 22 kJ mol^{-1} and a proton concentration of 3.5% per formula unit at 200 °C under p_{H2O}/p_0=0.020. BLFZ is, actually, also triple conductor having a higher hydration enthalpy (~ 86 kJ mol^{-1}), thereby higher proton concentration (10% per formula unit at 250 °C under p_{H2O}/p_0=0.016) than PBSCF.[4, 5] Therefore, the results mentioned above stimulate to examine the electrochemical performance of BLFZ as anode on P-SOECs. Unfortunately, the particle sizes of BLFZ are much larger than that of PBSCF, as shown in Figure 5-1. Therefore, BLFZ fine powders were prepared by ball-milling for 24 h in order to reduce the particle sizes and increase the anode surface areas. The BLFZ powders before and after ball-milling are denoted as O-BLFZ (Original BLFZ anode) and BM-BLFZ (Ball-milled BLFZ anode), respectively. O-BLFZ slurry was prepared by ball milling the O-BLFZ powders with a solution containing dispersant and binder for 3 h with (weight ratio of BLFZ:dispersant:binder = 10:3:1). BM-BLFZ slurry was prepared by ball milling the BM-BLFZ powders with the same solution for 10 h, as shown in Figure 5-7. Similarly, O-PBSCF and BM-PBSCF slurries were also prepared from as-received and ball-milled powders, respectively.

Figure 5-7a and b show the XRD patterns of BM-BLFZ and BM-PBSCF powders, respectively. The corresponding insets are expansion of (110) peak for O-BLFZ (black) and BM-BLFZ (red) in 2θ ranging from 29.5 ° to 32.5 °, (102) peak for O-PBSCF (black) and BM-PBSCF (red) at 2θ ranging from 31.5 ° to 34.5 °. Obviously, the peaks are broadened after ball milling in both, indicating the miniaturization of particle sizes by ball milling. O-BLFZ and O-PBSCF are comprised particles with a diameter of several micrometers and hundreds of nanometers, respectively, as confirmed by SEM (Figure 5-7c and d). Simultaneously, the SEM images of BM-BLFZ and BM-PBSCF (Figure 5-7e and f) clearly show the reduction of particle sizes. BM-BLFZ is mixture of several tens nm and a few μm-size particles. BM-PBSCF is more homogeneous, comprising several tens nm-size particles.

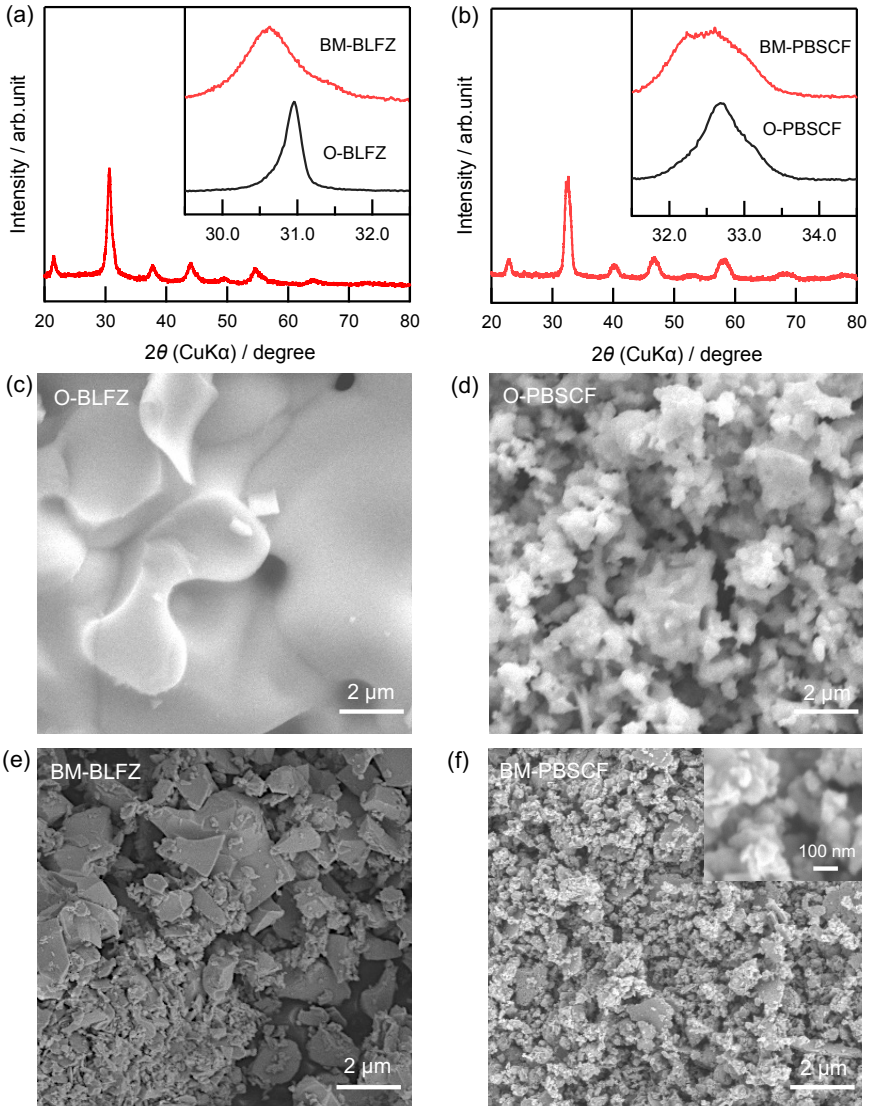

Figure 5-7 (a) XRD of BM-BLFZ. Inset is the expansion of (110) peaks for O-BLFZ and BM-BLFZ. (b) XRD of BM-PBSCF. Inset is the expansion of (102) peaks for O-PBSCF and BM-PBSCF. SEM images of (c) O-BLFZ and (d) O-PBSCF and (e) BM-BLFZ and (f) BM-PBSCF.

The *I-V* curves of P-SOECs based on O-BLFZ, BM-BLFZ and BM-PBSCF anodes are shown in Figure 5-8. BLFZ anode functional layer with a thickness of 150 nm was applied in all cells. O-BLFZ cell yields currents of 0.46, 0.24, 0.16 and 0.10 A cm^{-2} at 650, 600, 550 and 500 °C, respectively, under the thermal neutral potential 1.3 V (Figure 5-8a). BM-BLFZ cell exhibits similar values of 0.47, 0.32, 0.18 and 0.11 A cm^{-2} at corresponding temperatures (Figure 5-8b), which indicates the anodic reactions are not promoted by increasing the surface areas of the BLFZ anodes. The electrolysis currents of BM-BLFZ cell are much lower than the corresponding values of O-PBSCF cells (compared Figure 5-8b and Figure 5-3d) although the particle sizes of the former is similar as one of the later (Figure 5-7d and e). These features confirm that PBSCF is more favorable anode materials for P-SOECs. The electrolysis currents of BM-PBSCF cell at 1.3 V are 1.61, 1.12, 0.70 and 0.44 A cm^{-2} at 650, 600, 550 and 500 °C, respectively, (Figure 5-8c) which are 13, 35, 30 and 83% higher than the corresponding values (1.42, 0.83, 0.54 and 0.24 A cm^{-2}) of O-PBSCF, respectively, indicating the surface areas of PBSCF anodes are important to decrease the anode reaction resistances of P-SOECs particularly at low operating temperatures.

Figure 5-9 shows the hydrogen evolution rates of O-BLFZ cell under galvanostatic electrolysis at 600 °C and fixed current of 0.28 A cm^{-2} (1.3V). The average hydrogen evolution rates is 70 μmol min^{-1} cm^{-2} with a Faradaic efficiency of 79% calculated as described in chapter 3.3.2 and 4.3.3, which is far below that (165 μmol min^{-1} cm^{-2} and 71%) of O-PBSCF (Figure 5-4c).

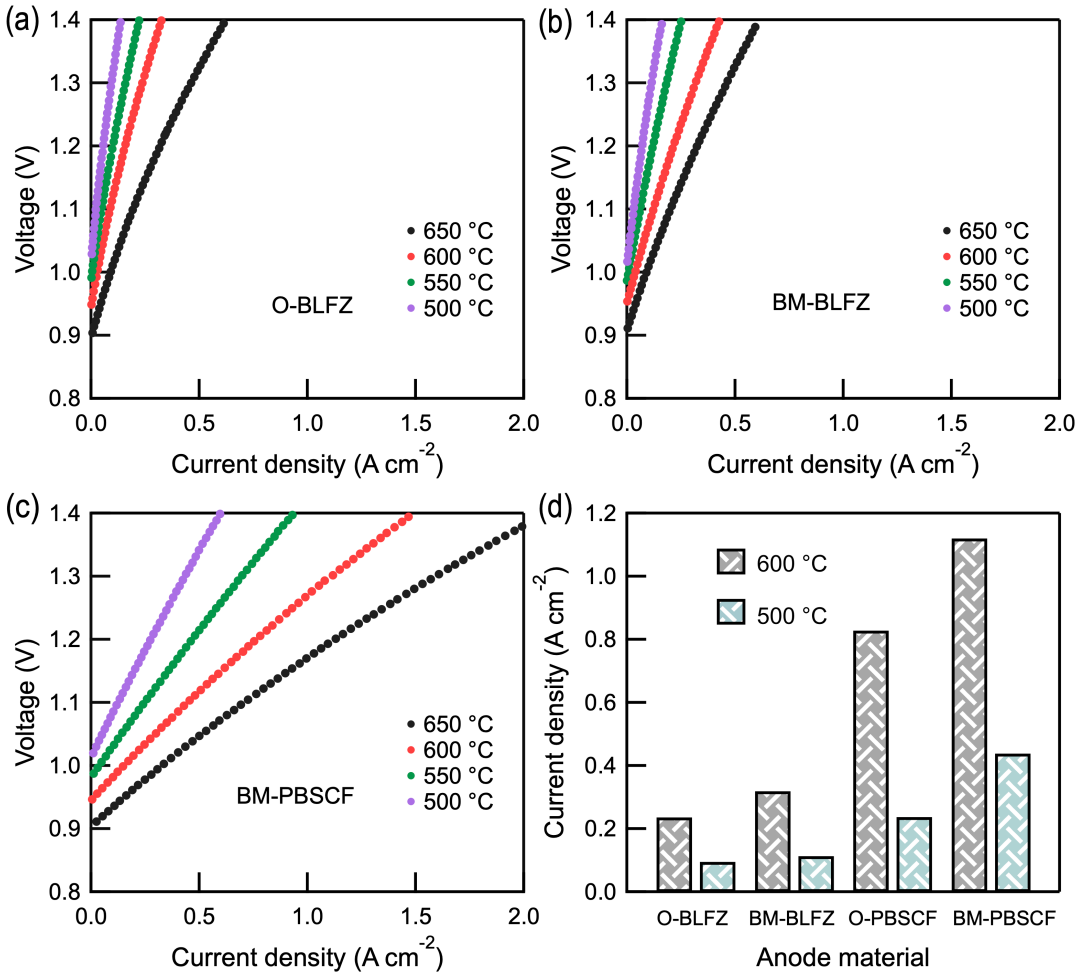

Figure 5-8 Current-voltage (*I-V*) curves of BLFZ-150 cells with anode of (a) O-BLFZ, (b) BM-BLFZ, and (c) BM-PBSCF. (d) Comparison of electrolysis current density at 1.3 V at 600 and 500 °C.

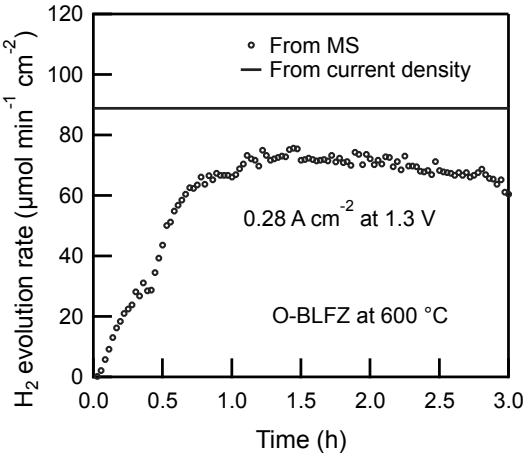

Figure 5-9 Hydrogen evolution rates for BLFZ-150 cell using O-BLFZ anode under galvanostatic electrolysis condition at 600 °C.

The polarization behavior was evaluated by electrochemical impedance spectroscopy (EIS), as shown in Figure 5-10 and 5-11. Figure 5-10a shows the Nyquist plots of O-BLFZ and BM-BLFZ cells at 600 and 500 °C under OCV conditions, which show two distinct semicircles, i.e. the polarization resistance (R_p) related to the anode reaction after the high frequency *x*-intercept corresponding to the ohmic resistance (R_o). The R_o values of BM-BLFZ are 1.11 and 1.68 Ω cm^2 at 600 and 500 °C, respectively, which are 28% and 20% smaller than those (1.54 and 2.10 Ω cm^2) of O-BLFZ. R_p of O-BLFZ cell is 0.79 Ω cm^2 at 600 °C, and it is 54% larger than that of BM-BLFZ (0.36 Ω cm^2) cell. At 500 °C, O-BLFZ and BM-BLFZ cells have R_p of 2.64 and 2.67 Ω cm^2, respectively, implying that the anode reaction resistances are similar each other, which is consistent with the similarity of *I-V* characteristics in both cells (Figure 5-8 a and b). These results indicate the anodic reaction mainly proceeds at the sites on BLFZ AFL, rather than those on BLFZ anode in case of BLFZ-150 cell using BLFZ anode.

In the case of BLFZ-150 cell with BM-PBSCF anode, both R_o and R_p are much lower than the cells with O-PSBCF anode, which is agreement with the *I-V* characteristics as depicted in Figure 5-8c. The R_o and R_p are only 0.32 and 0.10 Ω cm^2, respectively, at 600 °C, and 0.46 and 0.28 Ω cm^2, respectively, at 500 °C under OCV (Figure 5-10b and d). These results reveals that some anodic reaction steps favorably occurs on PBSCF anode surfaces. The R_p of BM-PBSCF cell is much smaller than the R_o at OCV, although R_p of other cells are lower than the corresponding R_o. This feature prove the pronounced anodic reaction activity of BLFZ-150 cell with PBSCF nanoparticle anodes. Figure 5-11 shows the dependance of impedance spectra for O-BLFZ, BM-BLFZ and BM-PBSCF cells under different cell bias at 500 °C. Similar with Figure 5-6, R_p of all cells decrease as increasing the DC potentials from OCV to 200 mV.

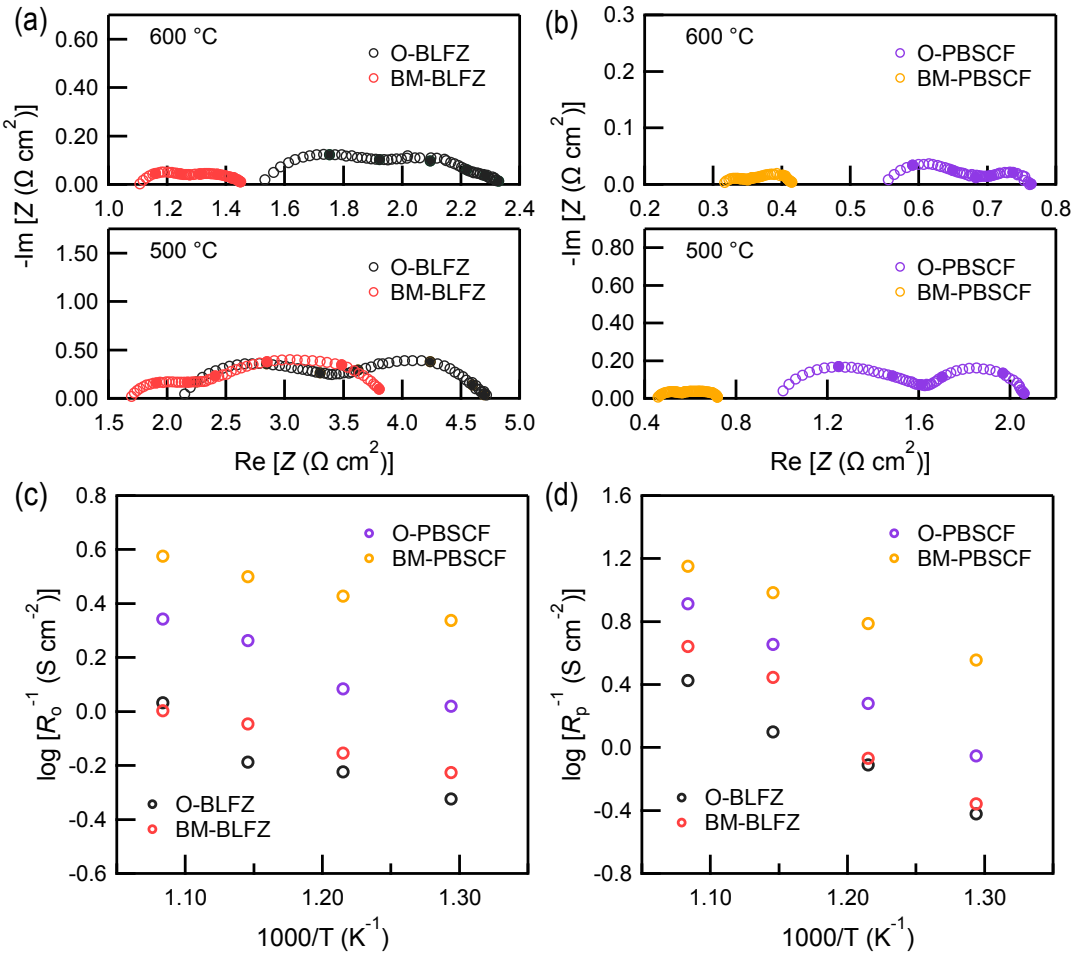

Figure 5-10 Electrochemical impedance spectroscopy (EIS) of P-SOECs. (a) and (b) Nyquist plots obtained by EIS at 600 and 500 °C, respectively, under OCV conditions. Arrhenius plots of (c) ohmic resistance (R_o) and (d) anodic polarization resistance (R_p) as determined by equivalent circuit analysis using EIS.

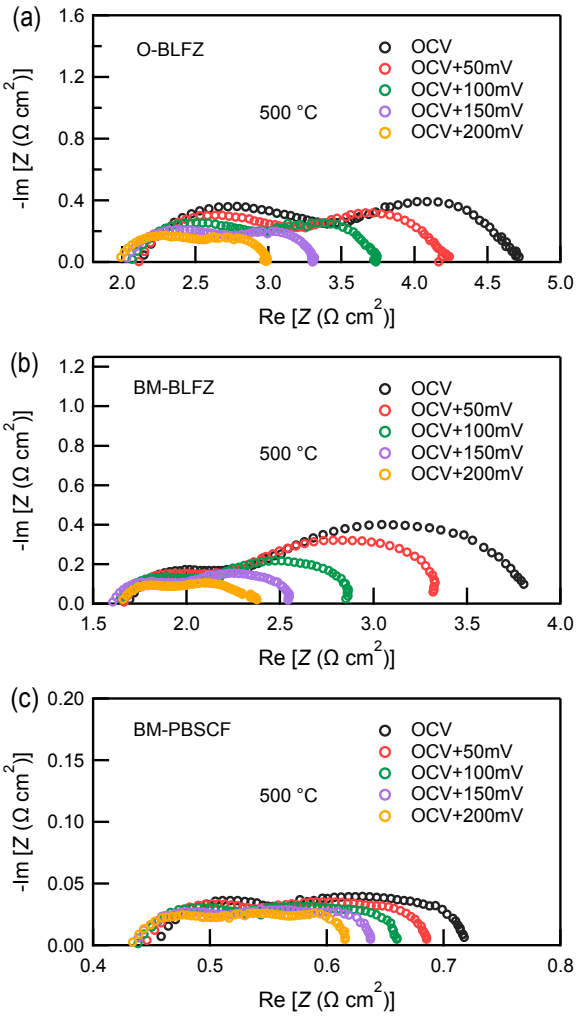

Figure 5-11 Bias-dependence of EIS. Nyquist impedance plots of (a) O-BLFZ cell, (b) BM-BLFZ cell, (c) BM-PBSCF cell.

As demonstrated in chapter 4.3.5, the combination of reaction order analysis and the distribution of relaxation time (DRT) analysis of EIS can validate the sluggish elementary step of the anode reaction in P-SOECs. The impedance responses of BM-PBSCF cells were evaluated under various oxygen partial pressures (p_{O2}) in the anode side at 500 °C under the OCV balanced with a fixed stem partial pressure of (p_{H2O} = 0.30 p_0, p_0 = 101.3 kPa), as displayed in Figure 5-12. Unlike LSCF anode, BLFZ-150 cell using BM-PBSCF anode shows only four DRT peaks at approximately 10^3 (P1), 10^2 (P2), 10^1 (P3) and 10^{-1} (P4) Hz, respectively. The corresponding resistances were calculated from the peak area as shown in Figure 5-12c. Hereafter, the assignment of DRT resistance peaks is conducted with response to p_{O2}^{-n} terms and reaction model listed in Table 4-2. P1 is dependent on p_{O2}^{-n} with n = –0.04 and thus is attributed to the first charger transfer ($O^{2-} + h^+ \longrightarrow O^-$, n = 0). P2 exhibits dependence on p_{O2} (n = 0.38), which is consistent with the feature of the second charger transfer ($O^- + h^+ \longrightarrow O$, n = 0.375). P3 at 10^1 Hz region is also assigned to the second charger transfer as LSCF anode, although the corresponding n value does not perfectly coincide with the ideal one. P4 at 10^{-1} Hz region exhibits very large p_{O2} dependence (n = 0.52), so it should be assigned to associative oxygen desorption ($2O \longrightarrow O_2$ (g)). The largest resistance of P3 means that second charger transfer is rate-controlling step of anodic reaction on BM-PBSCF anode.

Figure 5-13 shows the EIS and DRT plots as a function of p_{H2O} at 500 °C under the OCV with a fixed p_{O2} = 0.20 p_0. As p_{H2O} increasing from 0.03 p_0 to 0.40 p_0, the EIS and DRT plots remain the same, revealing that the partial pressure of steam has little impact on the performance in BM-PBSCF cell.

Here, the DRT plots of LSCF and BM-PBSCF anode-based cells are compared in Figure 5-14. Clearly, the higher current of BM-PBSCF cell is attributed to the significantly decrease of resistance from first, second charger transfer and oxygen desorption, indicating that PBSCF has higher catalytic ability than LSCF and is suitable to use as anode for steam electrolysis.

Finally, the long-term stability of electrolysis cell with BZCYYb6211 electrolyte and BLFZ AFL was examined by galvanostatic electrolysis at 1 and 0.45 A cm^{-2} at 600 and

500 °C, respectively, over 100 h under high humidified condition (Figure 5-15). The cell showed excellent durability.

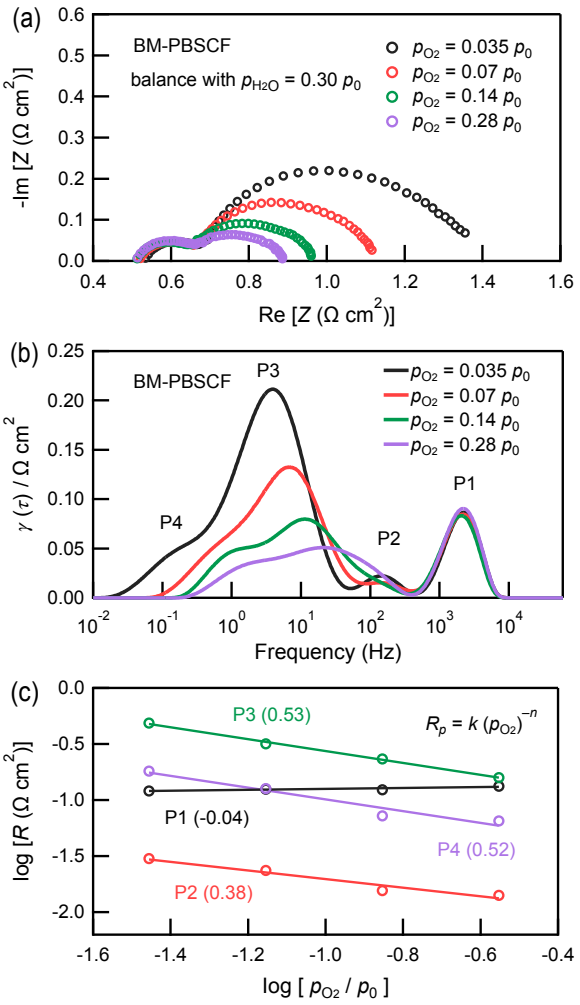

Figure 5-12 EIS and DRT plots of BM-PBSCF cell at 500 °C as a function of oxygen partial pressures (p_{O2}). (a) EIS. (b) DRT plots. (c) p_{O2} dependences of resistances related to DRT peaks P1–P4.

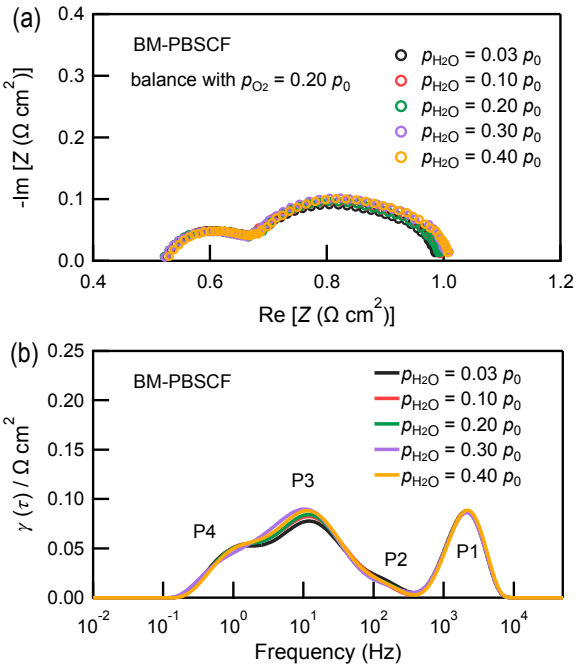

Figure 5-13 (a) EIS and (b) DRT plots of BM-PBSCF cell at 500 °C as a function of steam partial pressures (p_{H2O}).

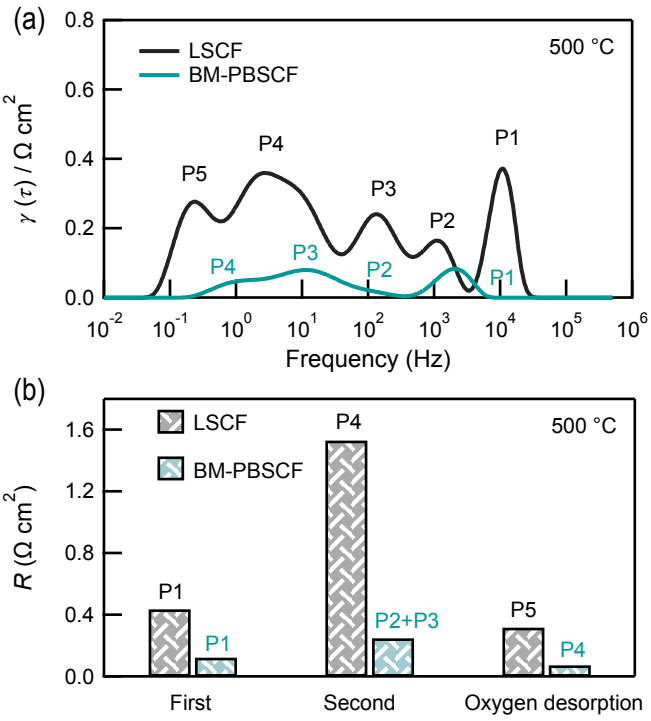

Figure 5-14 (a) DRT plots of LSCF and BM-PBSCF anode-based cells. (b) Corresponding resistances assigned as first and second charger transfer, and oxygen desorption.

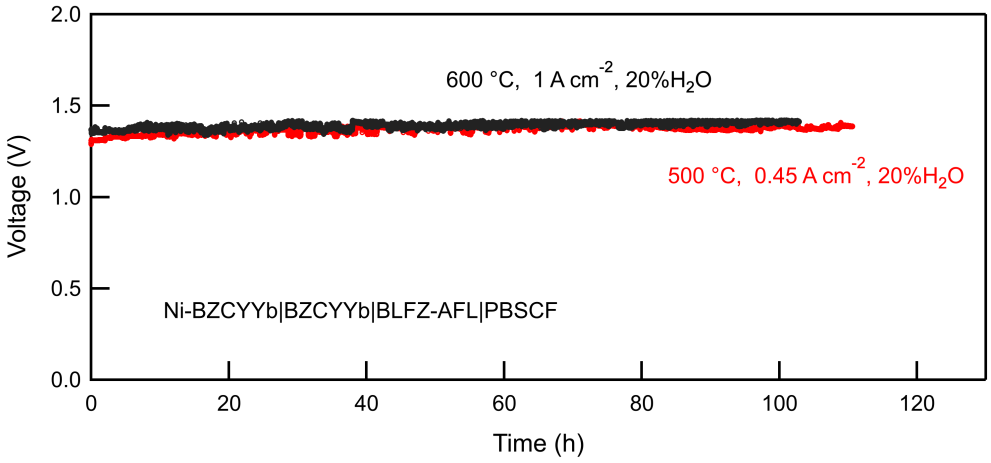

Figure 5-15 Long-term stability of P-SOECs measured at a current density of 1 A cm^{-2} and 0.45 A cm^{-2} for 600 and 500 °C, respectively. The H_2O concentration was fixed at 20%.

5.3.5 Comparison of performance and efficiency in P-SOECs

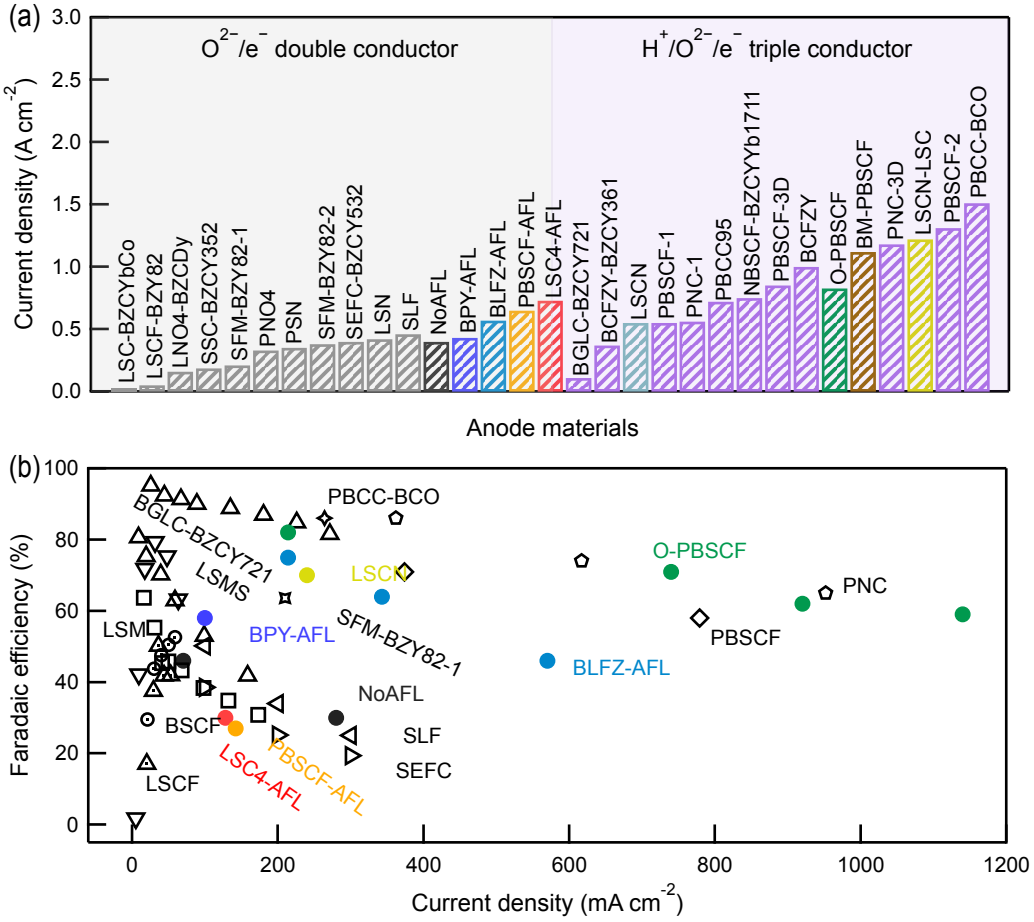

Figure 5-16 Comparison of electrochemical performance and Faradaic efficiencies in advanced P-SOECs with the O^{2-}/e^{-} double conductor and $H^{+}/O^{2-}/e^{-}$ triple conductor anode materials. a) Current density at 600 °C and 1.3 V for steam electrolysis. b) Faradaic efficiency obtained in this thesis and previous P-SOECs as a function of the current density.

Abbreviations of anode: $(LaSr)CoO_{3-\delta}$-$BaZr_{0.40}Ce_{0.48}Yb_{0.1}Co_{0.02}O_{3-\delta}$ (LSC-BZCYbCo),[6] $La_{0.6}Sr_{0.4}Co_{1-x}Fe_xO_{3-\delta}$-$BaZr_{0.8}Y_{0.2}O_{3-\delta}$ (LSCF-BZY82),[7] $La_2NiO_{4+\delta}$-$BaZr_{0.3}Ce_{0.5}Dy_{0.2}O_{3-\delta}$ (LNO4-BZCDy),[8] $Sm_{0.5}Sr_{0.5}CoO_{3-\delta}$-$BaZr_{0.3}Ce_{0.5}Y_{0.2}O_{3-\delta}$ (SSC-BZCY352),[9] $Sr_2Fe_{1.5}Mo_{0.5}O_{6-\delta}$-$BaZr_{0.8}Y_{0.2}O_{3-\delta}$ (SFM-BZY82-1),[10] $Pr_2NiO_{4+\delta}$ (PNO4),[11] $Pr_{1.2}Sr_{0.8}NiO_4$ (PSN),[12] $Sr_2Fe_{1.5}Mo_{0.5}O_{6-\delta}$-$BaZr_{0.8}Y_{0.2}O_{3-\delta}$ (SFM-BZY82-2),[13] $SrEu_2Fe_{1.8}Co_{0.2}O_{7-\delta}$-$BaZr_{0.5}Ce_{0.3}Y_{0.2}O_{3-\delta}$ (SEFC-BZCY532),[14] $Ln_{1.2}Sr_{0.8}NiO_4$ (LSN),[12] $Sr_{2.8}La_{0.2}Fe_2O_{7-\delta}$ (SLF),[15] $La_{0.8}Sr_{0.2}MnO_{3-\delta}$-$BaZr_{0.3}Ce_{0.5}Y_{0.16}Zn_{0.04}O_{3-\delta}$-$Co_3O_4/Fe_2O_3$ (LSM),[16,17] $La_{0.6}Sr_{0.4}Co_{0.2}Fe_{0.8}O_{3-\delta}$-$BaZr_{0.3}Ce_{0.5}Y_{0.16}Zn_{0.04}O_{3-\delta}$ (LSCF),[18] $Ba_{0.5}Sr_{0.5}Co_{0.8}Fe_{0.2}O_{3-\delta}$-$BaZr_{0.3}Ce_{0.5}Y_{0.16}Zn_{0.04}O_{3-\delta}$ (BSCF),[18] $La_{0.8}Sr_{0.2}Mn_{0.95}Sc_{0.05}O_{3-\delta}$ (LSMS),[19] $SrEu_2Fe_{1.8}Co_{0.2}O_{7-\delta}$ (SEFC).[14]

Abbreviations of triple conductors: $BaZr_{0.7}Ce_{0.2}Y_{0.1}O_{2.95}$-$BaZr_{0.7}Ce_{0.2}Y_{0.1}O_{3-\delta}$ (BGLC-BZCY721),[20] $BaCo_{0.4}Fe_{0.4}Zr_{0.1}Y_{0.1}O_{3-\delta}$-$BaZr_{0.3}Ce_{0.6}Y_{0.1}O_{3-\delta}$ (BCFZY-BZCY361),[21] $La_{0.8}Sr_{0.2}Co_{0.7}Ni_{0.3}O_{3-\delta}$ (LSCN in chapter 3), $PrBa_{0.5}Sr_{0.5}Co_{2-x}Fe_xO_{5+\delta}$ (PBSCF-1),[22] $PrNi_{0.5}Co_{0.5}O_{3-\delta}$ (PNC),[23] $(PrBa_{0.8}Ca_{0.2})_{0.95}Co_2O_{6-\delta}$ (PBCC95),[24] $NdBa_{0.5}Sr_{0.5}Co_{1.5}Fe_{0.5}O_{5+\delta}$-$BaZr_{0.1}Ce_{0.7}Y_{0.1}Yb_{0.1}O_{3-\delta}$ (NBSCF-BZCYYb1711),[25] $PrBa_{0.5}Sr_{0.5}Co_{2-x}Fe_xO_{5+\delta}$ (PBSCF-3D),[26] $BaCo_{0.4}Fe_{0.4}Zr_{0.1}Y_{0.1}O_{3-\delta}$ (BCFZY),[27] $PrNi_{0.5}Co_{0.5}O_{3-\delta}$ (PNC-3D),[23] $PrBa_{0.5}Sr_{0.5}Co_{1.5}Fe_{0.5}O_{5+\delta}$ (PBSCF-2),[28] $PrBa_{0.8}Ca_{0.2}Co_2O_{5+\delta}$-$BaCoO_{3-\delta}$ (PBCC-BCO)[29].

Figure 5-16a compares the electrochemical performance at 600 °C and 1.3 V for the cells presented in this thesis and reported previously. In chapter 3, LSC AFL was fabricated between BZCYYb6211 electrolyte and LSCN $H^+/O^{2-}/e^-$ triple conducting anode, achieving a current of 1.22 A cm^{-2} at 600 and 1.3 V, which is higher than most of the previously reported in P-SOECs, such as $BaCo_{0.4}Fe_{0.4}Zr_{0.1}Y_{0.1}O_{3-\delta}$ (BCFZY),[27] $NdBa_{0.5}Sr_{0.5}Co_{1.5}Fe_{0.5}O_{5+\delta}$ (NBSCF),[25] $PrBa_{0.5}Sr_{0.5}Co_{2-x}Fe_xO_{5+\delta}$-3D (PBSCF-3D),[26] and $PrNi_{0.5}Co_{0.5}O_{3-\delta}$ (PNC)[30] although most of them use Ce-rich-side, highly conductive electrolytes BZCYYb4411 or BZCYYb1711. The results of chapter 3 indicate that design of anode functional layer is effective to improve the performance of P-SOECs with Zr-rich electrolyte (BZCYYb6211). However, unfortunately, the Faradaic efficiency (η) is only approximately 70%, as shown in Figure 5-16b.

Therefore, a broad survey of the electrolysis performance was conducted for the cells with various AFLs, as demonstrated in chapter 4. NoAFL cell with LSCF anode have a higher current density (0.395 mA cm^{-2}) than the previously reported P-SOECs using O^{2-}/e^- double-conducting anode materials, such as LSCF,[7] LSC,[6] $La_2NiO_{4+\delta}$ (LNO4)[8] and $Sm_{0.5}Sr_{0.5}CoO_{3-\delta}$ (SSC)[9] as displayed in Figure 5-16a. In addition, the performance of NoAFL cells is comparable to that of novel anode materials. For example, Huan *et al.* reported a current of 0.42 A cm^{-2} with a $SrEu_2Fe_{1.8}Co_{0.2}O_{7-\delta}$ (SEFC)-$BaZr_{0.5}Ce_{0.3}Y_{0.2}O_{3-\delta}$ (BZCY532)[14] composite anode. The composite anode of the redox-stable perovskite $Sr_2Fe_{1.5}Mo_{0.5}O_{6-\delta}$ (SFM) with $BaZr_{0.8}Y_{0.2}O_{3-\delta}$ (BZY82) has a current of 0.38 A cm^{-2},[13] and that of the $La_{1.2}Sr_{0.8}NiO_4$ (LSN)[12] anode has a current of 0.42 mA cm^{-2}. The BLFZ cells achieved 0.57 mA cm^{-2}, which was surprisingly higher than that of P-SOECs with $H^+/O^{2-}/e^-$ triple-conductor anodes for Ba_{1-}

$_x$Gd$_{0.8}$La$_{0.2+x}$Co$_2$O$_{6-\delta}$ (BGLC, 0.11 A cm^{-2}),[20] BCFZY (0.37 A cm^{-2}),[21] La$_{0.8}$Sr$_{0.2}$Co$_{0.7}$Ni$_{0.3}$O$_{3-\delta}$ (LSCN, 0.55 A cm^{-2} in chapter 3), PBSCF (0.55 A cm^{-2})[22] and PNC (0.56 A cm^{-2}).[23] Thus, the modification of electrolyte and anode interfaces by the BLFZ AFL in this work is an effective strategy to improve the performance of electrolyzers. The η of the NoAFL cell is approximately 46% at 0.070 A cm^{-2}, which is similar to those of other O^{2-}/e^- double-conducting anode materials, including La$_{0.8}$Sr$_{0.2}$MnO$_{3-\delta}$ (LSM),[16,17] Ba$_{0.5}$Sr$_{0.5}$Co$_{0.8}$Fe$_{0.2}$O$_{3-\delta}$ (BSCF),[18] SrEu$_2$Fe$_{1.8}$Co$_{0.2}$O$_{7-\delta}$ (SEFC),[14] and Sr$_{2.8}$La$_{0.2}$Fe$_2$O$_{7-\delta}$ (SLF).[15] The BLFZ cell can gain an η of 75% at 0.214 A cm^{-2}, which is higher than the values for the cells with Ba$_{1-x}$Gd$_{0.8}$La$_{0.2+x}$Co$_2$O$_{6-\delta}$ (BGLC) and LSCN (chapter 3) H^+/O^{2-}/e^- single-phase triple-conductor anodes.

Because of the low activity of LSCF, the performance of BLFZ cells is still inferior to those of state-of-the-art P-SOECs, and it is also difficult to obtain high η values. Hence, PBSCF H^+/O^{2-}/e^- triple conducting anode was applied in P-SOECs. The synergy of BLFZ AFL and PBSCF anode further improve the performance and thus the cell with 150 nm-thick BLFZ AFL gains the currents of 0.83 and 1.12 A cm^{-2} for the cells by using O-PBSCF and BM-PBSCF, respectively, (Figure 5-16a). Surprisingly, the η of the cell with O-PBSCF anode increases to 82% and 71% at 500 and 600 °C with currents of 0.22 A cm^{-2} and 0.74 A cm^{-2}, respectively, under the thermal natural potential (1.3V) as shown in Figure 5-16b. These η are much higher than not only the other cells tested in this thesis (chapter 3 and 4) but also the champion data of the cells with PNC (74% at 0.62 A cm^{-2})[23] and PBSCF (71% at 0.37 A cm^{-2}, 58% at 0.78 A cm^{-2}) anodes.[28]

5.4 Conclusion

In summary, this chapter demonstrated that the combination of BLFZ AFL and $H^+/O^{2-}/e^-$ triple conducting PBSCF anode is beneficial to significantly improve the electrolysis performance and conversion efficiency of P-SOECs. When the BLFZ film thickness increased from 0 nm to 150 nm, the steam electrolysis current at 1.3 V increased monotonously from 0.23 to 0.83 A cm^{-2} at 600 °C since the ohmic and reaction resistances decreased from 1.67 to 0.55 Ω cm^2 and from 1.30 to 0.22 Ω cm^2, respectively. The current was slightly lowered by further increase of the thickness to 170 nm. The results confirmed the optimal thickness range for BLFZ thin film should be approximately 150 nm thick. The cell with 150 nm BLFZ AFL had a remarkable Faradaic efficiency equaling to 71% at 0.74 A cm^{-2}, which is the highest value of the cells with Zr-rich side BZCYYb6211 electrolytes. Meanwhile, the use of BLFZ for the anode leaded the deterioration of the performance; 0.32 A cm^{-2} at 600 °C and 1.3V. EIS confirmed that BLFZ anode caused large resistances related to charger transfer and oxygen desorption, indicating that BLFZ is less active than PBSCF for oxygen evolution reaction. In addition, the larger ohmic loss also hindered BM-BLFZ cell to achieve high performance.

5.5 References

1. F.J.A. Loureiro, N. Nasani, G.S. Reddy, N.R. Munirathnam and D.P. Fagg, *J. Power Sources*, 2019, **438**, 226991.
2. S. Jeong, T. Yamaguchi, M. Okamoto, C. Zhu, H. Habazaki, M. Nagayama and Y. Aoki, *ACS Appl. Energy Mater.*, 2020, **3**, 1222–1234.
3. R. J. Kee, H. Zhu, B. W. Hildenbrand, E. Vøllestad, M. D. Sanders and R. P. O'Hayre, *J. Electrochem. Soc.*, 2013, **160**, F290−F300.
4. S. Choi, C. J. Kucharczyk, Y. Liang, X. Zhang, I. Takeuchi, H.-I. Ji and S. M. Haile, *Nat. Energy* 2018, **3**, 202–210.
5. R. Zohourian, R. Merkle, G. Raimondi and J. Maier, *Adv. Funct. Mater.* 2018, **28**. 1801241.
6. M. A. Azimova and S. McIntosh, *Solid State Ionics*, 2011, **203**, 57–61.
7. L. Bi, S. P. Shafi and E. Traversa, *J. Mater. Chem. A*, 2015, **3**, 5815–5819.
8. J. Lyagaeva, N. Danilov, G. Vdovin, J. Bu, D. Medvedev, A. Demin and P. Tsiakaras, *J. Mater. Chem. A*, 2016, **4**, 15390–15399.
9. F. He, D. Song, R. Peng, G. Meng and S. Yang, *J. Power Sources*, 2010, **195**, 3359–3364.
10. L. Lei, Z. Tao, X. Wang, J. P. Lemmon and F. Chen, *J. Mater. Chem. A*, 2017, **5**, 22945–22951.
11. W. Li, B. Guan, L. Ma, H. Tian and X. Liu, *ACS Appl. Mater. Interfaces*, 2019, **11**, 18323–18330.
12. S. Yang, Y. Wen, J. Zhang, Y. Lu, X. Ye and Z. Wen, *Electrochim. Acta*, 2018, **267**, 269–277.
13. L. Lei, J. Zhang, R. Guan, J. Liu, F. Chen and Z. Tao, *Energy Convers. Manag.*, 2020, **218**. 113044.
14. D. Huan, N. Shi, L. Zhang, W. Tan, Y. Xie, W. Wang, C. Xia, R. Peng and Y. Lu, *ACS Appl. Mater. Interfaces*, 2018, **10**, 1761–1770.
15. D. Huan, W. Wang, Y. Xie, N. Shi, Y. Wan, C. Xia, R. Peng and Y. Lu, *J. Mater. Chem. A*, 2018, **6**, 18508–18517.
16. S. Li, R. Yan, G. Wu, K. Xie and J. Cheng, *Int. J. Hydrogen Energy*, 2013, **38**, 14943–14951.
17. H. Li, X. Chen, S. Chen, Y. Wu and K. Xie, *Int. J. Hydrogen Energy*, 2015, **40**, 7920–7931.
18. S. Li and K. Xie, *J. Electrochem. Soc.*, 2013, **160**, F224–F233.
19. L. Gan, L. Ye, M. Liu, S. Tao and K. Xie, *RSC Adv.*, 2016, **6**, 641–647.

20. E. Vøllestad, R. Strandbakke, M. Tarach, D. Catalan-Martinez, M. L. Fontaine, D. Beeaff, D. R. Clark, J. M. Serra and T. Norby, *Nat. Mater.*, 2019, **18**, 752.
21. Y. Meng, J. Gao, H. Huang, M. Zou, J. Duffy, J. Tong and K. S. Brinkman, *J. Power Sources*, 2019, **439**, 227093.
22. W. Wu, D. Ding and T. He, *ECS Trans.*, 2017, **80**, 167–173.
23. H. Ding, W. Wu, C. Jiang, Y. Ding, W. Bian, B. Hu, P. Singh, C. J. Orme, L. Wang, Y. Zhang and D. Ding, *Nat. Commun.*, 2020, **11**, 1907.
24. W. Tang, H. Ding, W. Bian, W. Wu, W. Li, X. Liu, J. Y. Gomez, C. Y. Regalado Vera, M. Zhou and D. Ding, *J. Mater. Chem. A*, 2020, **8**, 14600–14608.
25. J. Kim, A. Jun, O. Gwon, S. Yoo, M. Liu, J. Shin, T.-H. Lim and G. Kim, *Nano Energy*, 2018, **44**, 121–126.
26. W. Wu, H. Ding, Y. Zhang, Y. Ding, P. Katiyar, P. K. Majumdar, T. He and D. Ding, *Adv. Sci.*, 2018, **5**, 1800360.
27. C. Duan, R. Kee, H. Zhu, N. Sullivan, L. Zhu, L. Bian, D. Jennings and R. O'Hayre, *Nat. Energy*, 2019, **4**, 230–240.
28. S. Choi, T. C. Davenport and S. M. Haile, *Energy Environ. Sci.*, 2019, **12**, 206–215.
29. Y. Zhou, E. Liu, Y. Chen, Y. Liu, L. Zhang, W. Zhang, Z. Luo, N. Kane, B. Zhao, L. Soule, Y. Niu, Y. Ding, H. Ding, D. Ding and M. Liu, *ACS Energy Lett.*, 2021, **6**, 1511–1520.

Chapter 6 General conclusion

In this thesis, the protonic solid oxide electrolysis cells (P-SOECs) were investigated, and the following achievements were accomplished. Firstly, P-SOECs were fabricated with thermodynamically stable $BaZr_{0.6}Ce_{0.2}Y_{0.1}Yb_{0.1}O_{3-\delta}$ (BZCYYb6211) electrolyte. The performances of the cells were drastically improved by implementing $La_{0.5}Sr_{0.5}CoO_{3-\delta}$ (LSC) nanofilm as an anode function layer (AFL), and thus the resultant cells exhibited equivalent performance as the cell with Ce-rich side electrolyte $BaZr_{0.1}Ce_{0.7}Y_{0.1}Yb_{0.1}O_{3-\delta}$ (BZCYYb1711). Based on this finding, a broad material survey was conducted with various double- or triple-conducting oxides, and consequently, $Ba_{0.95}La_{0.05}Fe_{0.8}Zn_{0.2}O_{3-\delta}$ (BLFZ) AFL was found to significantly increase the Faradaic efficiency of BZCYYb6211 base P-SOECs. The functionality of BLFZ AFL was clarified by means of electrochemical measurements. Finally, we demonstrated the highest Faradaic efficiency and electrolysis current of P-SOECs with Zr-rich side $Ba(Zr,Ce,M)O_{3-\delta}$ electrolyte. The achievements of this thesis were briefly summarized as follows.

In chapter 1, the urgent demand for industrial production of green hydrogen was explained in terms of utilization of renewable energy for carbon neutrality. Compared to other H_2O electrolysis technologies, the essential merits of P-SOECs were assessed, in concern with the thermodynamic features of water splitting and less-pronounced thermal-corrosion of materials in the relatively low operation temperatures (400–700 °C). On the other hand, major issues of P-SOECs were attributed to the relatively high anodic polarization resistances and low Faradaic efficiency for the cells with thermodynamically sable, Zr-rich side $Ba(Zr,Ce,M)O_{3-\delta}$ electrolyte. The modification of anode/electrolyte interface was identified as a key factor to address these issues, based on the summary of the recent advances and challenges of P-SOECs. Finally, the motivations and objectives of this thesis were clearly stated.

In chapter 2, the experimental methods used in this thesis were introduced. Radio frequency (RF) sputtering and pulse laser deposition (PLD) techniques were applied in this thesis to grow AFL thin films on the electrolyte.

In chapter 3, thin film cells based on high Zr-content BZCYYb6211 and Ce-rich BZCYYb1711 electrolyte were fabricated by solid-state sintering at 1400 °C. The grain sizes of BZCYYb6211 electrolytes (3–4 μm) were smaller than those of Ce-rich BZCYYb1711 electrolytes (20–25 μm), so that the former cell exhibited high ohmic loss than the later probably due to the large grain boundary resistances. Meanwhile, the electrolysis current of BZCYYb6211 cell remarkably increased from 0.55 A cm^{-2} to 1.22 A cm^{-2} at 600 °C with 1.3 V bias by introducing $La_{0.5}Sr_{0.5}CoO_{3-\delta}$ (LSC) AFL of 90 nm thickness at anode/electrolyte interface, which was close to that of BZCYYb1711 cell (1.13 A cm^{-2}), demonstrating the importance of anode/electrolyte interface microstructures. AFL clearly decreased both ohmic resistances and anode reaction resistances at gas-electrolyte-electrode triple phase boundary (TPB), in which the total area-specific resistance (ASR) decreased from 1.50 Ω cm^2 to 0.83 Ω cm^2 at 600 °C under open circuit voltage (OCV). In addition, long-term durability of BZCYYb6211 cell with LSC AFL was carried out at 500 °C for 100 h under applying a constant current of 1 A cm^{-2}. The cell retains a bias at around 1.5 V and achieved Faradaic efficiency of approximately 70%. These results confirmed that steam electrolysis performance of P-SOECs based on Zr rich side $Ba(Ce, Zr, M)O_{3-\delta}$ could be greatly enhanced by AFL and thus the approach was helpful to develop a practical P-SOECs.

In chapter 4, a series of oxides with double- or triple-conductivity were surveyed to explore the optimal materials as AFLs for BZCYYb6211 electrolyte cells with standard air electrode material of $La_{0.6}Sr_{0.4}Co_{0.2}Fe_{0.8}O_{3-\delta}$ (LSCF). According to the OCVs values, these cells could be classified into three categories: (1) relatively low, (2) equivalent and (3) relatively high in comparison to the cell without AFL (NoAFL). Typical material categorized to (1), (2) and (3) are $LaSrCoO_{4+\delta}$ (LSC4), $PrBa_{0.5}Sr_{0.5}Co_{1.5}Fe_{0.5}O_{5+\delta}$ (PBSCF) and $Ba_{0.95}La_{0.05}Fe_{0.8}Zn_{0.2}O_{3-\delta}$ (BLFZ) AFL, respectively. The electrolysis currents of LSC4, PBSCF and BLFZ cells were much larger than that (0.40 A cm^{-2}) of NoAFL cell at 600 °C with 1.3 V bias, which equaled to 0.73, 0.65 and 0.57 A cm^{-2} respectively. Particularly, BLFZ cells possessed the anodic resistance of only 0.46 Ω cm^2 at 600 °C in OCV, which was 80% smaller than

that of NoAFL cell (2.18 Ω cm^2). The distribution of resonant time analysis for impedance spectra revealed that BLFZ AFL significantly extended proton-accessible reaction areas near TPB due to the superior proton conductivity and thus conducted the anode reaction without long range diffusion of O adsorbs. Moreover, BLFZ AFL could significantly increase Faraday efficiency and the corresponding cells exhibited efficiency of 75% at 500 °C with yielding significantly high current density (0.21 A cm^{-2}) at around 1.3 V bias, although LSC4 and PBSCF AFL decreased the efficiency. These results indicated the actual protonic current was changed by AFL, i.e., the AFL-elevating OCVs achieved a high efficiency by lowering the hole leakage. These results proved that BLFZ AFL could retain the relatively high steam partial pressure but lower the oxygen partial pressure at the AFL/electrolyte interface due to the relatively high proton and low oxide ion conductivity and thus suppressed the formation of hole carries at anode/electrolyte interface. Hence, the corresponding cells showed relatively high OCV and high efficiency.

In chapter 5, $H^+/O^{2-}/e^-$ triple conducting PBSCF was applied as anode of P-SOECs with BLFZ AFL. The simultaneous use of PBSCF anode and BLFZ AFL exhibited very low polarization resistances (0.10 Ω cm^2 at 600 °C and OCV), which was only 21% of that (0.46 Ω cm) for cell with LSCF anode. Hence the corresponding cells achieved electrolysis current equaling to 1.10 A cm^{-2} at 600 °C and 1.3 V, with a high efficiency of 71%, which was the highest values of P-SOECs with Zr-rich side BZCYYb6211 electrolyte. Nevertheless, BLFZ was found to poorly active if it was applied to the anode. These proved that AFL played a different role from that of anode in the anode reaction. DRT analysis revealed that BLFZ AFL reduced the resistance related to water adsorption due to the excellent hydration capability whereas PBSCF anode sufficiently decreased the resistance related to charge transfers. The cell with BLFZ AFL showed excellent long-term stability over 100 h with an electrolysis current of 1 A cm^{-2} at 600 °C under high steam condition.

In conclusion, this thesis demonstrated that modification of anode/electrolyte interface with functional oxide interlayer was an alternative way to develop highly efficient P-SOECs with Zr-rich electrolyte. The AFL could tune the hole carrier

concentration in electrolyte and increase proton-accessible reaction areas near the TPB, if the oxides of AFL had significantly high hydration capability and relatively low oxide ion conductivity.

List of publications

1. C. Tang, K. Akimoto, N. Wang, L. Fadillah, S. Kitano, H. Habazaki, Y. Aoki, *J. Mater. Chem. A*, 2021, **9**, 14032–14042.
2. C. Tang, N. Wang, R. Zhu, S. Kitano, H. Habazaki, Y. Aoki, *J. Mater. Chem. A*, 2022, **10**, 15719–15730.

List of other publications

1. N. Wang, C. Tang, L. Du, Z. Q. Liu, W. Li, Z. Song, Y. Aoki, S. Ye, *J. Materiomics*, https://doi.org/10.1016/j.jmat.2022.02.012 (2022).
2. N. Wang, H. Toriumi, Y. Sato, C. Tang, T. Nakamura, K. Amezawa, S. Kitano, H. Habazaki, Y. Aoki, *ACS Appl. Energy Mater.*, 2021, **4**, 554–563.
3. R. Zhu, H. Yang, W. Cui, L. Fadillah, T. Huang, Z. Xiong, C. Tang, D. Kowalski, S. Kitano, C. Zhu, D. R. King, T. Kurokawa, Y. Aoki, H. Habazaki, *J. Mater. Chem. A*, 2022, **10**, 3122–3133.

Acknowledgements

There are so many people I want to give my thanks. First and foremost, I would like to express my sincere gratitude to my supervisor, Dr. Yoshitaka Aoki. It has been such a pleasure having opportunity to learn from him for three years in the Laboratory of Interfacial Electrochemistry. He not only helped me conduct our research carefully and patiently but also taught me how to systematically analyze every work throughout this process. Thanks to his kind guidance and effective discussion, thus, I could finish several works and make this thesis happen.

I would also like to thank Professor Hiroki Habazaki, Professor Kei Murakoshi, Professor Kiyoharu Tadanaga, Professor Chunyu Zhu and Assistant Professor Sho Kitano. Thanks to their support and useful advice that helped me accomplish this thesis. They also gave me friendly care and encouragement in life.

I am forever grateful to the seniors: Dr. Ning Wang taught me many basic experiment skills for the academic research and also gave me help to live in Japan. Dr. SeongWoo Jeong taught me the importance of mathematic model analyses and method to explain our research data. Dr. Yuki Sato provided me a lot of useful information through the long days. Dr. Cheong Kim and Dr. Laras Fadillah's kind help and encouraging conversations. Special thanks are also expressed to my doctoral colleagues: Ruijie Zhu, Hajime Toriumi, Shinichi Nishimura and Katsuya Akimoto for their useful advice and discussion in research. Yoko Iwata, Yukako Yamashita, Midori Mizuki, Takahiro Mori, Ryoya Masuda, Reiko Takusari, Zetao Xiong, Shuya Fujita and other members in the Laboratory Interfacial Electrochemistry for their assistance.

To Wanlu Xiao and Liying Yao, my friends, your presence and company made the life in Japan colorful and gave me a memory that I would never forget.

I would like to acknowledge the financial supports from Chinese Scholarship Council, giving me opportunity to finish the doctor course in Hokkaido University.

I had so much support from my family, especially from my husband Chuanjiang Xia. He helped me solve many problems in life and always gave me laughter. Thanks for being here with me.